Augmenting Biological Fitness Prediction Benchmarks with Landscapes Features from GraphFLA

Mingyu Huang¹, Shasha Zhou², and Ke Li²

¹School of Computer Science and Engineering, University of Electronic Science and Technology of China ²Department of Computer Science, University of Exeter Email: m.huang.gla@outlook.com; {sz484, k.li}@exeter.ac.uk

Abstract

Machine learning models increasingly map biological sequence-fitness landscapes to predict mutational effects. Effective evaluation of these models requires benchmarks curated from empirical data. Despite their impressive scales, existing benchmarks lack topographical information regarding the underlying fitness landscapes, which hampers interpretation and comparison of model performance beyond averaged scores. Here, we introduce GraphFLA, a Python framework that constructs and analyzes fitness landscapes from mutagensis data in diverse modalities (e.g., DNA, RNA, protein, and beyond) with up to millions of mutants. GraphFLA calculates 20 biologically relevant features that characterize 4 fundamental aspects of landscape topography. By applying GraphFLA to over 5,300 landscapes from ProteinGym, RNAGym, and CIS-BP, we demonstrate its utility in interpreting and comparing the performance of dozens of fitness prediction models, highlighting factors influencing model accuracy and respective advantages of different models. In addition, we release 155 combinatorially complete empirical fitness landscapes, encompassing over 2.2 million sequences across various modalities. All the codes and datasets are available at https://github.com/COLA-Laboratory/GraphFLA.

1 Introduction

The fitness landscape is a nearly century-old foundational concept rooted in evolutionary biology [1] with profound implications on the understanding of biological principles in all 3 modalities of the central dogma (DNA, RNA, protein)—from drug resistance [2, 3], enzyme activity [4–8], protein stability and expression [9–11], RNA folding and function [12–16], to transcription factor binding [17, 18]. Efficiently and accurately mapping these fitness landscape surfaces is critical to enable various downstream tasks [19–23], and has been recently advanced by machine learning (ML) models that can capture complex and high-dimensional patterns of the sequence-fitness map [24–30].

A critical step in developing these models is their proper performance evaluation to understand limitations and enable comparisons with existing methods. For this purpose, large-scale benchmarks have been established across different modalities. For example, ProteinGym [31] offers more than 250 tasks curated from deep mutational scanning (DMS) assays for proteins, while RNAGym [32] incorporates over 30 standardized RNA DMS assays. Considering their impressive scales and the famous "no free lunch" theorem [33], it is often unrealistic to expect one single model to dominate on all tasks. For instance, although the VenusREM model [24] yields the highest average score across all 217 DMS substitution tasks in ProteinGym, it leads in only 14 (6.5%) individual tasks. Meanwhile, 44 out of the evaluated 89 models leads in at least one task. This reality prompts critical questions: Q1: "Why did one model perform well on one set of tasks but poorly on another?", Q2: "why did one model outperform baseline on one task, but not on the other?"

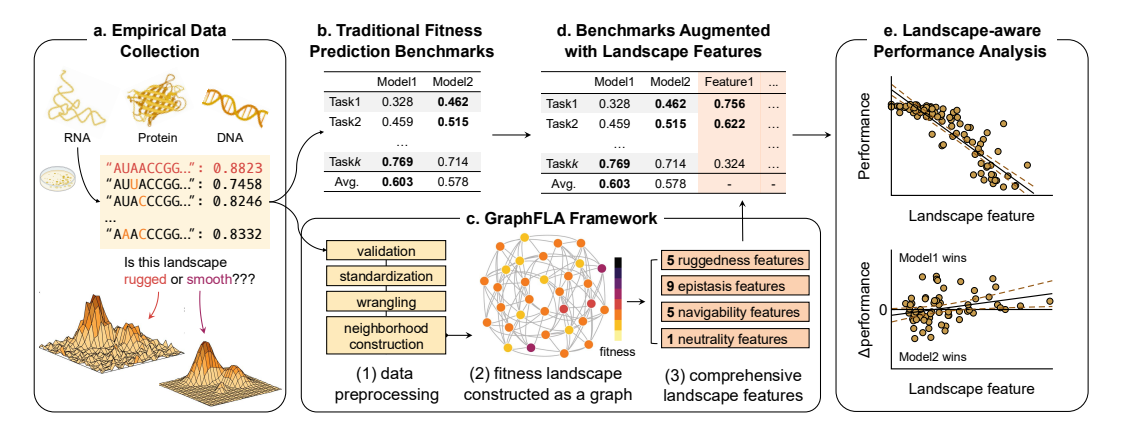


Figure 1: Overview of how GraphFLA contributes to the performance benchmarking of fitness prediction models. Existing biological fitness prediction benchmarks (b) are often curated from empirical fitness landscape datasets without interrogating landscape topography (a). GraphFLA constructs these landscapes and offers a comprehensive suite of features characterizing their topography (c). Such landscape features can then augment existing benchmarks (d) and thus assist performance interpretation (e, upper) and comparison (e, lower).

Answering these questions necessitates informative features that characterize each task. Unfortunately, existing benchmarks typically provide only basic labels (e.g., taxon) or statistics (e.g., sequence length), which are insufficient to fully elucidate the 2 questions above. Consequently, users often rely on average scores for decision-making and comparison, which can lead to biased conclusions.

For decades, evolutionary biologists have developed various features to quantitatively characterize topographical aspects of fitness landscapes, including ruggedness [4, 34, 35, 18], navigability [18, 4, 34, 17, 36], epistasis [37–42], and neutrality [43–45, 22]. These features have been extensively applied to unveil fundamental principles governing evolutionary dynamics [2–18]. As biological sequence models essentially aim to learn these landscape surfaces, we hypothesize that these same features can explain why models perform differently across tasks and address the previous 2 questions.

Yet, despite decades of study, landscape analysis remains a highly specialized biological field. As a result, standard open-source implementations for calculating many landscape features are rarely available. Also, existing research often targets specific landscape aspects, leaving no consensus on a comprehensive feature set. In addition, empirical landscapes span diverse biological modalities and scales, further complicating the development of unified analysis tools. The rapid growth in empirical data also demands highly scalable methods. Consequently, researchers currently lack accessible, broadly applicable tools for characterizing fitness landscape features in common benchmarking tasks.

To address this lack of analysis tooling, we present GraphFLA, a versatile, comprehensive, scalable and end-to-end Python framework for streamlining fitness landscape analysis. GraphFLA constructs fitness landscapes from biological sequence-fitness data in diverse modalities (including, but not limited to DNA, RNA, and protein) and is heavily optimized to scale to datasets with even millions of mutants. It is interoperable with established fitness prediction benchmarks by using an API and data format similar to that used for model training, and is essentially applicable to empirical data in other databases and in the literature. Once a landscape is constructed, GraphFLA offers a rich suite of 20 features compiled from thousands of papers characterizing 4 fundamental aspects of landscape topography: ruggedness, navigability, epistasis, and neutrality, which can serve as biologically meaningful meta-features for each benchmark task to better interpret model performance.

We extensively compared GraphFLA's scalability to existing tools and validated its reliability via a large-scale replication study using 155 combinatorially complete empirical landscapes collected from 61 works (Section 4.1), which are released as part of GraphFLA. We then demonstrated GraphFLA's robustness to data missing, biased sampling, as well as noise in Section 4.2 with synthetic landscapes. To further demonstrate its versatility, we applied GraphFLA to analyze 5,000+ empirical landscapes from ProteinGym, RNAGym, and the CIS-BP database [46]. By employing landscape features from GraphFLA to interpret the performance of dozens of established models on these landscapes, we illustrate that: ▶ Model performance strongly depends on landscape topography; Landscapes that are more rugged, epistatic, neutral, while less navigable, are harder for models to predict accurately (Q1;

Section 4.3); Different models, even with similar overall performance, can excel at different types of landscapes; Performance gaps between them can change with specific landscape characteristics (Q2; Section 4.4). Finally, we showcase the wider utility of GraphFLA by applying it to analyze results of ML-guided directed evolution (MLDE) and phenotype landscapes in Section 4.5.

2 Background and Related Work

Fitness landscapes. In his pioneering work in 1932, Wright first described the concept of a fitness landscape by analogy to a physical landscape, where each spatial location represents a genotype, and the elevation indicates its fitness. Though this landscape metaphor is initially used to describe the genotype-fitness map, its influence quickly extended to other biological modalities and scales, e.g., molecules like RNA [12–16], proteins [47, 10, 11], genes [48, 49], and even communities [50–54].

Landscape topography. Since adaptation can be viewed as navigating fitness landscapes towards their highest peaks, their topography is essential for understanding the course of evolution. The most intuitive and widely studied aspect is **ruggedness** [4, 34, 35, 18], often characterized by the presence of multiple local optima (peaks). A necessary condition for landscape ruggedness is **epistasis** [38–42], which occurs when one or more mutations interact. In contrast, a purely additive landscape, where mutational effects are independent, would be fairly smooth with a single global optimum. Ruggedness along with pervasive epistasis can pose a fundamental challenge to an evolving population's ability to find the highest peak, thus reducing the landscape's **navigability** [18, 4, 34, 17, 36], another important topography aspect. Finally, many studies also interrogate **neutrality** [43–45, 22], which describes the presence of "plateaus" consisting of genotypes sharing the same fitness.

Software packages for landscape analysis. The only biological landscape analysis package known to us, MAGALLEN [55], offers several quantitative metrics but is limited in scope. In contrast, GraphFLA offers a holistic suite of 20 features covering all 4 fundamental aspects above. Also, while MAGALLEN is written in C, it can only rapidly handle landscapes at the scale of 10^5 variants. GraphFLA, however, easily scales to landscapes of 10^7 . Furthermore, MAGALLEN's pure-C implementation also hinders interoperability with modern ML ecosystems, unlike GraphFLA's native Python API.

Empirical fitness landscapes. While early studies of landscape topography often relied on theoretical models (e.g., the NK model [56]), advancements in experimental methodologies have enabled the empirical assessment of increasingly large fitness landscapes [31, 57, 58]. These empirical landscapes are usually constructed by either ▶ randomly sampling a vast number of single- or multi-mutants for a wild-type (WT) sequence (e.g., [10–12]), or ▶ systematically assaying all possible sequences in a predefined space (e.g., [4, 7, 42, 59]). The first approach probes a fairly large area of the sequence space, but the resulting landscape is of narrow depth by containing only immediate neighbors of the WT. In contrast, the second approach generates *combinatorially complete* landscapes that allow exact analysis of topography and enable testing of model predictions on combined effects of mutations.

Fitness prediction benchmarks. Apart from driving biological insights, empirical landscape data also give rise to the wealth of benchmarking tasks for fitness prediction in different modalities [31, 32, 58, 60–64]. While earlier benchmarks like FLIP [58], [62] and [63] comprise only a handful of tasks, recent ones like ProteinGym [31] and RNAGym [32] now offer dozens to hundreds of tasks to enable more robust evaluation. Yet this scale also makes it harder to interpret the results, and users often abandon task-level scores and resort to averages [30, 63]. Though grouping scores based on basic task features (e.g., mutational type, taxon) or analyzing performance distribution can offer additional information [31, 32], they are not sufficient to fully address **Q1** and **Q2** that we previously posed. As a result, these benchmarks have not yet been fully leveraged. GraphFLA contributes augmenting them with fitness landscape features that enable biologically meaningful task-level analysis.

Landscape analysis in other domains. Landscape features have also been widely used to describe problem characteristics in black-box optimization (BBO). For example, the classic 24 BBO benchmarking functions included the COCO platform [65] are classified into 5 groups (from easy to hard) based on features like separability, modality, etc. Another R-package, flacco [66], offers 17 sets of features describing diverse characteristics of the optimization landscape. Similar features also exist for multi-objective optimization problems [67], and they can enable more informed algorithm testing, comparison, selection [68], and configuration [69]. Yet, all these features are designed for general continuous BBO problems. In contrast, GraphFLA is rooted in evolutionary biology for analyzing sequence-fitness landscapes, and goes beyond simple statistics to biologically meaningful ones.

Table 1: Collection of 20 essential landscapes features in GraphFLA

Class	Index	Feature	Ref.	Notation	Range	Higher value indicates
Ruggedness	F1	Fraction of local optima	[4]	$\phi_{ m lo}$	[0, 1]	↑ more peaks
	F2	Roughness-slope ratio	[70]	r/s	$[0,\infty)$	↑ ruggedness
	F3	Autocorrelation	[71]	$ ho_a$	[-1, 1]	↓ ruggedness
	F4	Gamma statistic	[72]	γ	[-1, 1]	↑ ruggedness
	F5	Neighbor-fitness correlation	[73]	NFC	[-1, 1]	↓ ruggedness
	F6	Magnitude epistasis	[36]	$\epsilon_{ m mag}$	[0,1)	↓ evolutionary constraints
	F7	Sign epistasis	[36]	$\epsilon_{ m sign}$	[0, 1]	↑ evolutionary constraints
	F8	Reciprocal sign epistasis	[36]	$\epsilon_{ m reci}$	[0, 1]	↑ evolutionary constraints
	F9	Positive epistasis	[74]	$\epsilon_{ m pos}$	[0, 1]	↑ synergistic effects
Epistasis	F10	Negative epistasis	[74]	$\epsilon_{ m neg}$	[0, 1]	↑ antagonistic effects
	F11	Global idiosyncratic index	[39]	$I_{ m id}$	[0, 1]	↑ specific interactions
	F12	Diminishing return epistasis	[38]	$\epsilon_{ m DR}$	[0, 1]	↑ flat peaks
	F13	Increasing cost epistasis	[75]	$\epsilon_{ m IC}$	[0, 1]	↑ steep descents
	F14	Pairwise epistasis	[42]	$\epsilon_{(2)}$	[0, 1]	↓ higher-order interactions
	F15	Fitness-distance correlation	[76]	FDC	[-1, 1]	↑ navigation
Navigability	F16	Glocal optima accessibility	[18]	$lpha_{ m go}$	[0, 1]	↑ access to global peaks
	F17	Basin-fitness corr. (accessible)	[4]	BFC_{acc}	[-1, 1]	↑ access to fitter peaks
	F18	Basin-fitness corr. (greedy)	[4]	BFC_{greedy}	[-1, 1]	↑ access to fitter peaks
	F19	Evol-enhancing mutation	[73]	$\phi_{ m EE}$	[0, 1]	↑ evolvability
Neutrality	F20	Neutrality	[77]	η	[0, 1]	↑ neutrality

3 GraphFLA: A Framework for Fitness Landscape Analysis

The GraphFLA framework mainly consists of 3 parts (Fig. 1c): (1) data preprocessing, (2) landscape construction, and (3) landscape analysis. We purpose-built GraphFLA to meet 4 desiderata: ► **Applicability** across empirical landscapes from diverse biological modalities and scales. ► **Interoperability** with existing ML-ready data. ► **Scalability** to efficiently handle landscapes containing millions of genetic variants. ► **Extendability** to include new analysis methods via an unified API.

Data input. To ensure compatibility with existing fitness prediction benchmarks, GraphFLA's API accepts the standard inputs used by typical ML models. It takes a list of biological sequences (X) and their corresponding fitness values (f), which can be obtained from either random, site-saturation, or combinatorial mutagenesis, or other analogous design. GraphFLA supports sequences of length n where each locus $i \in \{1, \ldots, n\}$ can take distinct values from a predefined set \mathcal{A}_i ($|\mathcal{A}_i| \geq 2$; for DNA, $\mathcal{A}_i = \{A, C, G, T\}$). This flexible representation enables GraphFLA to handle various biological modalities, such as DNA, RNA, proteins, genes, and even complex microbial communities. We also include built-in classes optimized for common sequence types (e.g., DNA, RNA, proteins, and binary data) to enhance performance. Additionally, GraphFLA's preprocessing pipeline automatically detects the composition of the sequence space, standardizes the input data, and identifies duplicates or missing values. This careful preprocessing ensures reliable results in subsequent analyses.

Neighborhood identification. Next, GraphFLA determines a neighborhood structure, which specifies which variants are genetically adjacent to each other in the sequence space. To this end, traditional methods calculate genetic distances between all possible pairs of variants to find one-mutant neighbors [4, 55]. However, this pairwise calculation quickly becomes impractical because it requires quadratic time and memory resources. To overcome this scalability issue, GraphFLA employs a more efficient approach: Instead of comparing every pair, it directly generates all potential single-mutation neighbors for each variant. This new strategy achieves nearly linear complexity and significantly outperforms existing implementations in both runtime and memory efficiency (Section 4.1).

Landscape as a variant network. Once the neighborhood is identified, GraphFLA constructs the fitness landscape as a directed graph (Fig. 1c), wherein each node represents a variant and is associated with its fitness; any two variants that are neighbors to each other are connected by an directed edge, which represents a single mutational step towards the fitter variant. This graph representation, backend by the igraph package in C, allows many landscape analysis to be implemented via efficient graph mining algorithms for significant speed up. For example, locating local optima can be done by finding all *sinks* in this graph, while classifying different types of epistasis is equivalent to finding specific types of 4-node motifs (Appendix C).

Table 2: Summary of combinatorially complete datasets in GraphFLA

Modality	Space	No. of Datasets	No. of Mutants
DNA	Genomic sequence	55	724k
Protein	Transcript sequence	63	1.1M
RNA	Amino acid sequence	37	348k
Total		155	2.2M

Landscape analysis. For each constructed landscape, GraphFLA offers a comprehensive suite of 20 features characterizing their 4 fundamental topographical aspects: ruggedness, navigability, epistasis, and neutrality (Table 1). In selection of these features, we conducted an large language model-assisted, data-driven survey of 1,673 papers on landscape analysis and evolutionary biology (Appendix B), which aims to identify all prevalemt quantitative indicators of landscape topography in literature. From more than 100 initial candidates, we compiled this final collection of 20 essential features based on their (1) frequency of appearance in literature, (2) biological significance, (3) coverage across different aspects, (4) computational feasibility, and (5) compatibility with data modalities, sizes, and structures (see details in Appendix B). A full introduction to them is available in Appendix C

Empirical and theoretical landscapes. Beyond the main modules depicted in Fig. 1c, GraphFLA provides a data module featuring 155 empirical fitness landscapes that are combinatorially complete, covering more than 2.2M total variants (Table 2; Table A3). These landscapes, gathered via another extensive literature survey (Appendix B), span multiple modalities (DNA, RNA, protein) and taxa with diverse fitness metrics. The comprehensive combinatorial nature of this collection distinguishes it from current benchmarks, which mainly consist of randomly generated mutagenesis libraries. This structure enables systematic evaluation of model predictions on combined mutations of varying orders and aids in interpreting results through landscape topography. Although some landscapes in this suite overlap with benchmarks like ProteinGym and RNAGym, GraphFLA is more exhaustive regarding combinatorial libraries. For instance, it contains several 4-site saturation protein landscapes ($20^4 = 160,000$ total variants) not found in ProteinGym [78, 79, 47]. In addition to these empirical landscapes, GraphFLA provides 5 theoretical models for generating synthetic landscapes with tunable characteristics (e.g., size, ruggedness; Appendix D)

4 Results

4.1 GraphFLA Enables Efficient and Accurate Landscape Analysis Across Modalities

Runtime and memory scalability. To evaluate the performance of GraphFLA, we generated synthetic fitness landscapes of varying sizes using the *NK* model by Kauffman. We then compared the scalability of landscape construction with that of the MAGELLAN package and the community implementation used in [4] The benchmarks were conducted using a single core of an Intel Xeon Platinum 8260 CPU with 256GB RAM. Our findings in Fig. 2a show that GraphFLA is significantly faster in landscape construction compared to existing implementations. For example, the two baselines took more than 5h and 3h respectively to construct the landscape at the scale of 1 million mutants, whereas GraphFLA used only 20s. Regarding memory efficiency, GraphFLA stood out by requiring only 2GB memory to process 1 million mutants. In contrast, the community implementation encountered out-of-memory errors when handling over 100,000 mutants. In sum, GraphFLA scales almost linearly with landscape size, allowing it to process even the largest empirical fitness landscapes with millions of mutants.

Application to diverse real-world data. To demonstrate the versatility of GraphFLA in processing real-world data for fitness predictions, we applied it to 4 large-scale benchmarks and databases to construct 5,300+ landscapes in different modalities and sizes for different species. We then calculated the 20 landscape features introduced in Table 1 for each of them (Table A3, Table A4, Table A5).

• **ProteinGym.** We used its 217 DMS substitution tasks. Since the data is highly curated, GraphFLA can directly construct landscape for each task using the "sequences" and "DMS_score" columns, with the only preprocessing being removing the common genetic backgrounds. This results in 217 landscapes (2.2M total mutants) describing protein activity, binding, expression, stability, etc. We note that 168 of these landscapes only contain single mutants, and were excluded from subsequent analysis as there is little information beyond the local neighborhood of the WT.

Table 3: Four essential landscape	metrics across reference,	incomplete, noisy	, and biasedly sampled
NK landscapes.			

Setting	Reciprocal sign epistasis	Global optima accessibility	Autocorrelation	FDC
reference (complete)	0.1885	0.6729	0.1151	-0.0313
incomplete (10%)	0.1883	0.6103	0.0927	-0.0420
incomplete (20%)	0.1884	0.5276	0.0771	-0.0337
incomplete (50%)	0.1774	0.3223	0.0553	-0.0313
noisy (0.01σ)	0.1889	0.6492	0.0965	-0.0314
noisy (0.05σ)	0.1896	0.6542	0.0927	-0.0317
noisy (0.1σ)	0.1921	0.6362	0.0966	-0.0319
noisy (0.2σ)	0.1984	0.6339	0.0867	-0.0414
biased (random mutagenesis)	0.1823	0.7246	0.1208	-0.0837

- **RNAGym.** We used the 33 fitness prediction tasks from it, following the same procedure above. This leads to 31 landscapes (358k total mutants) for mRNAs, tRNAs, aptamers, and ribozymes.
- Combinatorially complete landscapes. We constructed 155 combinatorially complete using the datasets introduced in Table 2, which contain a mixture of DNA, RNA, and protein landscapes.
- **CIS-BP database.** It harbors protein-binding microarray (PBM) data for 5,016 TFs of 329 eukaryotic species and 162 DNA-binding domain structural classes from 78 studies [46]. For each TF, the fitness is its binding affinity to all 32,896 possible 8-nucleotide, double-stranded DNA sequences. GraphFLA constructed these 5,016 TF binding landscapes with 174M total mutants.

Validation with existing literature. We proceeded to assess the precision of GraphFLA's landscape analysis by performing a large-scale replication study across the 61 papers from which our 155 combinatorially complete datasets originate. For each publication, we identified its reported qualitative (e.g., "highly navigable" [4]) and quantitative (e.g., "514 peaks" [4]) landscape characteristics. We then utilized the relevant metrics within GraphFLA to re-analyze these landscapes, and compared our outputs against the original findings. GraphFLA successfully replicated the qualitative conclusions from all 61 studies (full results in Table A3). Notably, for features with unique definitions such as ϕ_{lo} and ϵ_{reci} , GraphFLA precisely reproduced the published values if data processing details were sufficiently described. For features with more generalized definitions for which implementations can vary (e.g., ϵ_{DR}), GraphFLA's analysis consistently supported the conclusions drawn in the original studies. These results demonstrated that GraphFLA is a reliable framework for landscape analysis.

4.2 GraphFLA is Robust to Incomplete, Noisy, and Biasedly Sampled Data

A crucial validation for any analysis framework is quantifying its robustness to imperfect data. Real-world empirical landscapes often suffer from (a) missing variants, (b) experimental noise in fitness measurement, or (c) biased sampling in generating the mutant library. In order to validate GraphFLA's rosbutness to these, we conducted experiments on a *complete NK* landscape with moderate size and ruggedness (n = 15, k = 7), which can serve as a reference that represents the most ideal data.

Robustness to incomplete data. We created *incomplete* landscapes by randomly removing a fraction $\alpha = \{10\%, 20\%, 50\%\}$ of total variants. We then calculated four representative landscape features for these and the reference landscape in Table 3. The results shows that most key features are highly robust to data incompleteness. The one exception is global optima accessibility, which, as expected, decreases as more data is removed, since this will destroy paths leading to the global optima regardless of their evolutionary accessibility. Yet, this effect is predictable and can be partially corrected by scaling the measured accessibility by the fraction of remaining data $(1-\alpha)$.

Robustness to noisy data. To simulate experimental noise, we perturbed the fitness score of each variant by adding random noise drawn from a Gaussian distribution $\mathcal{N}(0,(\beta\sigma)^2)$, where σ is the standard deviation of the original fitness values and the noise level β was set to $\{0.01,0.05,0.1,02\}$. The results in Table 3 demonstrate that all four landscape features remain remarkably stable. Even with noise equivalent to 0.2σ , the calculated values are consistent with the reference. This highlights that GraphFLA's feature calculations are resilient to typical levels of experimental noise.

Robustness to biased sampling. We then simulated a more realistic scenario of random mutagenesis, which often creates a library that is densely sampled near a wild-type sequence but sparse elsewhere. We created a sparse, *biased* library of 1,804 variants (from 32,768 total) by applying a 10% per-site

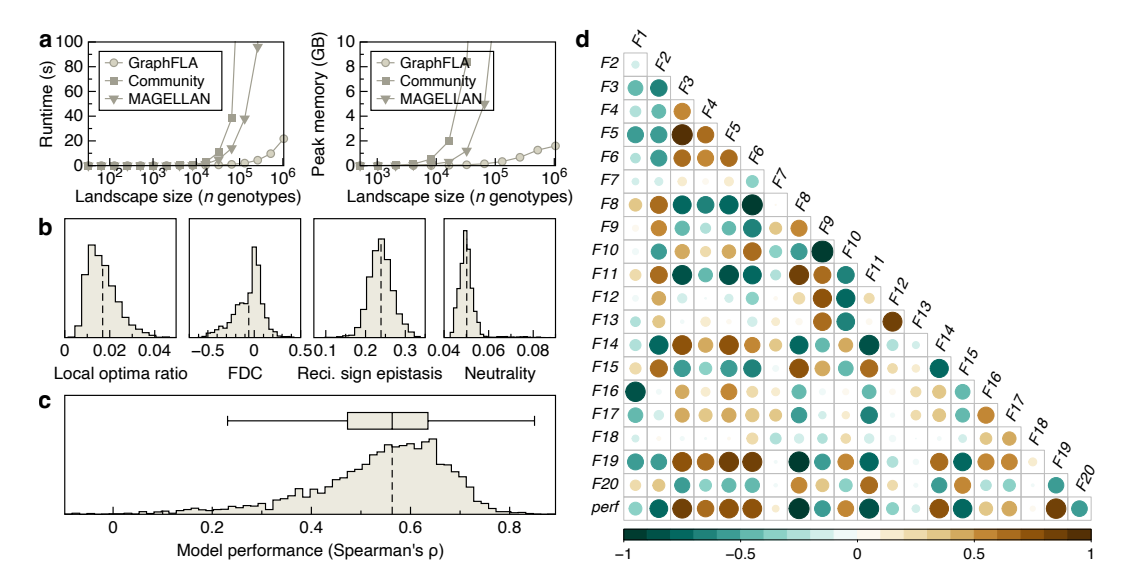


Figure 2: GraphFLA scales efficiently and captures influential landscape features for model performance. (a) Runtime (left) and peak memory usage (right) during fitness landscape construction for GraphFLA, MAGELLAN, and a community implementation [4], as a function of landscape size. Landscapes were generated using the NK model [80] by varying the number of loci N from 5 to $20~(\rightarrow$ landscape sizes from 2^5 to 2^{20}). Results shown are averages across 10 replicates. (b) Distribution of 3 representative landscape features across 155 combinatorially complete landscapes collected in GraphFLA. (c) Distribution of model performance, measured by Spearman's ρ , for Evo2 predictions across the same 155 landscapes. (d) Correlation matrix showing Spearman's ρ between 20 landscape features derived from GraphFLA and Evo2 performance across all 155 combinatorial landscapes.

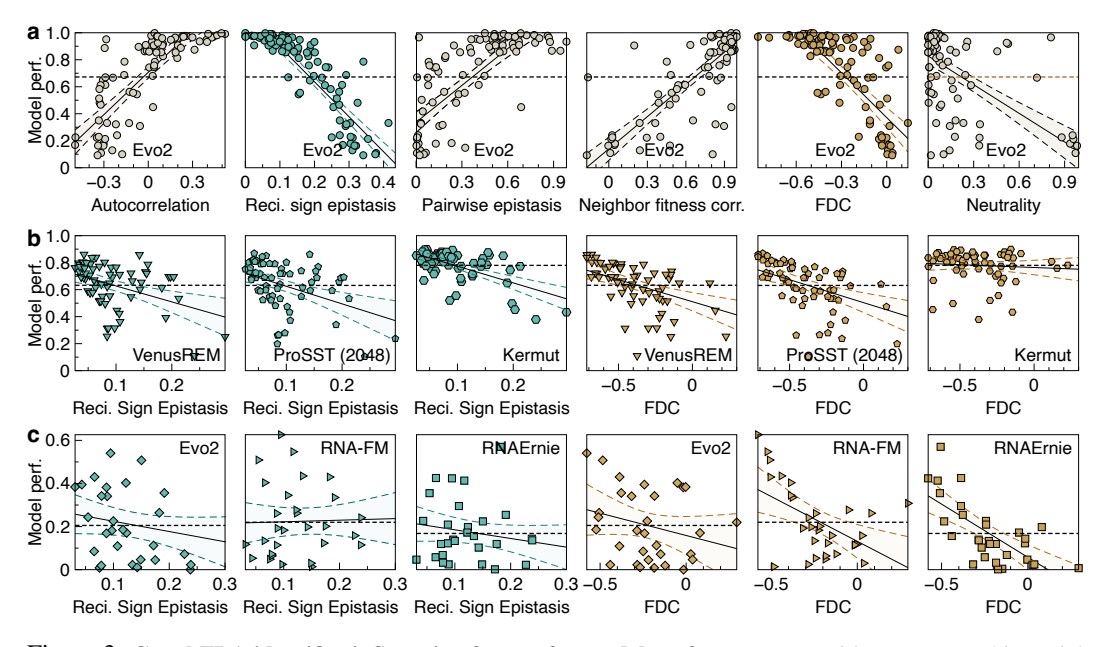


Figure 3: GraphFLA identifies influencing factors for model performance. For (a) our 155 combinatorial landscapes, (b) ProteinGym, and (c) RNAGym, we plot the distribution of model (name specified in each plot) performance (y-axis; measured as Spearman's ρ) against landscape features (x-axis). Straight lines show a fit of the linear regression model, and shaded regions depict the 95% confidence intervals. Dashed horizontal lines indicate the average performance across all landscapes.

mutation rate to the global optimum. As shown in Table 3, the key landscape features remain highly consistent with the reference landscape, even when calculated on this much smaller, non-uniform subset. This implies that GraphFLA can still provide reliable approximation of the overall landscape topography even with only biasedly and sparsly sampled data.

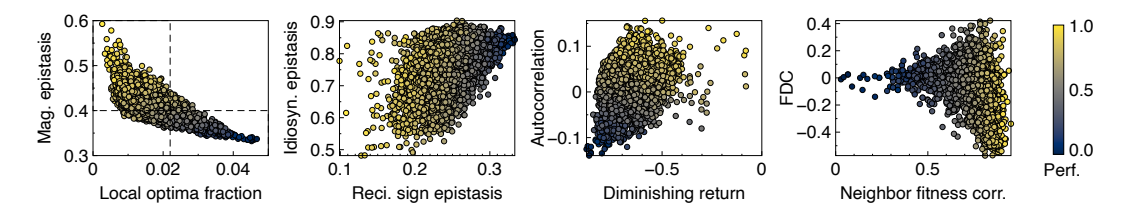


Figure 4: Visualizing the distribution of model performance in landscape feature space. We map each of the 5, 016 landscapes constructed from the CIS-BP data in the space composed of landscape features and color-coded with the performance (Spearman's ρ) of Evo2-7b to visualize its distribution in the feature space.

4.3 GraphFLA Identifies Key Influence Factors and Bottlenecks in Fitness Prediction

The 5,300 empirical landscapes we constructed in Section 4.1 exhibit significant variation in their topography. For instance, across the 155 combinatorially complete landscapes, the percentage of local optima ranges from around 0% to 5% (Fig. 2b). While the former value corresponds to a fairly smooth, unimodal landscape, the latter is on par with that of the most rugged NK landscapes [81]. Similar observations can be made for other landscape features (Fig. 2b; Fig. A1) and for ProteinGym (Fig. A2) as well as RNAGym (Fig. A3). From a performance benchmarking perspective, this is a good sign since it implies that the included tasks are diverse enough to "stress-test" models [82].

To illustrate how landscape features can shed light on fitness prediction performance, and thus our Q1 in Section 1: "Why did one model perform well on one set of tasks but poorly on another?", we used Evo2-7b [27], the successor of Evo [63], as an example. It is trained on 9.3 trillion DNA base pairs and applicable to diverse modalities including DNA, RNA, and protein. We applied Evo2 to each of our 155 combinatorial landscapes, and assessed its performance in fitness prediction using Spearman's ρ as in prior works [83, 60, 84, 61, 85]. We found that Evo2's performance varies significantly across landscapes (Fig. 2c), and is highly dependent on landscape features (Fig. 2d). Specifically, half of the landscape features yielded Spearman's $|\rho|$ higher than 0.6 with Evo2's performance, and 6 revealed moderate correlation (0.3 $< |\rho| < 0.6$). Similar results can be obtained by considering partial correlations controlling for landscape size. By taking a closer look at how Evo2's performance varies with landscape features Fig. 3a, we found that it struggles on landscapes that are:

- More rugged and more epistatic. In such landscapes, fitness values often fluctuate dramatically even in local regions within a small genetic distance (low ρ_a and NFC). Extrapolation of such landscapes, even across only a single mutation, may fail due to the existence of local epistatic hotspots (often local optima) resulting from high-order (indicated by low $\epsilon_{(2)}$), non-magnitude epistasis (indicated by high $\epsilon_{\rm reci}$) between sites that are unique to the current landscape.
- Less navigable. Benign landscapes that are easy to navigate and predict have strongly negative fitness distance correlation (FDC)—variants closer to the global peak in genetic distance tend to have higher fitness. In contrast, when FDC becomes closer to zero or positive, this information diminishes and even becomes "deceptive" (e.g., fitness declines as approaching global peak).
- **Highly neutral.** These landscapes feature abundant "plateau" regions where mutations have zero fitness effects (i.e., neutral), which can hardly be predicted by models trained on non-neutral data.

While such findings were drawn from landscapes with heterogeneous modalities and a general model, similar patterns can be observed in more specific settings. For example, current leading zero-shot models on ProteinGym's 217 DMS substitution tasks, VenusREM [24], ProSST (k=2,048) [25], and the leading supervised model, Kermut [26], tend to excel at fitness prediction for benign protein landscapes with FDC < -0.5 and $\epsilon_{\rm reci} < 0.1$, yet still struggles for more complex ones (Fig. 3b; more models and features in Fig. A8, Fig. A9). Established models for RNA fitness prediction like RNA-FM [28] and RNAErine [29] exhibited the same behavior (Fig. 3c; more in Fig. A10, Fig. A11).

To see this at a larger scale, we evaluated the performance of Evo2-7b on the 5,016 CIS-BP TF binding landscapes described in Section 4.1. We plotted each landscape instance in the feature space shown in Fig. 4, and mapped Evo2's performance to this space. From the results, we can observe a clear trend that landscapes located in certain regions of the feature space are in general harder to predict. For example, in the first panel, Quadrant II is occupied by landscapes featuring both a large number of local optima (ϕ_{lo}) and abundant non-magnitude epistasis (ϵ_{reci}), and Evo2 can hardly identify the true fitness rank in them despite extensive pre-training. On the other hand, landscapes

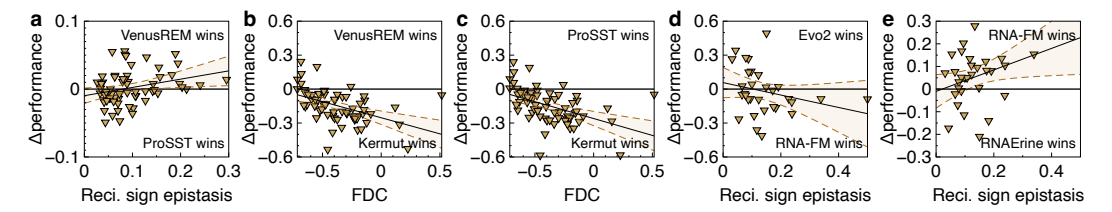


Figure 5: GraphFLA facilitates landscape-aware model comparison. Difference in performance (y-axis) between 5 pairs of baselines in ProteinGym $(\mathbf{a}, \mathbf{b}, \mathbf{c})$ and RNAGym (\mathbf{d}, \mathbf{e}) is plotted against landscape features on the x-axis. Line regression fit lines and 95% confidence intervals are depicted.

belonging to Quadrant IV are much more benign with low ϕ_{lo} and ϵ_{reci} . For such landscapes, Evo2 typically achieved Spearman's $\rho>0.5$. As for Quadrant I and III, landscapes in these regions contain a combination of complex and benign landscapes, which gave rise to mixed performance outcomes. The same trend can be observed for other combinations of features in other panels of Fig. 4.

4.4 GraphFLA Facilitates Landscape-aware Model Comparison

Another important question we asked is **Q2:** "why does one model outperform the baseline on one task, but not on the other?" For example, though VenusREM and ProSST (k=2,048) have similar (Spearman's ρ : 0.518 vs 0.507) zero-shot performance on ProteinGym, they lead on 53% and 47% of tasks, respectively. Without further information on each task it is hard to strictly distinguish them.

Here we demonstrate that GraphFLA's landscape features can shed light on their respective advantages. Fig. 5a plots the Δ performance between VenusREM and ProSST on each task against the $\epsilon_{\rm reci}$ of the corresponding landscape. We found that on benign landscapes with little reciprocal sign epistasis ($\epsilon_{\rm reci} < 0.1$), ProSST tends to outperform VenusREM (Wilcoxon signed-rank test, w=123, p=0.003). Yet this advantage diminishes as $\epsilon_{\rm reci}$ increases, as indicated by a positive slope of the linear regression line in Fig. 5a. Eventually, for landscapes with $\epsilon_{\rm reci} > 0.15$, VenusREM consistently outperforms ProSST, which implies it is better at capturing complex epistatic interactions.

More intriguingly, both these zero-shot models can only outperform Kermut, the leading supervised baseline, on highly navigable landscapes (FDC ≈ -0.7 ; Fig. 5b, c). As landscapes become less navigable (i.e., FDC increases), the performance gap between VenusREM (or ProSST) and Kermut increases drastically (Fig. 5b, c). Notably, for the ODP2 landscape from [86], which has an FDC = 0.23, Kermut outperforms VenusREM by a Spearman's ρ of 0.53. The same pattern can be observed if we replace Kermut with other supervised baselines like ProteinNPT [87] (Fig. A12). These highlight that supervised training is still necessary to better extrapolate on complex landscapes.

As for RNAGym, though Evo2 and RNA-FM achieved comparable prediction performance across all analyzed landscapes (Fig. 3c), the former falls short on landscapes with high incidence of reciprocal sign epistasis ($\epsilon_{\rm reci} > 0.2$; Fig. 5d). Also, the performance gap between RNA-FM and RNAErine increases as the landscape becomes more epistatic ($\epsilon_{\rm reci}$ increases; Fig. 5e). These results shed new light on the respective of different models beyond simple averaged scores.

4.5 GraphFLA is Applicable to a Broader Range of Tasks and Data

Application to directed evolution. Beyond fitness prediction, GraphFLA can also be employed to shed light on other tasks related to fitness landscapes. For example, as directed evolution (DE) [88–91], a central technique in protein engineering, is essentially an adaptive walk on the protein fitness landscape to find high fitness variants, landscape topography can have fundamental impact on its success. For instance, DE on rugged landscapes is notoriously difficult [92]. However, a comprehensive understanding of the impact of ruggedness, and other landscape features, on DE, has been missing due to the lack of (1) holistic landscape analysis frameworks like GraphFLA, and (2) large collection of combinatorially complete empirical landscapes like in Table 2.

To demonstrate how GraphFLA can provide insights into DE, we used 20 protein landscapes from our combinatorial library that are 3- or 4-site-saturated (i.e., total variants being 20^3 or 20^4). For each of them, we evaluated the performance of 5 DE classic approaches: (1) the simplest DE, implemented as a greedy adaptive walk; (2) ML-guided DE (MLDE) [92, 93]; (3) MLDE warm-started with a zero

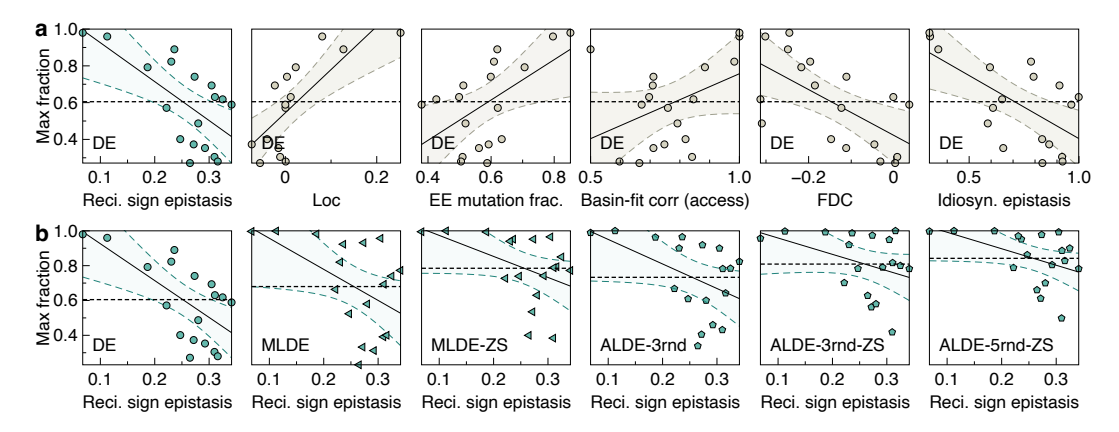


Figure 6: GraphFLA can be employed to interpret directed evolution (DE) outcomes. (a) The maximum fitness achieved (in percentile) by DE on each selected landscape against landscape features. (b) We fixed the x-axis to be reciprocal sign epistasis and replaced DE with 5 other ML-guided methods. Dashed horizontal lines indicate the average performance across all landscapes.

short model [90]; (4) Active learning-guided directed evolution (ALDE) [94, 95]; (5) ALDE with zero-shot warm start. Detailed implementations are available in Appendix F. For each approach, we measured performance using the fitness percentile (where 1 indicates finding the global optimum) of the best variant it found, and aggregated across 100 randomly initialized runs. For the two ALDE methods, we additionally set the number of iterations to 3 or 5 rounds.

From Fig. 6a, we can see that while the basic DE method can easily find variants with fitness close to the global optimum on benign landscapes, it struggles on ones that are more rugged and epistatic, and less navigable. The 5 ML- or active learning-guided approaches are also susceptible to the incidence of epistasis, but more advanced approaches—such as MLDE with a zero-shot warm start and the ALDE variants—demonstrated greater robustness and are less adversely affected (Fig. 6b).

Application to other data. Beyond molecular sequences such as DNA, RNA, and proteins, GraphFLA can be applied to fitness landscapes at various other biological scales. For instance, it can be utilized to analyze evolutionary landscapes of gene regulatory networks [48, 49] or metabolic landscapes [96] at the cellular level. It can also analyze how alterations in community composition impact collective functions [50–54]. As a demo, we analyzed 6 microbial community-function landscapes in Table A2. In addition to traditional fitness landscapes, GraphFLA can be adapted to study a broad array of phenotype landscapes, a.k.a, genotype-phenotype (GP) maps, for RNA secondary structure [97], protein tertiary structure [98, 99], and protein complexes [100], etc. We provide demonstrations for these using computational models and 3 phenotype landscape features in Appendix E.

5 Conclusion

GraphFLA addresses the critical lack of meaningful features for interpreting performance benchmarking results in sequence fitness prediction. Using its comprehensive suite of 20 features describing the underlying landscape topography, we are now able to answer questions like "why model performance varies across tasks?", "when and why will a model outperform the other?". In this way, GraphFLA augments current benchmarks like ProteinGym and RNAGym to fully take advantage of their impressive scales, and assists in obtaining granular understanding of the capabilities and limitations of existing genomic models that were previously impossible. In addition, since GraphFLA itself is designed for arbitrary combinatorial landscapes, we expect it will be a useful resource for advancing our understanding on a broader range of tasks and data that is related to combinatorial optimization.

Acknowledgements. We sincerely thank all the reviewers for their encouraging and constructive feedback. This work was supported by the UKRI Future Leaders Fellowship under Grant MR/S017062/1 and MR/X011135/1; in part by NSFC under Grant 62376056 and 62076056; in part by the Royal Society Faraday Discovery Fellowship (FDF/S2/251014), BBSRC Transformative Research Technologies (UKRI1875), Royal Society International Exchanges Award (IES/R3/243136), Kan Tong Po Fellowship (KTP/R1/231017); and the Amazon Research Award and Alan Turing Fellowship.

References

- [1] S. Wright. The roles of mutation, inbreeding, crossbreeding and selection in evolution. *Proc. XI Int. Congr. Genet.*, 8:209–222, 1932.
- [2] N. A. Rizvi, M. D. Hellmann, A. Snyder, P. Kvistborg, V. Makarov, J. J. Havel, W. Lee, J. Yuan, P. Wong, T. S. Ho, M. L. Miller, N. Rekhtman, A. L. Moreira, F. Ibrahim, C. Bruggeman, B. Gasmi, R. Zappasodi, Y. Maeda, C. Sander, E. B. Garon, T. Merghoub, J. D. Wolchok, T. N. Schumacher, and T. A. Chan. Cancer immunology. mutational landscape determines sensitivity to PD-1 blockade in non-small cell lung cancer. *Science*, 348(6230):124–128, 2015.
- [3] Chen JZ, Fowler DM, and Tokuriki N. Environmental selection and epistasis in an empirical phenotype-environment-fitness landscape. *Nat. Ecol. Evol.*, 6(4):427–438, 2022.
- [4] Andrei Papkou, Aviv Regev, and Joanna Masel. A rugged yet easily navigable fitness landscape. *Science*, 382:eadh3860, 2023.
- [5] Daniel M. Weinreich, Nigel Delaney, Mark A. DePristo, and Daniel L. Hartl. Darwinian evolution can follow only very few mutational paths to fitter proteins. *Science*, 312(5770): 111–114, 2006.
- [6] M. Lunzer, S. P. Miller, R. Felsheim, and A. M. Dean. The biochemical architecture of an ancient adaptive landscape. *Science*, 310(5747):499–501, 2005.
- [7] K. E. Johnston, P. J. Almhjell, E. J. Watkins-Dulaney, G. Liu, N. J. Porter, J. Yang, and F. H. Arnold. A combinatorially complete epistatic fitness landscape in an enzyme active site. *Proc. Natl. Acad. Sci. U. S. A.*, 121(32):e2400439121, 2024.
- [8] A. Judge, B. Sankaran, L. Hu, M. Palaniappan, A. Birgy, B. V. V. Prasad, and T. Palzkill. Network of epistatic interactions in an enzyme active site revealed by large-scale deep mutational scanning. *Proc. Natl. Acad. Sci. U. S. A.*, 121(12):e2313513121, 2024.
- [9] J. Zheng, N. Guo, and A. Wagner. Selection enhances protein evolvability by increasing mutational robustness and foldability. *Science*, 370(6521):eabb5962, 2020.
- [10] P. J. Ogden, E. D. Kelsic, S. Sinai, and G. M. Church. Comprehensive AAV capsid fitness landscape reveals a viral gene and enables machine-guided design. *Science*, 366(6469): 1139–1143, 2019.
- [11] K. S. Sarkisyan et al. Local fitness landscape of the green fluorescent protein. *Nature*, 533: 397–401, 2016.
- [12] C. Li, W. Qian, M. Maclean, and J. Zhang. The fitness landscape of a tRNA gene. *Science*, 352:837–840, 2016.
- [13] Sam F. Greenbury, Ard A. Louis, and Sebastian E. Ahnert. The structure of genotype-phenotype maps makes fitness landscapes navigable. *Nat. Ecol. Evol.*, 6(11):1742–1752, 2022.
- [14] O. Puchta, B. Cseke, H. Czaja, D. Tollervey, G. Sanguinetti, and G. Kudla. Network of epistatic interactions within a yeast snorna. *Science*, 352(6287):840–844, 2016.
- [15] J. I. Jiménez, R. Xulvi-Brunet, G. W. Campbell, R. Turk-MacLeod, and I. A. Chen. Comprehensive experimental fitness landscape and evolutionary network for small RNA. *Proc. Natl. Acad. Sci. U. S. A.*, 110(37):14984–14989, 2013.
- [16] Joel N. Pitt and Adrian R. Ferré-D'Amaré. Rapid construction of empirical RNA fitness landscapes. *Science*, 330(6002):376–379, 2010.
- [17] Joshua L. Payne and Andreas Wagner. The robustness and evolvability of transcription factor binding sites. *Science*, 343(6173):875–877, 2014.
- [18] Juan Aguilar-Rodríguez, Joshua L. Payne, and Andreas Wagner. A thousand empirical adaptive landscapes and their navigability. *Nat. Ecol. Evol.*, 1(2):45, 2017.
- [19] P. Notin, N. Rollins, Y. Gal, C. Sander, and D. Marks. Machine learning for functional protein design. *Nat. Biotechnol.*, 42(2):216–228, 2024.
- [20] T. Hayes, R. Rao, H. Akin, N. J. Sofroniew, D. Oktay, Z. Lin, R. Verkuil, V. Q. Tran, J. Deaton, M. Wiggert, R. Badkundri, I. Shafkat, J. Gong, A. Derry, R. S. Molina, N. Thomas, Y. A. Khan, C. Mishra, C. Kim, L. J. Bartie, M. Nemeth, P. D. Hsu, T. Sercu, S. Candido, and A. Rives. Simulating 500 million years of evolution with a language model. *Science*, 387 (6736):850–858, 2025.

- [21] K. Jiang, Z. Yan, M. Di Bernardo, S. R. Sgrizzi, L. Villiger, A. Kayabolen, B. Kim, J. K. Carscadden, M. Hiraizumi, H. Nishimasu, J. S. Gootenberg, and O. O. Abudayyeh. Rapid protein evolution by few-shot learning with a protein language model. *bioRxiv*, 2024: 2024.07.17.604015, 2024.
- [22] E. D. Vaishnav, C. G. de Boer, J. Molinet, M. Yassour, L. Fan, X. Adiconis, D. A. Thompson, J. Z. Levin, F. A. Cubillos, and A. Regev. The evolution, evolvability and engineering of gene regulatory DNA. *Nature*, 603(7901):455–463, 2022.
- [23] H. Yu, H. Yang, W. Sun, Z. Yan, X. Yang, H. Zhang, Y. Ding, and K. Li. An interpretable RNA foundation model for exploring functional RNA motifs in plants. *Nat. Mach. Intell.*, 6 (12):1616–1625, 2024.
- [24] Yang Tan, Ruilin Wang, Banghao Wu, Liang Hong, and Bingxin Zhou. Retrieval-enhanced mutation mastery: Augmenting zero-shot prediction of protein language model. *CoRR*, abs/2410.21127, 2024.
- [25] Li, Tan, Ma, Zhong, Yu, Zhou, Ouyang, Zhou, Tan, and Hong. Prosst: protein language modeling with quantized structure and disentangled attention. *NeurIPS'24: Proc. of Advances* in Neural Information Processing Systems, 38, 2024.
- [26] Groth, Kerrn, Olsen, Salomon, and Boomsma. Kermut: composite kernel regression for protein variant effects. NeurIPS'24: Proc. of Advances in Neural Information Processing Systems, 38, 2024.
- [27] N. Hollmann, S. Müller, L. Purucker, A. Krishnakumar, M. Körfer, S. B. Hoo, R. T. Schirrmeister, and F. Hutter. Accurate predictions on small data with a tabular foundation model. *Nature*, 637(8045):319–326, 2025.
- [28] Jiayang Chen, Zhihang Hu, Siqi Sun, Qingxiong Tan, Yixuan Wang, Qinze Yu, Licheng Zong, Liang Hong, Jin Xiao, Tao Shen, Irwin King, and Yu Li. Interpretable RNA foundation model from unannotated data for highly accurate RNA structure and function predictions. *arXiv*, 2204:00300, 2022.
- [29] Ning Wang, Jiang Bian, Yuchen Li, Xuhong Li, Shahid Mumtaz, Linghe Kong, and Haoyi Xiong. Multi-purpose RNA language modelling with motif-aware pretraining and type-guided fine-tuning. *Nat. Mach. Intell.*, 6(5):548–557, 2024.
- [30] Garyk Brixi, Matthew G. Durrant, Jerome Ku, Michael Poli, Greg Brockman, Daniel Chang, Gabriel A. Gonzalez, Samuel H. King, David B. Li, Aditi T. Merchant, Mohsen Naghipourfar, Eric Nguyen, Chiara Ricci-Tam, David W. Romero, Gwanggyu Sun, Ali Taghibakshi, Anton Vorontsov, Brandon Yang, Myra Deng, Liv Gorton, Nam Nguyen, Nicholas K. Wang, Etowah Adams, Stephen A. Baccus, Steven Dillmann, Stefano Ermon, Daniel Guo, Rajesh Ilango, Ken Janik, Amy X. Lu, Reshma Mehta, Mohammad R.K. Mofrad, Madelena Y. Ng, Jaspreet Pannu, Christopher Ré, Jonathan C. Schmok, John St. John, Jeremy Sullivan, Kevin Zhu, Greg Zynda, Daniel Balsam, Patrick Collison, Anthony B. Costa, Tina Hernandez-Boussard, Eric Ho, Ming-Yu Liu, Thomas McGrath, Kimberly Powell, Dave P. Burke, Hani Goodarzi, Patrick D. Hsu, and Brian L. Hie. Genome modeling and design across all domains of life with Evo 2. bioRxiv, 2025:2025.02.18.638918, 2025.
- [31] Pascal Notin, Aaron Kollasch, Daniel Ritter, Lood van Niekerk, Steffanie Paul, Han Spinner, Nathan J. Rollins, Ada Shaw, Rose Orenbuch, Ruben Weitzman, Jonathan Frazer, Mafalda Dias, Dinko Franceschi, Yarin Gal, and Debora S. Marks. Proteingym: Large-scale benchmarks for protein fitness prediction and design. In *NeurIPS'23: Proc. of Advances in Neural Information Processing Systems 36*, 2023.
- [32] Rohit Arora, Murphy Angelo, Christian Andrew Choe, Aaron W Kollasch, Fiona Qu, Courtney A. Shearer, Ruben Weitzman, Artem Gazizov, Sarah Gurev, Erik Xie, Debora Susan Marks, and Pascal Notin. RNAGym: benchmarks for RNA fitness and structure prediction. In *ICLR 2025 Workshop on Machine Learning for Genomics Explorations*, 2025.
- [33] David H. Wolpert and William G. Macready. No free lunch theorems for optimization. *IEEE Trans. Evol. Comput.*, 1(1):67–82, 1997.
- [34] C. A. Westmann, L. Goldbach, and A. Wagner. The highly rugged yet navigable regulatory landscape of the bacterial transcription factor TetR. *Nat. Commun.*, 15(1):10745, 2024.
- [35] Van Cleve J and Weissman DB. Measuring ruggedness in fitness landscapes. *Proc. Natl. Acad. Sci. U. S. A.*, 112(24):7345–7346, 2015.

- [36] Frank J. Poelwijk, Daan J. Kiviet, Daniel M. Weinreich, and Sander J. Tans. Empirical fitness landscapes reveal accessible evolutionary paths. *Nature*, 445(7126):383–386, 2007.
- [37] Claudia Bank. Epistasis and adaptation on fitness landscapes. *Annu. Rev. Ecol. Evol. Syst.*, 53: 457–479, 2022.
- [38] HH Chou, HC Chiu, NF Delaney, D Segrè, and CJ Marx. Diminishing returns epistasis among beneficial mutations decelerates adaptation. *Science*, 332(6034):1190–1192, 2011.
- [39] CW Bakerlee, AN Nguyen Ba, Y Shulgina, JI Rojas Echenique, and MM Desai. Idiosyncratic epistasis leads to global fitness-correlated trends. *Science*, 376(6593):630–635, 2022.
- [40] Jakub Otwinowski, David M. McCandlish, and Joshua B. Plotkin. Inferring the shape of global epistasis. *Proc. Natl. Acad. Sci. U. S. A.*, 115(32):E7550–E7558, 2018.
- [41] A. I. Khan, D. M. Dinh, D. Schneider, R. E. Lenski, and T. F. Cooper. Negative epistasis between beneficial mutations in an evolving bacterial population. *Science*, 332(6034):1193– 1196, 2011.
- [42] J. Domingo, G. Diss, and B. Lehner. Pairwise and higher-order genetic interactions during the evolution of a tRNA. *Nature*, 558(7708):117–121, 2018.
- [43] Andrew S. Lauring, Judith Frydman, and Raul Andino. The role of mutational robustness in RNA virus evolution. *Nat. Rev. Microbiol.*, 11(5):327–336, 2013.
- [44] Jeremy A. Draghi, Todd L. Parsons, Günter P. Wagner, and Joshua B. Plotkin. Mutational robustness can facilitate adaptation. *Nature*, 463(7279):353–355, 2010.
- [45] M. A. Félix and M. Barkoulas. Pervasive robustness in biological systems. *Nat. Rev. Genet.*, 16(8):483–496, 2015.
- [46] Matthew T. Weirauch, Alina Yang, Mihai Albu, Andre G. Cote, Andres Montenegro-Montero, Philipp Drewe, Hamed S. Najafabadi, Samuel A. Lambert, Ian Mann, Katie Cook, Hao Zheng, Andrea Goity, Harm van Bakel, Juan C. Lozano, Mary Galli, Matthew G. Lewsey, Eric Huang, Tathagata Mukherjee, Xianjun Chen, John S. Reece-Hoyes, Suganthi Govindarajan, Gad Shaulsky, Albertha J. M. Walhout, François-Yves Bouget, Gunnar Rätsch, Luis F. Larrondo, Joseph R. Ecker, and Timothy R. Hughes. Determination and inference of eukaryotic transcription factor sequence specificity. *Cell*, 158(6):1431–1443, September 2014.
- [47] Anna I. Podgornaia and Michael T. Laub. Pervasive degeneracy and epistasis in a protein-protein interface. *Science*, 347(6222):673–677, 2015.
- [48] T. Friedlander, R. Prizak, N. H. Barton, and G. Tkačik. Evolution of new regulatory functions on biophysically realistic fitness landscapes. *Nat. Commun.*, 8(1):216, 2017.
- [49] C. H. Yang and S. V. Scarpino. A family of fitness landscapes modeled through gene regulatory networks. *Entropy*, 24(5):622, 2022.
- [50] J. Kehe, A. Kulesa, A. Ortiz, C.M. Ackerman, S.G. Thakku, D. Sellers, S. Kuehn, J. Gore, J. Friedman, and P.C. Blainey. Massively parallel screening of synthetic microbial communities. *Proc. Natl. Acad. Sci. U.S.A.*, 116(26):12804–12809, 2019.
- [51] Juan Diaz-Colunga, Pablo Catalan, Magdalena San Roman, Andrea Arrabal, and Alvaro Sanchez. Full factorial construction of synthetic microbial communities. *eLife*, 13:RP101906, 2024.
- [52] Abigail Skwara, Karna Gowda, Mahmoud Yousef, Juan Diaz-Colunga, Arjun S. Raman, Alvaro Sanchez, Mikhail Tikhonov, and Seppe Kuehn. Statistically learning the functional landscape of microbial communities. *Nat. Ecol. Evol.*, 7:1823–1833, 2023.
- [53] Juan Diaz-Colunga, Abigail Skwara, Jean C.C. Vila, Djordje Bajic, and Alvaro Sanchez. Global epistasis and the emergence of function in microbial consortia. *Cell*, 187(12):3108–3119.e30, 2024.
- [54] A. Sanchez-Gorostiaga, D. Bajić, M.L. Osborne, J.F. Poyatos, and A. Sanchez. High-order interactions distort the functional landscape of microbial consortia. *PLoS Biol.*, 17(12): e3000550, 2019.
- [55] S Brouillet, H Annoni, L Ferretti, and G Achaz. MAGELLAN: a tool to explore small fitness landscapes. *bioRxiv*, 2015:031583, 2015.
- [56] Stuart Kauffman and Simon Levin. Towards a general theory of adaptive walks on rugged landscapes. *J. Theor. Biol.*, 128:11–45, 1987.

- [57] Roshan Rao, Nicholas Bhattacharya, Neil Thomas, Yan Duan, Xi Chen, John F. Canny, Pieter Abbeel, and Yun S. Song. Evaluating protein transfer learning with TAPE. In *NeurIPS'19: Proc. of Advances in Neural Information Processing Systems 32*, pages 9686–9698, 2019.
- [58] Christian Dallago, Jody Mou, Kadina E. Johnston, Bruce J. Wittmann, Nicholas Bhattacharya, Samuel Goldman, Ali Madani, and Kevin K. Yang. FLIP: benchmark tasks in fitness landscape inference for proteins. In *Proc. of the Neural Information Processing Systems Track on Datasets and Benchmarks* 1, 2021.
- [59] Nicholas C Wu, Lei Dai, C Anders Olson, James O Lloyd-Smith, and Ren Sun. Adaptation in protein fitness landscapes is facilitated by indirect paths. *eLife*, 5:e16965, 2016.
- [60] T. A. Hopf, J. B. Ingraham, F. J. Poelwijk, C. P. Schärfe, M. Springer, C. Sander, and D. S. Marks. Mutation effects predicted from sequence co-variation. *Nat. Biotechnol.*, 35(2): 128–135, 2017.
- [61] A. J. Riesselman, J. B. Ingraham, and D. S. Marks. Deep generative models of genetic variation capture the effects of mutations. *Nat. Methods*, 15(10):816–822, 2018.
- [62] S. Sumi, M. Hamada, and H. Saito. Deep generative design of RNA family sequences. *Nat. Methods*, 21(3):435–443, 2024.
- [63] E. Nguyen, M. Poli, M. G. Durrant, B. Kang, D. Katrekar, D. B. Li, L. J. Bartie, A. W. Thomas, S. H. King, G. Brixi, J. Sullivan, M. Y. Ng, A. Lewis, A. Lou, S. Ermon, S. A. Baccus, T. Hernandez-Boussard, C. Ré, P. D. Hsu, and B. L. Hie. Sequence modeling and design from molecular to genome scale with Evo. *Science*, 386(6723):eado9336, 2024.
- [64] Yuchen Ren, Zhiyuan Chen, Lifeng Qiao, Hongtai Jing, Yuchen Cai, Sheng Xu, Peng Ye, Xinzhu Ma, Siqi Sun, Hongliang Yan, Dong Yuan, Wanli Ouyang, and Xihui Liu. BEA-CON: benchmark for comprehensive RNA tasks and language models. *Proc. of the Neural Information Processing Systems Track on Datasets and Benchmarks*, 2024.
- [65] N. Hansen, A. Auger, R. Ros, O. Mersmann, T. Tušar, and D. Brockhoff. COCO: a platform for comparing continuous optimizers in a black-box setting. *Optim. Methods Softw.*, 36(1): 114–144, 2021.
- [66] Pascal Kerschke and Heike Trautmann. Comprehensive feature-based landscape analysis of continuous and constrained optimization problems using the R-package flacco. pages 93–123, 2019.
- [67] A. Liefooghe, F. Daolio, S. Verel, B. Derbel, H. Aguirre, and K. Tanaka. Landscape-aware performance prediction for evolutionary multiobjective optimization. *IEEE Trans. Evol. Comput.*, 24(6):1063–1077, 2020.
- [68] Pascal Kerschke and Heike Trautmann. Automated algorithm selection on continuous blackbox problems by combining exploratory landscape analysis and machine learning. *Evol. Comput.*, 27(1):99–127, 2019.
- [69] Pascal Kerschke, Holger H. Hoos, Frank Neumann, and Heike Trautmann. Automated algorithm selection: Survey and perspectives. *Evol. Comput.*, 27(1):3–45, 2019.
- [70] T. Aita, M. Iwakura, and Y. Husimi. A cross-section of the fitness landscape of dihydrofolate reductase. *Protein Eng.*, 14(9):633–638, 2001.
- [71] Edward Weinberger. Correlated and uncorrelated fitness landscapes and how to tell the difference. *Biol. Cybern.*, 63(5):325–336, 1990.
- [72] Luca Ferretti, Bastian Schmiegelt, Daniel Weinreich, Atsushi Yamauchi, Yutaka Kobayashi, Fumio Tajima, and Guillaume Achaz. Measuring epistasis in fitness landscapes: the correlation of fitness effects of mutations. *J. Theor. Biol.*, 396:132–143, 2016.
- [73] Andreas Wagner. Evolvability-enhancing mutations in the fitness landscapes of an RNA and a protein. *Nat. Commun.*, 14(1):3624, 2023.
- [74] P. C. Phillips. Epistasis—the essential role of gene interactions in the structure and evolution of genetic systems. *Nat. Rev. Genet.*, 9(11):855–867, 2008.
- [75] Matthew S. Johnson, Aleksej Martsul, Sergey Kryazhimskiy, and Michael M. Desai. Higher-fitness yeast genotypes are less robust to deleterious mutations. *Science*, 366(6464):490–493, 2019.

- [76] T. Jones and S. Forrest. Fitness distance correlation as a measure of problem difficulty for genetic algorithms. *Proc. Int. Conf. Genet. Algorithms*, 6:184–192, 1995.
- [77] Joshua L. Payne and Andreas Wagner. Mechanisms of mutational robustness in transcriptional regulation. *Front. Genet.*, 6:322, 2015.
- [78] A. S. B. Jalal, N. T. Tran, C. E. Stevenson, E. W. Chan, R. Lo, X. Tan, A. Noy, D. M. Lawson, and T. B. K. Le. Diversification of DNA-binding specificity by permissive and specificity-switching mutations in the ParB/Noc protein family. *Cell Rep.*, 32(3):107928, 2020.
- [79] Boqiang Tu, Vikram Sundar, and Kevin M. Esvelt. An ultra-high-throughput method for measuring biomolecular activities. bioRxiv, 2022.
- [80] Stuart A. Kauffman. The origins of order: self organization and selection in evolution. Oxford Univ Press, New York, 1993.
- [81] Edward D. Weinberger. Local properties of Kauffman's N-k model: a tunably rugged energy landscape. *Phys. Rev. A*, 44(10):6399–6413, 1991.
- [82] Kate Smith-Miles and Mario Andrés Muñoz. Instance space analysis for algorithm testing: Methodology and software tools. *ACM Comput. Surv.*, 55(12):255:1–255:31, 2023.
- [83] C. Hsu, H. Nisonoff, C. Fannjiang, and J. Listgarten. Learning protein fitness models from evolutionary and assay-labeled data. *Nat. Biotechnol.*, 40(7):1114–1122, 2022.
- [84] Russ W. P., Figliuzzi M., Stocker C., Barrat-Charlaix P., Socolich M., Kast P., Hilvert D., Monasson R., Cocco S., Weigt M., and Ranganathan R. An evolution-based model for designing chorismate mutase enzymes. *Science*, 369(6502):440–445, 2020.
- [85] A Rives, J Meier, T Sercu, S Goyal, Z Lin, J Liu, D Guo, M Ott, C L Zitnick, J Ma, and R Fergus. Biological structure and function emerge from scaling unsupervised learning to 250 million protein sequences. *Proc. Natl. Acad. Sci. U. S. A.*, 118(15):e2016239118, 2021.
- [86] K. Tsuboyama, J. Dauparas, J. Chen, E. Laine, Y. Mohseni Behbahani, J. J. Weinstein, N. M. Mangan, S. Ovchinnikov, and G. J. Rocklin. Mega-scale experimental analysis of protein folding stability in biology and design. *Nature*, 620(7973):434–444, 2023.
- [87] P. Notin, R. Weitzman, D. Marks, and Y. Gal. Proteinnpt: improving protein property prediction and design with non-parametric transformers. Adv. Neural Inf. Process. Syst., 36:33529–33563, 2023.
- [88] M. S. Packer and D. R. Liu. Methods for the directed evolution of proteins. *Nat. Rev. Genet.*, 16(7):379–394, 2015.
- [89] Y. Wang, P. Xue, M. Cao, T. Yu, S. T. Lane, and H. Zhao. Directed evolution: methodologies and applications. *Chem. Rev.*, 121(20):12384–12444, 2021.
- [90] B. J. Wittmann, Y. Yue, and F. H. Arnold. Informed training set design enables efficient machine learning-assisted directed protein evolution. *Cell Syst.*, 12(11):1026–1045.e7, 2021.
- [91] P. A. Romero, A. Krause, and F. H. Arnold. Navigating the protein fitness landscape with gaussian processes. *Proc. Natl. Acad. Sci. U. S. A.*, 110(3):E193–E201, 2013.
- [92] K. K. Yang, Z. Wu, and F. H. Arnold. Machine-learning-guided directed evolution for protein engineering. *Nat. Methods*, 16(8):687–694, 2019.
- [93] Z. Wu, S. B. J. Kan, R. D. Lewis, B. J. Wittmann, and F. H. Arnold. Machine learning-assisted directed protein evolution with combinatorial libraries. *Proc. Natl. Acad. Sci. U. S. A.*, 116 (18):8852–8858, 2019.
- [94] Y. Qiu, J. Hu, and G. W. Wei. Cluster learning-assisted directed evolution. *Nat. Comput. Sci.*, 1(12):809–818, 2021.
- [95] J. Yang, R. G. Lal, J. C. Bowden, R. Astudillo, M. A. Hameedi, S. Kaur, M. Hill, Y. Yue, and F. H. Arnold. Active learning-assisted directed evolution. *Nat. Commun.*, 16(1):714, 2025.
- [96] F. Pinheiro, O. Warsi, D. I. Andersson, and M. Lässig. Metabolic fitness landscapes predict the evolution of antibiotic resistance. *Nat. Ecol. Evol.*, 5(5):677–687, 2021.
- [97] I. L. Hofacker, W. Fontana, P. F. Stadler, L. S. Bonhoeffer, M. Tacker, and P. Schuster. Fast folding and comparison of RNA secondary structures. *Monatsh. Chem.*, 125:167–188, 1994.
- [98] K. A. Dill. Theory for the folding and stability of globular proteins. *Biochemistry*, 24(6): 1501–1509, 1985.

- [99] K. F. Lau and K. A. Dill. A lattice statistical mechanics model of the conformational and sequence spaces of proteins. *Macromol.*, 22(10):3986–3997, 1989.
- [100] S. F. Greenbury, I. G. Johnston, A. A. Louis, and S. E. Ahnert. A tractable genotype-phenotype map modelling the self-assembly of protein quaternary structure. *J. R. Soc. Interface*, 11(95): 20140249, 2014.
- [101] N. Altman and M. Krzywinski. The curse(s) of dimensionality. *Nat. Methods*, 15(6):399–400, 2018.
- [102] I. T. Jolliffe and J. Cadima. Principal component analysis: a review and recent developments. *Philos. Trans. A Math. Phys. Eng. Sci.*, 374(2065):20150202, 2016.
- [103] Laurens van der Maaten and Geoffrey Hinton. Visualizing data using t-SNE. *J. Mach. Learn. Res.*, 9(86):2579–2605, 2008.
- [104] Leland McInnes and John Healy. UMAP: uniform manifold approximation and projection for dimension reduction. *CoRR*, abs/1802.03426, 2018.
- [105] K. Zhang, N. R. Zemke, E. J. Armand, and B. Ren. A fast, scalable and versatile tool for analysis of single-cell omics data. *Nat. Methods*, 21(2):217–227, 2024.
- [106] J. Zhou and O. G. Troyanskaya. An analytical framework for interpretable and generalizable single-cell data analysis. *Nat. Methods*, 18(11):1317–1321, 2021.
- [107] L. Heumos, P. Ehmele, T. Treis, J. Upmeier Zu Belzen, E. Roellin, L. May, A. Namsaraeva, N. Horlava, V. A. Shitov, X. Zhang, L. Zappia, R. Knoll, N. J. Lang, L. Hetzel, I. Virshup, L. Sikkema, F. Curion, R. Eils, H. B. Schiller, A. Hilgendorff, and F. J. Theis. An open-source framework for end-to-end analysis of electronic health record data. *Nat. Med.*, 30(11): 3369–3380, 2024.
- [108] M. S. Keller, I. Gold, C. McCallum, T. Manz, P. V. Kharchenko, and N. Gehlenborg. Vitessce: integrative visualization of multimodal and spatially resolved single-cell data. *Nat. Methods*, 22(1):63–67, 2025.
- [109] Mingyu Huang, Shasha Zhou, Yuxin Chen, and Ke Li. Conversational exploration of literature landscape with litchat. In *IJCAI'25: Proc. of the 34th International Joint Conference on Artificial Intelligence*, volume in press, 2025.
- [110] Mingyu Huang and Ke Li. A survey of decomposition-based evolutionary multi-objective optimization: Part II A data science perspective. *CoRR*, abs/2404.14228, 2024.
- [111] Ke Li and Fan Li. Multi-fidelity methods for optimization: A survey. *CoRR*, abs/2402.09638, 2024.
- [112] D. J. Wales. Exploring energy landscapes. Annu. Rev. Phys. Chem., 69:401–425, 2018.
- [113] Mingyu Huang and Ke Li. Exploring structural similarity in fitness landscapes via graph data mining: A case study on number partitioning problems. In *IJCAI'23: Proc. of the 32nd International Joint Conference on Artificial Intelligence*, pages 5595–5603, 2023.
- [114] U. Chitra, B. Arnold, and B. J. Raphael. Resolving discrepancies between chimeric and multiplicative measures of higher-order epistasis. *Nat. Commun.*, 16(1):1711, 2025.
- [115] C. Bank, S. Matuszewski, R. T. Hietpas, and J. D. Jensen. On the (un)predictability of a large intragenic fitness landscape. *Proc. Natl. Acad. Sci. U. S. A.*, 113(49):14085–14090, 2016.
- [116] S. A. Fahlberg, C. R. Freschlin, P. Heinzelman, and P. A. Romero. Neural network extrapolation to distant regions of the protein fitness landscape. *Nat. Commun.*, 15(1):6405, 2024.
- [117] Angela M. Phillips, Katherine R. Lawrence, Alief Moulana, Thomas Dupic, Jeffrey Chang, Milo S. Johnson, Ivana Cvijovic, Thierry Mora, Aleksandra M. Walczak, and Michael M. Desai. Binding affinity landscapes constrain the evolution of broadly neutralizing anti-influenza antibodies. *eLife*, 10:e71393, 2021.
- [118] V. W. C. Soo, J. B. Swadling, A. J. Faure, and T. Warnecke. Fitness landscape of a dynamic RNA structure. *PLoS Genet.*, 17(2):e1009353, 2021.
- [119] R. L. Clark, B. M. Connors, and D. M. Stevenson. Design of synthetic human gut microbiome assembly and butyrate production. *Nat. Commun.*, 12:3254, 2021.

- [120] Stuart A. Kauffman and Edward D. Weinberger. The NK model of rugged fitness landscapes and its application to maturation of the immune response. *J. Theor. Biol.*, 141(2):211–245, 1989.
- [121] J. Arjan G. M. de Visser and Joachim Krug. Empirical fitness landscapes and the predictability of evolution. *Nat. Rev. Genet.*, 15(7):480–490, 2014.
- [122] Ivan G. Szendro, Martijn F. Schenk, Jasper Franke, Joachim Krug, and J. Arjan G. M. de Visser. Quantitative analyses of empirical fitness landscapes. J. Stat. Mech. Theory Exp., 2013(01): P01005, 2013.
- [123] Maurício Carneiro and Daniel L. Hartl. Adaptive landscapes and protein evolution. *Proc. Natl. Acad. Sci. U. S. A.*, 107(Suppl. 1):1747–1751, 2010.
- [124] John H. Gillespie. Molecular evolution over the mutational landscape. *Evolution*, 38(5): 1116–1129, 1984.
- [125] Christian Blum and Andrea Roli. Metaheuristics in combinatorial optimization: overview and conceptual comparison. *ACM Comput. Surv.*, 35(3):268–308, 2003.
- [126] L. Darrell Whitley, Adele E. Howe, and Doug Hains. Greedy or not? best improving versus first improving stochastic local search for MAXSAT. In *AAAI'13: Proc. of the 27th AAAI Conference on Artificial Intelligence*, pages 940–946, 2013.
- [127] Joshua L. Payne and Andreas Wagner. The causes of evolvability and their evolution. *Nat. Rev. Genet.*, 20(1):24–38, 2019.
- [128] Peter A. Cariani. Extradimensional bypass. *Biosyst.*, 64(1–3):47–53, 2002.
- [129] Sergey Kryazhimskiy, Daniel P. Rice, Eric R. Jerison, and Michael M. Desai. Global epistasis makes adaptation predictable despite sequence-level stochasticity. *Science*, 344(6191):1519– 1522, 2014.
- [130] Philip A. Romero and Frances H. Arnold. Exploring protein fitness landscapes by directed evolution. *Nat. Rev. Mol. Cell Biol.*, 10(12):866–876, 2009.
- [131] Daniel M. Lyons, Zhengting Zou, Haiqing Xu, and Jianzhi Zhang. Idiosyncratic epistasis creates universals in mutational effects and evolutionary trajectories. *Nat. Ecol. Evol.*, 4: 1685–1693, 2020.
- [132] Leandro Aguirre, Arielle Hendelman, Samantha F. Hutton, David M. McCandlish, and Zachary B. Lippman. Idiosyncratic and dose-dependent epistasis drives variation in tomato fruit size. *Science*, 382(6668):315–320, 2023.
- [133] T. F. Hansen and G. P. Wagner. Modeling genetic architecture: a multilinear theory of gene interaction. *Theor. Popul. Biol.*, 59(1):61–86, 2001.
- [134] D. M. Weinreich, Y. Lan, C. S. Wylie, and R. B. Heckendorn. Should evolutionary geneticists worry about higher-order epistasis? *Curr. Opin. Genet. Dev.*, 23(6):700–707, 2013.
- [135] Jörg Neidhart, István G. Szendro, and Joachim Krug. Adaptation in tunably rugged fitness landscapes: the rough mount Fuji model. *Genetics*, 198(2):699–721, 2014.
- [136] J. F. C. Kingman. A simple model for the balance between selection and mutation. *J. Appl. Probab.*, 15(1):1–12, 1978.
- [137] Toshio Aita, Hiroshi Uchiyama, Takashi Inaoka, Masahiro Nakajima, Tatsuya Kokubo, and Yoshiyuki Husimi. Analysis of a local fitness landscape with a model of the rough Mt. Fuji-type landscape: application to prolyl endopeptidase and thermolysin. *Biopolymers*, 54(1):64–79, 2000
- [138] Benedikt Schmiegelt and Joachim Krug. Evolutionary accessibility of modular fitness land-scapes. *J. Stat. Phys.*, 154(1):334–355, 2014.
- [139] P. Schuster, W. Fontana, P. F. Stadler, and I. L. Hofacker. From sequences to shapes and back: a case study in RNA secondary structures. *Proc. Biol. Sci.*, 255(1344):279–284, 1994.
- [140] J. Aguirre, J. M. Buldú, M. Stich, and S. C. Manrubia. Topological structure of the space of phenotypes: the case of RNA neutral networks. *PLoS One*, 6(10):e26324, 2011.
- [141] S. F. Greenbury, S. Schaper, S. E. Ahnert, and A. A. Louis. Genetic correlations greatly increase mutational robustness and can both reduce and enhance evolvability. *PLoS Comput. Biol.*, 12(3):e1004773, 2016.

- [142] I. G. Johnston, K. Dingle, S. F. Greenbury, C. Q. Camargo, J. P. K. Doye, S. E. Ahnert, and A. A. Louis. Symmetry and simplicity spontaneously emerge from the algorithmic nature of evolution. *Proc. Natl. Acad. Sci. U. S. A.*, 119(11):e2113883119, 2022.
- [143] A. Irbäck and C. Troein. Enumerating designing sequences in the HP model. *J. Biol. Phys.*, 28 (1):1–15, 2002.
- [144] E. Ferrada and A. Wagner. A comparison of genotype-phenotype maps for RNA and proteins. Biophys. J., 102(8):1916–1925, 2012.
- [145] H. Li, R. Helling, C. Tang, and N. Wingreen. Emergence of preferred structures in a simple model of protein folding. *Science*, 273(5275):666–669, 1996.
- [146] Tianqi Chen and Carlos Guestrin. Xgboost: A scalable tree boosting system. In KDD'16: Proc. of the 22nd ACM SIGKDD International Conference on Knowledge Discovery and Data Mining, pages 785–794. ACM, 2016.
- [147] S. Biswas, G. Khimulya, E. C. Alley, K. M. Esvelt, and G. M. Church. Low-n protein engineering with data-efficient deep learning. *Nat. Methods*, 18(4):389–396, 2021.
- [148] Yi Wang, Hui Tang, Lichao Huang, Lulu Pan, Lixiang Yang, Huanming Yang, Feng Mu, and Meng Yang. Self-play reinforcement learning guides protein engineering. *Nat. Mach. Intell.*, 5:845–860, 2023.
- [149] Joshua Meier, Roshan Rao, Robert Verkuil, Jason Liu, Tom Sercu, and Alexander Rives. Language models enable zero-shot prediction of the effects of mutations on protein function. In *NeurIPS'21: Proc. of Advances in Neural Information Processing Systems 34*, pages 29287–29303, 2021.
- [150] Zuobai Zhang, Pascal Notin, Yining Huang, Aurélie C. Lozano, Vijil Chenthamarakshan, Debora S. Marks, Payel Das, and Jian Tang. Multi-scale representation learning for protein fitness prediction. In *NeurIPS'24: Advances in Neural Information Processing Systems 38*, 2024.
- [151] Mustafa Tekpinar et al. Prescott: a population aware, epistatic and structural model accurately 575 predicts missense effect. medrxiv. 2024.
- [152] Timothy F. Truong Jr. and Tristan Bepler. Poet: A generative model of protein families as sequences-of-sequences. In *NeurIPS'23: Advances in Neural Information Processing Systems* 36, 2023.
- [153] Thomas Hayes, Roshan Rao, Halil Akin, Nicholas J Sofroniew, Deniz Oktay, Zeming Lin, Robert Verkuil, Vincent Q Tran, Jonathan Deaton, Marius Wiggert, et al. Simulating 500 million years of evolution with a language model. *Science*, page eads0018, 2025.
- [154] Matsvei Tsishyn, Pauline Hermans, Fabrizio Pucci, and Marianne Rooman. Residue conservation and solvent accessibility are (almost) all you need for predicting mutational effects in proteins. *bioRxiv*, pages 2025–02, 2025.
- [155] Céline Marquet, Michael Heinzinger, Tobias Olenyi, Christian Dallago, Kyra Erckert, Michael Bernhofer, Dmitrii Nechaev, and Burkhard Rost. Embeddings from protein language models predict conservation and variant effects. *Human genetics*, 141(10):1629–1647, 2022.
- [156] Jin Su, Chenchen Han, Yuyang Zhou, Junjie Shan, Xibin Zhou, and Fajie Yuan. Saprot: Protein language modeling with structure-aware vocabulary. In *ICLR'24: Proc. of the Twelfth International Conference on Learning Representations*. OpenReview.net, 2024.
- [157] Pascal Notin, Lood Van Niekerk, Aaron W Kollasch, Daniel Ritter, Yarin Gal, and Debora S Marks. Trancepteve: Combining family-specific and family-agnostic models of protein sequences for improved fitness prediction. *bioRxiv*, pages 2022–12, 2022.
- [158] Maxim Zvyagin, Alexander Brace, Kyle Hippe, Yuntian Deng, Bin Zhang, Cindy Orozco Bohorquez, Austin Clyde, Bharat Kale, Danilo Perez-Rivera, Heng Ma, et al. Genslms: Genome-scale language models reveal sars-cov-2 evolutionary dynamics. *The International Journal of High Performance Computing Applications*, 37(6):683–705, 2023.
- [159] Hugo Dalla-Torre, Liam Gonzalez, Javier Mendoza-Revilla, Nicolas Lopez Carranza, Adam Henryk Grzywaczewski, Francesco Oteri, Christian Dallago, Evan Trop, Bernardo P de Almeida, Hassan Sirelkhatim, et al. Nucleotide transformer: building and evaluating robust foundation models for human genomics. *Nature Methods*, 22(2):287–297, 2025.

- [160] Roshan Rao, Jason Liu, Robert Verkuil, Joshua Meier, John F. Canny, Pieter Abbeel, Tom Sercu, and Alexander Rives. MSA transformer. In *ICML'21: Proc. of the 38th International Conference on Machine Learning*, volume 139 of *Proceedings of Machine Learning Research*, pages 8844–8856. PMLR, 2021.
- [161] Pascal Notin, Mafalda Dias, Jonathan Frazer, Javier Marchena-Hurtado, Aidan N. Gomez, Debora S. Marks, and Yarin Gal. Tranception: Protein fitness prediction with autoregressive transformers and inference-time retrieval. In *ICML'22: Proc. of the International Conference* on Machine Learning, volume 162 of Proceedings of Machine Learning Research, pages 16990–17017. PMLR, 2022.
- [162] S. Langenheder, M.T. Bulling, M. Solan, and J.I. Prosser. Bacterial biodiversity-ecosystem functioning relations are modified by environmental complexity. *PLoS One*, 5(5):e10834, 2010.
- [163] Shih-Tsung Kuo, Regina L. Jahn, Yu-Ju Cheng, Yi-Lin Chen, Yen-Ju Lee, Florian Hollfelder, Jen-Der Wen, and Han-Dung Chou. Global fitness landscapes of the Shine-Dalgarno sequence. *Genome Res.*, 30(5):711–723, 2020.
- [164] Angela M Phillips, Daniel P Maurer, Caelan Brooks, Thomas Dupic, Aaron G Schmidt, and Michael M Desai. Hierarchical sequence-affinity landscapes shape the evolution of breadth in an anti-influenza receptor binding site antibody. *eLife*, 12:e83628, 2023.
- [165] Mandy S. Wong, Justin B. Kinney, and Adrian R. Krainer. Quantitative activity profile and context dependence of all human 5' splice sites. *Mol. Cell*, 71(6):1012–1026, 2018.
- [166] Alief Moulana, Thomas Dupic, and Angela M. Phillips. Compensatory epistasis maintains ACE2 affinity in SARS-CoV-2 Omicron BA.1. *Nat. Commun.*, 13:7011, 2022.
- [167] Alief Moulana, Thomas Dupic, Angela M. Phillips, Jeffrey Chang, Anne A. Roffler, Allison J. Greaney, Tyler N. Starr, Jesse D. Bloom, and Michael M. Desai. The landscape of antibody binding affinity in SARS-CoV-2 Omicron BA.1 evolution. *eLife*, 12:e83442, 2023.
- [168] D.P. Bendixsen, J. Collet, B. Østman, and E.J. Hayden. Genotype network intersections promote evolutionary innovation. *PLoS Biol.*, 17(5):e3000300, 2019.
- [169] F.J. Poelwijk, M. Socolich, and R. Ranganathan. Learning the pattern of epistasis linking genotype and phenotype in a protein. *Nat. Commun.*, 10:4213, 2019.
- [170] Thuy-Lan V Lite, Robert A Grant, Isabel Nocedal, Megan L Littlehale, Monica S Guo, and Michael T Laub. Uncovering the basis of protein-protein interaction specificity with a combinatorially complete library. *eLife*, 9:e60924, 2020.
- [171] Pablo Baeza-Centurion, Belén Miñana, Jörn M. Schmiedel, Juan Valcárcel, and Ben Lehner. Combinatorial genetics reveals a scaling law for the effects of mutations on splicing. *Cell*, 176 (3):549–563, 2019.
- [172] S. Schulz, T. J. C. Tan, N. C. Wu, and S. Wang. Epistatic hotspots organize antibody fitness landscape and boost evolvability. *Proc. Natl. Acad. Sci. U. S. A.*, 122(2):e2413884122, 2025.
- [173] N. C. Wu, J. Otwinowski, A. J. Thompson, C. M. Nycholat, A. Nourmohammad, and I. A. Wilson. Major antigenic site B of human influenza H3N2 viruses has an evolving local fitness landscape. *Nat. Commun.*, 11(1):1233, 2020.
- [174] Michael B. Doud, Animesh Gupta, Victor Li, Sarah J. Medina, Caesar A. De La Fuente, and Justin R. Meyer. Competition-driven eco-evolutionary feedback reshapes bacteriophage lambda's fitness landscape and enables speciation. *Nat. Commun.*, 15(1):863, 2024.
- [175] Kristina R. Hall, Katherine J. Robins, Emily M. Williams, Matthew H. Rich, Matthew J. Calcott, Jason N. Copp, Robert F. Little, Raphael Schwörer, Gregory B. Evans, Wayne M. Patrick, and David F. Ackerley. Intracellular complexities of acquiring a new enzymatic function revealed by mass-randomisation of active-site residues. *Elife*, 9:e59081, 2020.
- [176] Christian Fröhlich. On the evolvability of OXA-48. PhD thesis, UiT The Arctic University of Norway, 2021.
- [177] D. W. Hall, M. Agan, and S. C. Pope. Fitness epistasis among 6 biosynthetic loci in the budding yeast Saccharomyces cerevisiae. *J. Hered.*, 101(Suppl 1):S75–S84, 2010.

- [178] Yusuf T. Tamer, Izabela K. Gaszek, Hamed Abdizadeh, Tugce A. Batur, Kelly A. Reynolds, Ali R. Atilgan, Canan Atilgan, and Erdal Toprak. High-order epistasis in catalytic power of dihydrofolate reductase gives rise to a rugged fitness landscape in the presence of trimethoprim selection. *Mol. Biol. Evol.*, 36(7):1533–1550, 2019.
- [179] Eric R. Lozovsky, R. Frank Daniels, Gabriel D. Heffernan, David P. Jacobus, and Daniel L. Hartl. Relevance of higher-order epistasis in drug resistance. *Mol. Biol. Evol.*, 38(1):142–151, 2021.
- [180] A. E. Hall, K. Karkare, V. S. Cooper, C. Bank, T. F. Cooper, and F. B. Moore. Environment changes epistasis to alter trade-offs along alternative evolutionary paths. *Evolution*, 73(10): 2094–2105, 2019.
- [181] M. C. Whitlock and D. Bourguet. Factors affecting the genetic load in Drosophila: synergistic epistasis and correlations among fitness components. *Evolution*, 54(5):1654–1660, 2000.
- [182] J. A. de Visser, S. C. Park, and J. Krug. Exploring the effect of sex on empirical fitness landscapes. *Am. Nat.*, 174(Suppl 1):S15–S30, 2009.
- [183] J. da Silva, M. Coetzer, R. Nedellec, C. Pastore, and D. E. Mosier. Fitness epistasis and constraints on adaptation in a human immunodeficiency virus type 1 protein region. *Genetics*, 185(1):293–303, 2010.
- [184] Fredrik Sunden, Austin Peck, Julia Salzman, Simone Ressl, and Daniel Herschlag. Extensive site-directed mutagenesis reveals interconnected functional units in the alkaline phosphatase active site. *Elife*, 4:e06181, 2015.
- [185] Dane W. Anderson, Felix Baier, Guangfeng Yang, and Nobuhiko Tokuriki. The adaptive landscape of a metallo-enzyme is shaped by environment-dependent epistasis. *Nat. Commun.*, 12(1):3867, 2021.
- [186] P. M. Mira, K. Crona, D. Greene, J. C. Meza, B. Sturmfels, and M. Barlow. Rational design of antibiotic treatment plans: a treatment strategy for managing evolution and reversing resistance. *PLoS One*, 10(5):e0122283, 2015.
- [187] M. R. Meini, P. E. Tomatis, D. M. Weinreich, and A. J. Vila. Quantitative description of a protein fitness landscape based on molecular features. *Mol. Biol. Evol.*, 32(7):1774–1787, 2015.
- [188] E R Lozovsky, T Chookajorn, K M Brown, M Imwong, P J Shaw, S Kamchonwongpaisan, D E Neafsey, D M Weinreich, and D L Hartl. Stepwise acquisition of pyrimethamine resistance in the malaria parasite. *Proc. Natl. Acad. Sci. U.S.A.*, 106(29):12025–12030, 2009.
- [189] Peijie Jiang, Istvan Keren, Katherine G. O'Loughlin, Susan P. Sater, Shweta S. More, Jayson S. Loll, and Daniel M. Weinreich. Accessible mutational trajectories for the evolution of Pyrimethamine resistance in the malaria parasite Plasmodium vivax. *J. Mol. Evol.*, 86(7): 495–508, 2018.
- [190] C. B. Ogbunugafor. The mutation effect reaction norm (mu-rn) highlights environmentally dependent mutation effects and epistatic interactions. *Evolution*, 76:37–48, 2022.
- [191] K. M. Flynn, T. F. Cooper, F. B. Moore, and V. S. Cooper. The environment affects epistatic interactions to alter the topology of an empirical fitness landscape. *PLoS Genet.*, 9(4):e1003426, 2013.
- [192] B. A. Malcolm, K. P. Wilson, B. W. Matthews, J. F. Kirsch, and A. C. Wilson. Ancestral lysozymes reconstructed, neutrality tested, and thermostability linked to hydrocarbon packing. *Nature*, 345(6270):86–89, 1990.
- [193] R. F. Guerrero, S. V. Scarpino, J. V. Rodrigues, D. L. Hartl, and C. B. Ogbunugafor. Proteostasis environment shapes higher-order epistasis operating on antibiotic resistance. *Genetics*, 212(2): 565–575, 2019.

NeurIPS Paper Checklist

1. Claims

Question: Do the main claims made in the abstract and introduction accurately reflect the paper's contributions and scope?

Answer: [Yes]

Justification: As stated in the abstract and introduction, the main scope of this paper is biological fitness prediction, in particular the benchmark of methods for this topic. The main contribution of this paper is the development of the GraphFLA framework to make performance benchmarks more interpretable and insightful by considering fitness landscape features. This paper also contributes to the collection of a new set of 155 combinatorially complete fitness landscapes across DNA, RNA, and protein.

2. Limitations

Question: Does the paper discuss the limitations of the work performed by the authors?

Answer: [Yes]

Justification: We discussed the limitations of GraphFLA in Appendix A.

3. Theory assumptions and proofs

Question: For each theoretical result, does the paper provide the full set of assumptions and a complete (and correct) proof?

Answer: [NA]

Justification: The paper does not include any theoretical results.

4. Experimental result reproducibility

Question: Does the paper fully disclose all the information needed to reproduce the main experimental results of the paper to the extent that it affects the main claims and/or conclusions of the paper (regardless of whether the code and data are provided or not)?

Answer: [Yes]

Justification: All experimental setups are clearly described in either Section 4 or in corresponding Appendix sections.

5. Open access to data and code

Question: Does the paper provide open access to the data and code, with sufficient instructions to faithfully reproduce the main experimental results, as described in supplemental material?

Answer: [Yes]

Justification: All the artifacts needed to reproduce the experiments, including code for GraphFLA and the 155 combinatorially complete fitness landscapes data, are available in https://github.com/COLA-Laboratory/GraphFLA. We also used previously published benchmark results from ProteinGym, which is available at https://proteingym.org/. We are currently unable to share the RNAGym data and benchmark scores without permission from the original authors.

6. Experimental setting/details

Question: Does the paper specify all the training and test details (e.g., data splits, hyper-parameters, how they were chosen, type of optimizer, etc.) necessary to understand the results?

Answer: [Yes]

Justification: Relevant information are available in Section 4 and Appendix F.

7. Experiment statistical significance

Question: Does the paper report error bars suitably and correctly defined or other appropriate information about the statistical significance of the experiments?

Answer: [Yes]

Justification: The experimental results are accompanied by confidence intervals and statistical significance tests.

8. Experiments compute resources

Question: For each experiment, does the paper provide sufficient information on the computer resources (type of compute workers, memory, time of execution) needed to reproduce the experiments?

Answer: [Yes]

Justification: Section 4.1 provides sufficient details regarding computation hardware used as well as the runtime & memory scalability of GraphFLA.

9. Code of ethics

Question: Does the research conducted in the paper conform, in every respect, with the NeurIPS Code of Ethics https://neurips.cc/public/EthicsGuidelines?

Answer: [Yes]

Justification: The authors have ensured that all aspects of the research adhere to the NeurIPS Code of Ethics.

10. Broader impacts

Question: Does the paper discuss both potential positive societal impacts and negative societal impacts of the work performed?

Answer: [NA]

Justification: No negative social impact is related to this work.

11. Safeguards

Question: Does the paper describe safeguards that have been put in place for responsible release of data or models that have a high risk for misuse (e.g., pretrained language models, image generators, or scraped datasets)?

Answer: [NA]

Justification: The paper poses no such risks.

12. Licenses for existing assets

Question: Are the creators or original owners of assets (e.g., code, data, models), used in the paper, properly credited and are the license and terms of use explicitly mentioned and properly respected?

Answer: [Yes]

Justification: The paper properly credits the creators of the assets and mentions the license and terms of use.

13. New assets

Question: Are new assets introduced in the paper well documented and is the documentation provided alongside the assets?

Answer: [Yes]

Justification: All assets are available in https://github.com/COLA-Laboratory/GraphFLA.

14. Crowdsourcing and research with human subjects

Question: For crowdsourcing experiments and research with human subjects, does the paper include the full text of instructions given to participants and screenshots, if applicable, as well as details about compensation (if any)?

Answer: [NA]

Justification: The paper does not involve crowdsourcing nor research with human subjects

15. Institutional review board (IRB) approvals or equivalent for research with human subjects

Question: Does the paper describe potential risks incurred by study participants, whether such risks were disclosed to the subjects, and whether Institutional Review Board (IRB) approvals (or an equivalent approval/review based on the requirements of your country or institution) were obtained?

Answer: [NA]

Justification: The paper does not involve crowdsourcing nor research with human subjects

16. Declaration of LLM usage

Question: Does the paper describe the usage of LLMs if it is an important, original, or non-standard component of the core methods in this research? Note that if the LLM is used only for writing, editing, or formatting purposes and does not impact the core methodology, scientific rigorousness, or originality of the research, declaration is not required.

Answer: [Yes]

Justification: The authors declare the usage of LLMs in Section 3 and Appendix B.

A Limitations

While GraphFLA provides extensive quantitative features for characterizing fitness landscapes, effectively visualizing their topography remains challenging due to the inherent high dimensionality and associated curse of dimensionality [101]. Dimensionality reduction methods, such as PCA [102], t-SNE [103], and UMAP [104], partially address this issue and have been effectively applied to diverse biological data [105–108]. However, these methods risk generating misleading visualizations of fitness landscapes. Specifically, compressing data into fewer dimensions inevitably leads to loss of information, potentially distorting spatial relationships among variants. Although this might be acceptable for general visualization purposes—where overall data trends remain intact—such distortions can result in the incorrect identification of local optima that do not exist in the original high-dimensional space. Consequently, despite the intuitive appeal of visualizing fitness landscape topography, GraphFLA, along with much of the landscape analysis literature, emphasizes quantitative metrics that inherently capture patterns within high-dimensional spaces.

Additionally, despite extensive optimization efforts, the scale of landscapes analyzable by GraphFLA within practical computational times remains small compared to the entire genotype space. For instance, the number of potential RNA sequences of length n=100 is 4^{100} , vastly exceeding the number of atoms in the observable universe. Nonetheless, by efficiently handling landscapes containing millions of variants, GraphFLA aligns well with current experimental capabilities, and can comfortably accommodate even the largest empirically measured fitness landscapes.

B Data-driven Literature Survey on Landscape Analysis

Building on our prior success in leveraging data-driven methods and large language models (LLMs) to enhance literature comprehension [109–111], we adopted a similar strategy in the development of GraphFLA. This involved conducting an extensive literature survey designed to: (1) identify key landscape features that characterize their topography, and (2) gather empirical data for combinatorially complete fitness landscapes. The methodology encompassed several distinct stages:

B.1 Initial Literature Collection and Filtering

Search Query Formulation. The initial step involved crafting a targeted search query to retrieve literature pertinent to fitness landscapes. This topic is central to research where landscape features and combinatorially complete datasets are developed or utilized. The formulated query was:

```
(("fitness landscape*" OR "adaptive landscape*" OR "genotype network" OR "genotype-phenotype map*") OR ("epistasis" OR "diminishing return*" OR "increasing cost*" OR "NK landscape*"))
```

This query is structured with two primary components:

- 1. The first component utilizes established terminology for fitness landscapes (e.g., "fitness landscape", "adaptive landscape") and associated concepts (e.g., "genotype network", "genotype-phenotype mapping") to ensure a broad capture of relevant studies.
- 2. The second component augments the search by incorporating specific terms frequently used in biological landscape analysis, such as "epistasis" and "NK landscape".

While other relevant concepts exist (e.g., local optima, r/s ratio, see Appendix C), terms like "local optima" are prevalent across diverse optimization fields, making them less specific. Similarly, terms like "r/s ratio" can be challenging for effective textual matching. Consequently, these were excluded from the initial query. This search strategy deliberately prioritized high recall, acknowledging that it might retrieve studies from related domains (e.g., energy landscapes in physics/chemistry [112], optimization landscapes in evolutionary computation [113]). Distinguishing these fields solely through keywords is often infeasible due to their broad scopes; therefore, subsequent filtering steps were planned to refine the selection for biological relevance.

Database Search. The formulated search query was executed on the Web of Science database¹. This platform was chosen for its comprehensive coverage of peer-reviewed literature and high-quality

¹https://www.webofscience.com

metadata. To enhance the precision of the initial retrieval and minimize noise from full-text searches (such as incidental mentions of keywords), the search scope was restricted to the title, abstract, and author keywords fields. These sections typically encapsulate the core subject matter of a publication.

LLM-based Filtering. This initial search yielded a substantial corpus of 31, 784 potentially relevant publications. To manage this volume and efficiently identify studies most pertinent to our research scope, we employed an LLM—specifically GPT-4o-mini—for automated initial screening. The title and abstract of each publication were processed by the LLM, which was prompted to classify the study based on two primary criteria:

- 1. Does the publication investigate fitness landscapes or closely related concepts specifically within biological systems?
- 2. If the answer to the first criterion is affirmative, does the publication report on empirical data, as opposed to being a purely theoretical analysis, *in-silico* simulation study, or review article?

This LLM-driven filtering process significantly narrowed the candidate pool. After applying the first criterion, the number of papers was reduced to 11,098. The second criterion further refined this set to 1,673 publications. This curated collection of papers, focusing on analysis of empirically measured fitness landscapes in biological systems, formed the basis for subsequent landscape feature set construction and the collection of combinatorially complete landscape data.

B.2 Landscape Feature Set Construction

Following the identification of 1,673 core publications relevant to empirical fitness landscape analysis, we proceeded to construct a comprehensive and representative set of landscape features. The objective was to distill a manageable yet informative collection of quantitative indicators that capture the fundamental topographical aspects of fitness landscapes.

Initial Feature Candidate Identification. The full texts of the 1,673 curated papers were systematically reviewed to identify all quantitative measures used to describe landscape topography. This extensive survey, augmented by an LLM (GPT-40) to scan for mentions and definitions of landscape metrics, initially yielded a broad list of over 100 candidate features. These candidates encompassed a wide range of mathematical formulations, statistical measures, and network-based properties that researchers have employed to characterize landscapes.

LLM-assisted Feature Filtering and Selection. To refine this extensive list into a practical and impactful feature set, we devised a set of carefully crafted criteria to guide selection:

- 1. **Empirical prevalence in literature:** How frequently is the feature used or discussed in the surveyed 1,673 papers? Features with high prevalence were prioritized as they represent established and widely accepted indicators. The number of local optima are employed in 45% of our analyzed literature.
- 2. **Biological significance:** Does the feature provide meaningful insights into evolutionary processes or other biological phenomena? Features with clear connections to biological interpretations were favored. For instance, features quantifying aspects like diminishing returns epistasis can shed light on the rate of adaptation [38], while measures related to neutrality can have great biological implications for understanding mutational robustness [43].
- 3. Coverage across different topographical aspects: Does the feature contribute to characterizing one of the 4 fundamental topographical aspects: ruggedness, navigability, epistasis, and neutrality? We aimed for a balanced set that provides a holistic view of the landscape.
- 4. **Computational feasibility:** Can the feature be computed efficiently for landscapes of varying sizes and complexities, such as those included in GraphFLA? Features requiring prohibitive computational resources for typical dataset sizes were deprioritized. For example, while the Walsh-Hadamard transform [114] can be used to calculate a full spectrum of epistatic interactions, its computational demand can be prohibitive for large landscapes.
- 5. Compatibility with data modalities, Sizes, and Structures: Is the feature applicable to the types of data commonly found in empirical fitness landscapes? Is it robust to missing data or variations in landscape size? Features with broad applicability and robustness were preferred.

Final feature set. By manual reviewing the initial set of features along with expert consultations, we arrived at the final set of 20 essential landscape features presented in Table 1, which cover all 4 fundamental aspects of landscape topography and are extensively used in landscape analysis literature to offer different biological insights. They can also be efficiently computed for empirical landscapes with different modalities and sizes, and are applicable to non-complete landscapes. A full introduction to each of these 20 features, including their definitions, interpretations, and computational considerations, is available in Appendix C.

B.3 Combinatorially Complete Landscape Collection

In GraphFLA, we focused on collecting combinatorially complete datasets derived from extensive mutagenesis studies. Unlike datasets generated by randomly sampling mutants around a wild-type sequence, combinatorially complete landscapes encompass measurements for all possible genotypes within a defined genotype space. We identified and collected such datasets from our focused set of 1,673 papers via manual scrutiny of the full-texts with the aid of GPT-40. Specifically, for each paper, we asked:

- Does the publication publishes new empirical landscape data?
 - → If yes, was the published data combinatorially complete? This criterion specifically excludes datasets focusing only on evolutionary trajectories (i.e., monitoring changes in population mean fitness and genotypic composition) or deep mutational scanning data (i.e., sampling only mutants closely related to a wild-type sequence).
 - → If no, did it mention or use combinatorially complete datasets from previous works?

After this final review, we arrived at a total of 155 datasets as listed in Table A3, sourced from more than 67 studies. This number is much smaller compared to the initial corpus of over 30,000 papers. The main reason for this is such combinatorially complete landscapes are extremely costly to construct. Consequently, they are regarded as extremely valuable resources and are extensively utilized in subsequent works for both deriving biological insights [115, 73] and testing ML systems [95, 116, 58].

B.4 Datasets Processing.

Here we describe a few standards we applied when preparing these data.

Naming convention. We established a systematic naming convention to uniquely and informatively identify each dataset within the collection, following these guidelines:

- Base identifier: The core of the name typically consists of the first author's last name concatenated with the four-digit publication year (e.g., "Papkou2024").
- Common name suffix: If a dataset is widely recognized by a common identifier, often related to the specific biological system or molecule studied, this identifier may be appended as a suffix for easier recognition. For instance, the study by Wu et al. [59] investigated the fitness landscape across $20^4 = 160,000$ variants at four sites (V39, D40, G41, V54) within protein G domain B1 (GB1). This landscape is commonly referred to as "GB1," and thus the dataset might be named incorporating this suffix (e.g., "Wu2016_GB1").
- **Disambiguation suffixes:** Additional suffixes are employed when a single publication or study system yields multiple distinct datasets. These suffixes serve to differentiate datasets based on key experimental variables, such as:
 - Different subjects and fitness measures (e.g., Phillips et al. [117] studied binding
 affinities of different variants of antibodies CR9114 and CR6261 against various
 influenza HA antigens like H1, H3, etc., which results in separate datasets per antibodyantigen pair).
 - Variations in experimental conditions or environments (e.g., Soo et al. [118] measured the self-splicing activity of $4^8=65,536$ Tetrahymena intron variants at two different temperatures, 30°C and 37°C , leading to two distinct datasets).
 - Exploration of different mutation sites or regions (e.g., Johnston et al. [7] generated the "TrpB3D" landscape from $20^3 = 8,000$ variants at sites {T117, A118, A119} of the thermostable tryptophan synthase β -subunit (TrpB), and the distinct "TrpB3E" landscape based on sites {F184, G185, S186}).

- A combination of the above factors.

These distinguishing characteristics are systematically incorporated into the dataset name as further suffixes to ensure clarity and uniqueness.

Search space representation. Genotypes within each dataset are presented using two formats: a sequence-based representation (e.g., "ATTA") and a vector explicitly listing the allele at each locus (e.g., ["A", "T", "T", "A"]). The combinatorial nature of these representations leads to vast theoretical search spaces. For a sequence of length L, the total number of possible genotypes is 4^L for DNA or RNA, 20^L for proteins, or 2^L for binary representations. Binary representations typically indicate the presence or absence of specific mutations and can be applied to DNA, RNA, proteins, or other biological systems, such as microbial communities [52, 119]. Although the theoretical search spaces for our collected landscapes are combinatorially complete by design, the experimentally generated data often exhibit incomplete coverage due to experimental constraints or subsequent filtering steps. For example, the DHFR landscape from Papkou et al. [4] measured fitness for 261, 382 variants, which constitutes 99.7% of the total $4^9 = 262, 144$ possible genotypes. Similarly, the GB1 protein landscape reported by Wu et al. [59] includes 149, 361 variants, covering 93.4% of the theoretical space of $20^4 = 160,000$ sequences.

Fitness measure. Following our naming convention, each of the 155 dataset listed in Table A3 focuses on a single fitness measure under a given condition (e.g., environment). To ensure the potential for accurate landscape reconstruction and the replication of published analysis results, we have retained the original fitness values as reported in the source publications. No transformations were applied to these values unless such transformations were already part of the published dataset. For datasets where fitness variance across replications is available, this is amended as an additional column.

C Fitness Landscape Features

Core Definitions

We begin by defining fundamental concepts used throughout the fitness landscape analysis.

Definition C.1 (Alleles and Loci). Let n be the number of polymorphic loci under consideration. For each locus $i \in \{1, 2, ..., n\}$, let A_i denote the set of distinct alleles present. The number of alleles at locus i is $m_i = |A_i| > 2$.

Example 1. For example, in complete DNA or RNA landscapes, A_i typically contains four nucleotide bases ($\{A, C, G, T\}$ for DNA, $\{A, C, G, U\}$ for RNA), thus $m_i = |A_i| = 4$. For proteins, where loci usually represent amino acid positions, A_i comprises the 20 standard amino acids, resulting in $m_i = |A_i| = 20$.

Definition C.2 (Genotype Space). A genotype g is a specific combination of alleles across all n loci, represented as a sequence (a_1, a_2, \ldots, a_n) where $a_i \in \mathcal{A}_i$ for each i. The set of all possible genotypes constitutes the genotype space \mathcal{G} . The total number of genotypes is $|\mathcal{G}| = \prod_{i=1}^n m_i$.

Definition C.3 (Hamming Distance). The Hamming (genetic) distance $d_H(g,g')$ between two genotypes $g=(a_1,\ldots,a_n)$ and $g'=(a'_1,\ldots,a'_n)$ is the number of loci at which their alleles differ:

$$d_H(g, g') = \sum_{i=1}^n \mathbb{I}(a_i \neq a'_i),$$

where $\mathbb{I}(\cdot)$ is the indicator function ($\mathbb{I}(condition) = 1$ if the condition is true, 0 otherwise).

Definition C.4 (Mutational Neighborhood). The neighborhood $\mathcal{N}(g)$ of a genotype $g \in \mathcal{G}$ is the set of all genotypes reachable from g by a single point mutation, i.e., genotypes g' differing from g at exactly one locus:

$$\mathcal{N}(g) = \{ g' \in \mathcal{G} \mid d_H(g, g') = 1 \}.$$

The size of the neighborhood is $|\mathcal{N}(g)| = \sum_{i=1}^{n} (m_i - 1)$.

Definition C.5 (Fitness Function). The fitness function $f: \mathcal{G} \to \mathbb{R}$ assigns a scalar fitness value f(g) to each genotype $g \in \mathcal{G}$.

Definition C.6 (Mutant Genotype Notation). Let $g = (a_1, \ldots, a_j, \ldots, a_n)$. We denote the specific single-mutant neighbor resulting from changing the allele a_j at locus j to a different allele $a'_j \in A_j \setminus \{a_j\}$ as $g_{[j \leftarrow a'_j]}$. When the specific mutated allele a'_j is not critical or is clear from context (e.g., in biallelic systems where the alternative allele is unique), we may use the shorthand $g_{[j]}$ to denote any single mutant differing from g only at locus j.

Definition C.7 (Selection Coefficient). Let g be a genotype with allele a_j at locus j. The selection coefficient $s_{j,a_j \to a'_j}(g)$ measures the fitness effect of mutating allele a_j to a'_j (where $a'_j \in \mathcal{A}_j \setminus \{a_j\}$) at locus j within the genetic background of g:

$$s_{j,a_j \to a'_j}(g) = f(g_{[j \leftarrow a'_i]}) - f(g).$$

When the specific mutation $a_j \to a'_j$ is unambiguous or when referring generally to the effect of a mutation at locus j, we may use the simpler notation $s_j(g) = f(g_{[j]}) - f(g)$.

C.1 Ruggedness

C.1.1 Number of Local Optima

Definition C.8 (Local and Global Optima). A genotype $g^{\ell} \in \mathcal{G}$ is a **local optimum** if its fitness is greater than or equal to that of all its neighbors: $f(g^{\ell}) \geq f(g')$ for all $g' \in \mathcal{N}(g^{\ell})$. A **global optimum** g^* is a genotype with the maximum fitness across the entire landscape: $g^* \in \arg\max_{g \in \mathcal{G}} f(g)$. We generally assume a unique global optimum for simplicity, although the concepts readily extend to scenarios with multiple global optima.

The number of local optima, $n_{\rm lo}$, serves as a primary indicator of landscape ruggedness [4]. A smooth landscape possesses only a single local optimum, which coincides with the global optimum. In contrast, highly rugged landscapes, such as Kauffman's NK model [120] with k=n-1 interactions, can feature a large number of local optima, potentially scaling exponentially with system size (e.g., approximately $\frac{2^n}{n+1}$ local optima for certain NK parameters [81]).

In the graph-based representation employed by GraphFLA, where directed edges implicitly encode fitness comparisons between neighboring genotypes, local optima correspond directly to sink nodes (i.e., nodes with no outgoing edges). These sinks can be efficiently identified using standard graph algorithms (e.g., via the igraph library). To facilitate comparisons between landscapes of varying sizes, the absolute number of local optima is often normalized by the total number of genotypes, $|\mathcal{G}| = \prod_{i=1}^n m_i$. This yields the dimensionless quantity fraction of local optima.

C.1.2 Autocorrelation

Autocorrelation assesses the smoothness or ruggedness of a fitness landscape by measuring the correlation between the fitness values of genotypes encountered along random walks [71, 121]. Specifically, consider a random walk g_0, g_1, \ldots, g_L of length L through the genotype space \mathcal{G} , where each step g_{t+1} is typically chosen uniformly at random from the neighbors $\mathcal{N}(g_t)$. The lag-k autocorrelation $\rho_a(k)$ is defined as:

$$\rho_a(k) = \frac{\mathbb{E}[(f(g_t) - \langle f \rangle)(f(g_{t+k}) - \langle f \rangle)]}{\operatorname{Var}[f(g_t)]}$$
(A1)

where the expectation $\mathbb{E}[\cdot]$ and variance $\text{Var}[\cdot]$ are taken over all valid time steps t (and potentially multiple walks), and $\langle f \rangle$ represents the average fitness value across all considered steps g_t .

The primary focus is often on the lag-1 autocorrelation, $\rho_a(1)$ (simplified as ρ_a), which measures the fitness correlation between genotypes separated by a single mutation (Hamming distance 1).

In practice, GraphFLA estimates ρ_a by simulating a large number $(N_{walks}, \text{e.g.}, 1,000)$ of independent random walks, each of length L. A common choice for the walk length is L=n, where n is the number of loci. The covariance term (numerator) and variance term (denominator) in Eq. A1 are estimated by averaging over all adjacent pairs (g_t, g_{t+1}) across all simulated walks. Averaging over multiple walks provides a robust estimate.

A value of ρ_a close to 1 indicates a smooth landscape where fitness changes gradually between neighboring genotypes. Conversely, ρ_a values close to 0 suggest a rugged landscape where the fitness of neighbors is largely uncorrelated, implying rapid and unpredictable fitness changes.

C.1.3 Neighbor Fitness Correlation (NFC)

Another intuitive measure of landscape ruggedness assesses the relationship between a genotype's fitness and the average fitness of its mutational neighbors. This evaluates the tendency for high-fitness genotypes to be surrounded by neighbors that also have high fitness, and conversely for low-fitness genotypes.

Specifically, we compute the Pearson correlation coefficient, denoted $\rho_{f,\langle f\rangle_{\mathcal{N}}}$, between the fitness f(g) of each genotype $g\in\mathcal{G}$ and the average fitness of its neighborhood $\langle f\rangle_{\mathcal{N}(g)}$:

$$NFC = Cor \left[f(g), \langle f \rangle_{\mathcal{N}(g)} \right], \tag{A2}$$

where $\langle f \rangle_{\mathcal{N}(g)}$ is the mean fitness over all single-mutant neighbors of g:

$$\langle f \rangle_{\mathcal{N}(g)} = \frac{1}{|\mathcal{N}(g)|} \sum_{g' \in \mathcal{N}(g)} f(g').$$
 (A3)

The correlation in Eq. (A2) is calculated across all genotypes $g \in \mathcal{G}$ in the landscape.

This neighbor fitness correlation provides insight into the local smoothness or ruggedness of the landscape structure:

- A value of NFC ≈ 1 indicates a relatively smooth landscape where fitness changes tend to be gradual; high-fitness genotypes are typically surrounded by other high-fitness genotypes.
- A value of NFC ≈ 0 suggests a rugged landscape where a genotype's fitness provides little predictive power for its neighbors' fitness, indicating abrupt changes.
- A value of NFC ≈ -1, though less common, would imply an anticorrelated or oscillatory landscape structure where high-fitness genotypes are predomiNaNtly surrounded by lowfitness neighbors, and vice versa.

This measure focuses specifically on the fitness relationship between immediate neighbors, and complements measures like autocorrelation (C.1.2) which consider correlations along walks.

C.1.4 Roughness-Slope Ratio (r/s)

The roughness-slope ratio (r/s) quantifies the deviation of a fitness landscape from a purely additive model, thereby measuring the relative contribution of epistasis to the landscape structure [122, 123]. It is defined as the ratio of the landscape's 'roughness' (r), representing the magnitude of non-additive effects (residuals from an additive fit), to its 'slope' (s), representing the average magnitude of additive effects. A higher r/s value indicates greater ruggedness and stronger relative epistasis, while r/s=0 corresponds to a perfectly additive (non-epistatic) landscape.

To compute r/s, an additive fitness model $f^{\mathrm{add}}(g)$ is fitted to the observed fitness data f(g) using ordinary least squares (OLS) regression. For multi-allelic landscapes, genotypes are typically represented using one-hot encoding. The additive model is generally specified as:

$$f^{\text{add}}(g) = \beta_0 + \sum_{i=1}^n \sum_{a \in \mathcal{A}'_i} \beta_{i,a} X_{i,a}(g),$$
 (A4)

where $X_{i,a}(g)$ is a binary indicator variable (1 if genotype g has allele a at locus i, 0 otherwise), β_0 is the intercept, and $\beta_{i,a}$ are the fitted coefficients representing the additive effect of allele a at locus i relative to a reference allele. The inner sum $\sum_{a \in \mathcal{A}'_i}$ typically runs over $m_i - 1$ alleles for each locus i (excluding one reference allele per locus, denoted implicitly by \mathcal{A}'_i) to ensure model identifiability.

The roughness r is defined as the root-mean-square error (RMSE) between the true fitness values f(g) and the fitness predicted by the additive model $f^{\text{add}}(g)$:

$$r = \sqrt{\frac{1}{|\mathcal{G}|} \sum_{g \in \mathcal{G}} (f(g) - f^{\text{add}}(g))^2}.$$
 (A5)

The slope s is calculated as the average absolute value of the estimated additive coefficients (excluding the intercept and reference allele coefficients, which are implicitly zero or absorbed):

$$s = \frac{1}{\sum_{k=1}^{n} (m_k - 1)} \sum_{i=1}^{n} \sum_{a \in \mathcal{A}'_i} |\beta_{i,a}|.$$
 (A6)

Here, the denominator $\sum_{k=1}^{n}(m_k-1)$ represents the total number of independent additive coefficients fitted in the model (one for each non-reference allele across all loci), and the summation $\sum_{a\in\mathcal{A}_i'}$ covers these specific fitted coefficients for locus i.

The r/s ratio thus provides a scale-independent measure comparing the magnitude of epistatic deviations to the average strength of individual additive allelic effects.

C.1.5 Gamma statistic.

This measure is initially introduced in [72] for di-allelic data (i.e., $m_i=2$, e.g., genotypes encoded with "0"s and "1"s as is common in mutation data) and is extended to multi-allelic data (i.e., $m_i \geq 3$, DNA sequences) in [115]. It is defined as the single-step correlation of fitness effects for mutations between neighboring genotypes. It quantifies how the fitness effect of a focal mutation if altered when it occurs in a different genetic background, averaged over all genotypes of the fitness landscape. Geometrically, γ measures the correlation between "slopes" (i.e.,) of the same mutation put into different genetic backgrounds. Thus, if the fitness effect of a mutation is independent of its genetic background (i.e., if there is no epistasis), the correlation in slopes will be perfect ($\gamma=1$), whereas it will be zero if the fitness slopes of each genotype are independent of the fitnesses of other genotypes. Depending on the scale γ can either be used to quantify the strength of gene×gene interactions between specific mutations or as an overall measure for the entire fitness landscape.

Then the matrix of epistatic effects between loci i and j carrying alleles $a_i, b_i \in \mathcal{A}_i$ and $A_j, B_j \in \mathcal{A}_j$ is given by

$$\gamma_{(a_i,b_i)\to(A_j,B_j)} = \text{Cor}\left[s_{(A_j,B_j)}(g), s_{(A_j,B_j)}\left(g_{[(a_i,b_i)]}\right)\right] = \frac{\sum_g s_j(g)s_j(g_{[i]})}{\sum_g (s_j(g))^2}.$$
 (A7)

where $g:=\{x\in\mathcal{G}|x_i=a_i \text{ or } x_i=b_i \text{ and } x_j=A_j \text{ or } x_j=B_j\}\subseteq\mathcal{G} \text{ such that the sum is only calculated over the subset of genotypes carrying one of the two focal alleles at each focal locus. Thus, <math>\gamma_{(a_i,b_i)\to(A_j,B_j)}$ is a quadratic matrix of dimension $(\sum_{i=1}^n \frac{|\mathcal{A}_i|(|\mathcal{A}_i|-1)}{2})$.

Likewise, the epistatic effect of a mutation in locus i with alleles (a_i, b_i) on other loci (and pairs of alleles) can be calculated as

$$\gamma_{(a_i,b_i)\to} = \operatorname{Cor}\left[s(g), s\left(g_{[(a_i,b_i)]}\right)\right] = \frac{\sum_{j\neq i} \sum_{a_j} \sum_{g} s_j(g) s_j(g_{[i]})}{\sum_{j\neq i} \sum_{a_i} \sum_{g} (s_j(g))^2},\tag{A8}$$

where the summation index $\mathfrak{a}_j = \{(A_j, B_j) \mid A_j, B_j \in \mathcal{A}_j \text{ and } A_j \neq B_j\}$ is over the set of subsets of size two that can be constructed from all alleles found at locus j. Note that the third summation index g changes depending on \mathfrak{a}_j .

An additional summation allows calculation of the epistatic effect of a mutation in locus i carrying allele (a_i) on other loci (and pairs of alleles) can be calculated as:

$$\gamma_{a_i \to} = \operatorname{Cor}[s(g), s(g_{[a_i]})] = \frac{\sum_{j \neq i} \sum_{\mathfrak{f}_i} \sum_{\mathfrak{a}_j} \sum_{g} s_j(g) s_j(g_{[i]})}{\sum_{j \neq i} \sum_{\mathfrak{f}_i} \sum_{\mathfrak{a}_j} \sum_{g} (s_j(g))^2}, \tag{A9}$$

where $\mathfrak{f}_i = \{(a_i, b_i) \mid b_i \in \mathcal{A}_i \text{ and } a_i \neq b_i\}$ such that the sum is only calculated over the elements of the set of subsets of size two that can be constructed from all alleles found at locus i that contain allele a_i .

Then, summing over $l_i = \{(a_i, b_i) \mid a_i, b_i \in \mathcal{A}_i \text{ and } a_i \neq b_i\}$, i.e., the elements of the set of subsets of size two that can be constructed from all alleles found at locus i, gives the epistatic effect of a mutation in locus i:

$$\gamma_{i\to} = \operatorname{Cor}[s(g), s(g_{[i]})] = \frac{\sum_{j\neq i} \sum_{\mathfrak{l}_i} \sum_{\mathfrak{a}_j} \sum_{g} s_j(g) s_j(g_{[i]})}{\sum_{j\neq i} \sum_{\mathfrak{l}_i} \sum_{\mathfrak{a}_i} \sum_{g} (s_j(g))^2}.$$
 (A10)

Similarly, the epistatic effect of other mutations (again considering pairs of alleles first) on locus j with alleles (a_i, b_i) can be calculated as

$$\gamma_{\to (A_j, B_j)} = \text{Cor}\left[s_{(A_j, B_j)}(g), s_{(A_j, B_j)}(g_1)\right] = \frac{\sum_{i \neq j} \sum_{\mathfrak{a}_i} \sum_{g} s_j(g) s_j(g_{[i]})}{\sum_{i \neq j} \sum_{\mathfrak{a}_i} \sum_{g} (s_j(g))^2},$$
(A11)

the epistatic effect of other mutations on locus j carrying allele A_i is given by

$$\gamma_{\to A_j} = \operatorname{Cor}\left[s_{(A_j)}(g), s_{(A_j)}(g_1)\right] = \frac{\sum_{i \neq j} \sum_{\mathfrak{f}_j} \sum_{\mathfrak{a}_i} \sum_{g} s_j(g) s_j(g_{[i]})}{\sum_{i \neq j} \sum_{\mathfrak{f}_j} \sum_{\mathfrak{a}_i} \sum_{g} (s_j(g))^2}, \tag{A12}$$

and the epistatic effect of other mutations on locus j becomes

$$\gamma_{\to j} = \operatorname{Cor}[s_j(g), s_j(g_1)] = \frac{\sum_{i \neq j} \sum_{\mathfrak{l}_j} \sum_{\mathfrak{a}_i} \sum_{g} s_j(g) s_j(g_{[i]})}{\sum_{i \neq j} \sum_{\mathfrak{l}_i} \sum_{\mathfrak{a}_i} \sum_{g} (s_j(g))^2},$$
(A13)

Finally, γ_d , that is the decay of correlation of fitness effects with Hamming distance d (i.e., the cumulative epistatic effect of d mutations averaged over the entire fitness landscape) is calculated as

$$\gamma_d = \text{Cor}[s(g), s_j(g_d)] = \frac{\sum_g \sum_{g_d} \sum_{j \neq i_1, i_2, \dots, i_d} \sum_{\mathcal{A}_j \setminus \{A_j\}} s_j(g) s_j(g_{[i_1 i_2 \dots i_d]})}{\sum_g \sum_{\mathcal{A}_i \setminus \{A_i\}} (s_j(g))^2}, \quad (A14)$$

where the last summation is over all different alleles present at locus j except the one carried by genotype g at locus j. We provide implementation of γ_1 in GraphFLA since increasing d would significantly increase the amount of calculations required (e.g., γ_d would require $\binom{n}{d}$ times more calculations compared to γ_1). In doing this, we utilize vector operation from pandas and numpy whenever possible to avoid nested loops as would appear with a brute-force implementation of (A14).

C.2 Navigability

Navigability refers to the ease with which an evolving population can traverse the fitness landscape, typically towards genotypes of higher fitness, under the influence of mutation and natural selection. A highly navigable landscape allows populations to readily find high-fitness peaks, potentially the global optimum, through series of fitness-increasing mutations. Conversely, low navigability implies that evolutionary trajectories might be hindered, often getting trapped on suboptimal peaks due to fitness valleys or complex landscape structures [18, 4, 34].

C.2.1 Global Optima Accessibility

Definition C.9 (Adaptive Walk). An adaptive walk is a sequence of genotypes g_0, g_1, \ldots, g_k such that each genotype g_{t+1} is a neighbor of g_t ($g_{t+1} \in \mathcal{N}(g_t)$) and has strictly higher fitness $(f(g_{t+1}) > f(g_t))$ for all steps $t \in \{0, \ldots, k-1\}$. The walk terminates at step k when g_k is a local optimum (Definition C.8). Under the strong selection weak mutation (SSWM) regime [124], evolution often proceeds along such paths, as natural selection favors higher-fitness genotypes and prevents populations from crossing fitness valleys.

Definition C.10 (Evolutionary Accessibility). A target genotype $g_T \in \mathcal{G}$ is considered accessible from a starting genotype $g_S \in \mathcal{G}$ if there exists at least one adaptive walk (Definition C.9) connecting g_S to g_T . Specifically, a sequence of single mutations $g_S = g_0, g_1, \ldots, g_k = g_T$ exists such that $g_{t+1} \in \mathcal{N}(g_t)$ and $f(g_{t+1}) > f(g_t)$ for all $t \in \{0, \ldots, k-1\}$.

Global optimum accessibility quantifies the extent to which the global optimum (g^*) is accessible (Definition C.10) from other genotypes in the landscape via adaptive walks (Definition C.9). Fitness landscape theory posits that rugged landscapes can hinder adaptation by trapping evolving populations on suboptimal local optima, thereby limiting access to the global optimum [121, 56].

Following [4], we measure global optimum accessibility as the fraction of genotypes residing within the basin of attraction of g^* , denoted $\mathcal{B}(g^*)$ (Definition C.11). This fraction represents the probability that an adaptive walk initiated from a random genotype will eventually reach g^* :

$$\alpha_{go} = \frac{|\mathcal{B}(g^*)|}{|\mathcal{G}|} = \frac{|\mathcal{B}(g^*)|}{\prod_{i=1}^n m_i}.$$
(A15)

An accessibility value $\alpha_{go}\approx 1$ suggests a highly navigable landscape where the global optimum is readily reachable via simple hill-climbing dynamics from most starting points. Conversely, a low α_{go} indicates that reaching the global optimum through adaptive walks alone is improbable for populations starting from random initial genotypes, suggesting they are likely to become trapped on local optima.

It is noteworthy that recent findings suggest some rugged landscapes can still be highly navigable, with the global optimum accessible from a large fraction of genotypes [4]. Furthermore, even if g^* is inaccessible via adaptive walks from certain regions, this does not necessarily prevent its discovery through methods used in directed evolution. Many computational optimizers (e.g., simulated annealing [125], machine learning-guided directed evolution) employ mechanisms to traverse fitness valleys and escape local optima. Nevertheless, highly rugged landscape topographies generally pose greater challenges for locating global fitness peaks [18, 34].

C.2.2 Basin of Attraction and BFC

Definition C.11 (Basin of Attraction). The basin of attraction $\mathcal{B}(g^{\ell})$ of a local optimum g^{ℓ} is the set of all genotypes $g \in \mathcal{G}$ from which at least one adaptive walk starting at g can reach g^{ℓ} :

$$\mathcal{B}(g^{\ell}) = \{g \in \mathcal{G} \mid \exists \text{ an adaptive walk } g_0 = g, \dots, g_k = g^{\ell}\}.$$

The size of the basin, $|\mathcal{B}(g^{\ell})|$, reflects the accessibility of the local optimum g^{ℓ} within the genotype space. Larger basins are often associated with higher-fitness local optima [4]. We use the basin size-fitness correlation to quantify this relationship.

GraphFLA estimates basin sizes by analyzing adaptive walks. It supports two distinct methods, yielding different definitions and computational properties for basin size:

• Stochastic adaptive walks: Also known as first-improvement hill climbing [126]. At each step, one neighbor g' ∈ N(g) with f(g') > f(g) is chosen uniformly at random from all such improving neighbors. Because of this stochasticity, walks from the same starting genotype can terminate at different local optima, leading to overlapping basins [4]. GraphFLA calculates the basin size deterministically by identifying the set of all genotypes from which at least one such adaptive walk can reach the local optimum g^ℓ. In the graph representation, this corresponds to finding all ancestors of the node g^ℓ reachable via directed paths representing fitness increases, typically using functions like those available in igraph.

This computation can be expensive for large landscapes (e.g., > 300,000 genotypes) with numerous local optima.

• Greedy adaptive walks: Also known as best-improvement hill climbing. At each step, this walk deterministically selects a neighbor $g' \in \mathcal{N}(g)$ that maximizes the fitness increase, $\Delta f = f(g') - f(g)$. If multiple neighbors offer the same maximal increase, a consistent tie-breaking rule (e.g., random choice implemented once or lexicographical order) ensures determinism. The path from any starting genotype g is unique, meaning each genotype belongs to the basin of exactly one local optimum. Consequently, these basins partition the genotype space \mathcal{G} , and their sizes sum to $|\mathcal{G}| = \prod_{i=1}^n m_i$. GraphFLA calculates these basin sizes by simulating a greedy walk starting from every genotype $g \in \mathcal{G}$ and recording the local optimum reached.

Using these two measures of basin size, GraphFLA provides two features, BFC_{acc} and BFC_{greedy} that assess whether local optima with higher fitness tend to have larger basin of attraction:

$$BFC_{acc} = Cor \left[f(g^{\ell}), |\mathcal{B}_{acc}(g^{\ell})| \right]$$
(A16)

$$BFC_{greedy} = Cor\left[f(g^{\ell}), |\mathcal{B}_{greedy}(g^{\ell})|\right]$$
(A17)

A higher value of BFC indicates that fitter local optima would have larger basin of attraction compared to those have lower fitness, which results in their higher evolutionary accessibility and increased navigability of the whole landscape [4].

C.2.3 Fitness Distance Correlation (FDC)

Fitness Distance Correlation (FDC) is a measure used to assess the global structure of a fitness landscape and its potential navigability by an evolutionary process [76]. Specifically, it quantifies the relationship between the fitness of genotypes and their distance to a known global optimum g^* . In biological fitness landscapes, this distance is typically the Hamming distance $d_H(g,g^*)$ (Definition C.3) between a genotype $g \in \mathcal{G}$ and the global optimum $g^* \in \mathcal{G}$ (Definition C.8).

The FDC is calculated as the Pearson correlation coefficient between the fitness values f(g) of all genotypes in the landscape (or a representative sample) and their respective Hamming distances to the global optimum g^* :

$$FDC = Cor [f(g), d_H(g, g^*)], \qquad (A18)$$

The interpretation of the FDC value provides insights into the navigability of the fitness landscape:

- FDC ≈ -1: A strong negative correlation indicates that genotypes with higher fitness tend
 to be closer (i.e., have a smaller Hamming distance) to the global optimum g*. This signifies
 a relatively smooth, "funnel-like" landscape structure where fitness gradients consistently
 guide an evolutionary search towards g*. Such landscapes are considered highly navigable
 by processes like adaptive walks (Definition C.9), as selection for increased fitness generally
 directs the population towards the global peak.
- **FDC** ≈ 0: A correlation close to zero suggests that there is no clear relationship between a genotype's fitness and its distance to the global optimum. This is characteristic of rugged or random landscapes, where fitness values can change erratically and provide little information about the direction towards g^* . In such landscapes, navigability is low, and evolutionary processes are more likely to become trapped on local optima (Definition C.8) far from g^* .
- FDC ≈ +1: A strong positive correlation implies that genotypes with higher fitness tend to
 be further away from the global optimum g*. This indicates a "deceptive" landscape, where
 selection for immediate fitness gains would systematically lead an evolving population away
 from the global optimum. Such landscapes are exceptionally difficult to navigate towards g*
 using simple hill-climbing strategies.

C.2.4 Evolvability-Enhancing Mutations

Evolvability [127] refers to the capacity of a biological system to generate adaptive heritable variation. Unlike measures focusing solely on the direct fitness impact of a mutation (first-order selection), evolvability emphasizes the potential for future adaptive change (second-order selection) [127]. On top of this, Wagner introduced the concept of an evolvability-enhancing (EE) mutation, defined as one that modifies the genetic background such that subsequent mutations at other loci tend to be, on average, more beneficial or less deleterious, irrespective of the initial mutation's own fitness effect.

Definition C.12 (Evolvability-Enhancing (EE) Mutation). Consider a mutation at locus j that converts genotype g to $g_{[j]}$. Let $\mathcal{N}_{-j}(g)$ denote the set of single-mutant neighbors of g resulting from mutations at any locus $k \neq j$. The size of this set is $|\mathcal{N}_{-j}(g)| = \sum_{k \neq j, k=1}^{n} (m_k - 1)$. Let $\langle f \rangle_{\mathcal{N}_{-j}(g)}$ be the average fitness over the genotypes in $\mathcal{N}_{-j}(g)$. Similarly, let $\mathcal{N}_{-j}(g_{[j]})$ be the set of single-mutant neighbors of $g_{[j]}$ resulting from mutations at loci $k \neq j$, and let $\langle f \rangle_{\mathcal{N}_{-j}(g_{[j]})}$ be their average fitness.

The mutation $g \rightarrow g_{[j]}$ *is defined as evolvability-enhancing (EE) if:*

• It is σ -neutral ($|s_j(g)| < \sigma$, see Def. C.14) and increases the average fitness of subsequent mutants:

$$\langle f \rangle_{\mathcal{N}_{-i}(q_{[i]})} - \langle f \rangle_{\mathcal{N}_{-i}(q)} > 0.$$
 (A19)

• It is beneficial $(s_j(g) > 0)$ and enhances the fitness prospects of subsequent mutations beyond its own additive contribution:

$$\langle f \rangle_{\mathcal{N}_{-j}(g_{[j]})} - \langle f \rangle_{\mathcal{N}_{-j}(g)} > s_j(g). \tag{A20}$$

This condition is equivalent to requiring that the average fitness effect of subsequent mutations (relative to the background they arise in) is greater in the $g_{[j]}$ background than in the $g_{[j]}$ background:

$$\left(\langle f \rangle_{\mathcal{N}_{-j}(g_{[j]})} - f(g_{[j]})\right) > \left(\langle f \rangle_{\mathcal{N}_{-j}(g)} - f(g)\right). \tag{A21}$$

This definition implies that an EE mutation at locus j exhibits, on average, positive epistasis with mutations occurring at other loci $k \neq j$ [73]. Following [73], we primarily consider beneficial EE mutations. Such mutations can spread through populations via direct (first-order) selection due to their immediate fitness advantage, potentially increasing future evolvability as a byproduct without needing selection to act directly on evolvability itself (second-order selection). Beneficial EE mutations are expected to shift the distribution of fitness effects (DFE) of subsequent mutations favourably, for instance, by reducing the impact of deleterious mutations or increasing the frequency and/or magnitude of beneficial ones.

C.2.5 Mean Accessible Path Length

The minimum number of single mutations required to transition between a genotype g and the global optimum g^* is their Hamming distance, $d_H(g,g^*)$ (Definition C.3). However, not all paths realizing this minimum distance are necessarily evolutionarily accessible; that is, they may not consist solely of fitness-increasing steps (Section C.2.1). Consequently, the shortest accessible path, composed entirely of fitness-increasing mutations (an adaptive walk, Definition C.9), can be longer than the Hamming distance, potentially requiring detours to navigate around fitness valleys [59, 128].

We measure the typical length of such paths using the mean shortest accessible path length to the global optimum, averaged over all genotypes from which g^* is reachable.

Definition C.13 (Shortest Accessible Path Length). For a genotype g within the basin of attraction of the global optimum g^* (i.e., $g \in \mathcal{B}(g^*)$), the shortest accessible path length, $d_{acc}(g,g^*)$, is the minimum number of steps k in an adaptive walk $g_0 = g, \ldots, g_k = g^*$ terminating at g^* . If g is not in the basin of g^* ($g \notin \mathcal{B}(g^*)$), then by definition $d_{acc}(g,g^*) = \infty$.

The mean accessible path length to the global optimum, $\langle d_{\rm acc} \rangle_{q^*}$, is calculated as:

$$\langle d_{\mathrm{acc}} \rangle_{g^*} = \frac{1}{|\mathcal{B}(g^*)|} \sum_{g \in \mathcal{B}(g^*)} d_{\mathrm{acc}}(g, g^*).$$

The average is taken over all genotypes g belonging to the basin of attraction $\mathcal{B}(g^*)$ of the global optimum (Definition C.11).

In GraphFLA, $d_{\rm acc}(g,g^*)$ is computed for all $g\in\mathcal{B}(g^*)$ using shortest path algorithms on the subgraph containing only fitness-increasing transitions, implemented via igraph's distances targeting g^* . While the absolute value of $\langle d_{\rm acc} \rangle_{g^*}$ is context-dependent (influenced by landscape size and dimensionality), comparing it to the mean Hamming distance between genotypes in the basin and the optimum, $\langle d_H(g,g^*) \rangle_{g\in\mathcal{B}(g^*)}$, can provide valuable insights into landscape navigability. In a perfectly smooth landscape with a single peak, $d_{\rm acc}(g,g^*)=d_H(g,g^*)$ for all g. In rugged landscapes, accessible paths often meander, leading to $\langle d_{\rm acc} \rangle_{g^*} > \langle d_H(g,g^*) \rangle_{g\in\mathcal{B}(g^*)}$ [4, 36]. A larger difference signifies greater path indirectness imposed by the landscape's rugged structure.

C.3 Epistasis

C.3.1 Classification of Epistasis

This section defines different types of pairwise epistatic interactions between mutations at two distinct loci, say i and j. Epistasis occurs when the fitness effect of a mutation at one locus depends on the allele present at the other locus. We classify epistasis based on how the fitness effects change across genetic backgrounds. Consider a reference genotype g, the single mutants $g_{[ij]}$ and $g_{[j]}$, and the double mutant $g_{[ij]}$ (assuming specific mutations $a_i \to a_i'$ at locus i and $a_j \to a_j'$ at locus j are implied or defined). The interaction epistasis term ϵ_{ij} measures the deviation from additivity:

$$\epsilon_{ij} = f(g_{[ij]}) - f(g) - [f(g_{[i]}) - f(g)] - [f(g_{[j]}) - f(g)]$$
(A22)

$$= f(g_{[ij]}) - f(g_{[i]}) - f(g_{[j]}) + f(g)$$
(A23)

Using the selection coefficient notation from Definition C.7, where $s_i(g) = f(g_{[i]}) - f(g)$ is the effect of the mutation at locus i in the background g, and $s_i(g_{[j]}) = f(g_{[ij]}) - f(g_{[j]})$ is the effect of the same mutation at locus i but in the background $g_{[j]}$, the epistasis term can be equivalently written as:

$$\epsilon_{ij} = s_i(g_{[j]}) - s_i(g) = s_j(g_{[i]}) - s_j(g)$$

Based on the sign and magnitude of the selection coefficients involved, we can classify the interaction:

- No epistasis ($\epsilon_{ij} = 0$): The effects of the mutations are additive. The effect of mutation i is the same regardless of the allele at locus j, i.e., $s_i(g_{[j]}) = s_i(g)$.
- Magnitude epistasis ($\epsilon_{ij} \neq 0$, no sign changes): The fitness effects are non-additive ($\epsilon_{ij} \neq 0$), but the sign of each mutation's effect remains consistent across the backgrounds considered. That is, $s_i(g)$ and $s_i(g_{[j]})$ have the same sign (or zero), and $s_j(g)$ and $s_j(g_{[i]})$ also have the same sign (or zero). This occurs when the combined effect deviates from the sum of individual effects.
 - **Positive epistasis** ($\epsilon_{ij} > 0$): The combined effect is greater than expected from additivity $(f(g_{[ij]}) f(g) > s_i(g) + s_j(g))$. This includes synergistic interactions where, for example, two beneficial mutations together yield a larger benefit than their sum, or two deleterious mutations are less harmful together than expected (antagonistic interaction between deleterious mutations).
 - Negative epistasis ($\epsilon_{ij} < 0$): The combined effect is less than expected from additivity $(f(g_{[ij]}) f(g) < s_i(g) + s_j(g))$. This includes antagonistic interactions like diminishing returns, where two beneficial mutations yield a smaller benefit together than their sum [38] (see Section C.3.2), or synergistic interactions where two deleterious mutations are more harmful together than expected. Negative epistasis can decelerate adaptation [41, 38, 129], create concave fitness peaks [17], and increase mutational robustness near peaks [17, 11].
- Sign epistasis ($\epsilon_{ij} \neq 0$, one sign change): The sign of the fitness effect of one mutation (e.g., beneficial vs. deleterious) flips depending on the background provided by the other mutation, while the second mutation's sign remains consistent. For instance, mutation i might be

beneficial in background $g(s_i(g) > 0)$ but deleterious in background $g_{[j]}(s_i(g_{[j]}) < 0)$, while mutation j's sign remains the same $(s_j(g))$ and $s_j(g_{[i]})$ have the same sign). Sign epistasis restricts accessible mutational trajectories [5, 36, 18] and contributes to landscape ruggedness [37, 130].

• Reciprocal sign epistasis ($\epsilon_{ij} \neq 0$, two sign changes): A symmetric form where the sign of the effect of both mutations changes depending on the background provided by the other. For example, both single mutations might be deleterious ($s_i(g) < 0, s_j(g) < 0$), but each becomes beneficial in the background containing the other mutation ($s_i(g_{[j]}) > 0, s_j(g_{[i]}) > 0$), often leading to a beneficial double mutant ($f(g_{[ij]}) > f(g)$).

Formally, the type of epistatic interaction $\mathfrak{e}(g,i,j)$ between specific mutations at loci i and j relative to a reference genotype g can be classified based on the selection coefficients:

$$\mathfrak{e}(g,i,j) = \begin{cases} \text{None} & \text{if } \epsilon_{ij} = 0 \\ \text{Magnitude} & \text{if } \epsilon_{ij} \neq 0 \text{ and } [s_i(g) \cdot s_i(g_{[j]}) \geq 0 \text{ and } s_j(g) \cdot s_j(g_{[i]}) \geq 0] \\ \text{Reciprocal Sign} & \text{if } s_i(g) \cdot s_i(g_{[j]}) < 0 \text{ and } s_j(g) \cdot s_j(g_{[i]}) < 0 \\ \text{Sign} & \text{otherwise (i.e., if } \epsilon_{ij} \neq 0 \text{ and exactly one sign product is negative)} \end{cases}$$

where the condition $\epsilon_{ij} = s_i(g_{[j]}) - s_i(g) = 0$ defines the non-epistatic case. The product conditions check for sign changes (a negative product indicates a sign change, assuming neither term is zero).

The prevalence of each epistasis type across the entire landscape can be estimated by enumerating all pairs of single mutations originating from all possible reference genotypes g. Computationally, this involves analyzing local structures corresponding to double mutants relative to a reference genotype. For graph-based representations, these structures correspond to specific 4-node motifs. As noted by [4], specific non-isomorphic directed motifs identifiable using graph libraries like igraph correspond to these epistasis types (e.g., motifs 66, 52, and 19 were identified as potentially representing magnitude, sign, and reciprocal sign epistasis, respectively).

C.3.2 Global epistasis.

Global epistasis refers to systematic trends where the fitness effect of a mutation exhibits a predictable relationship with the overall fitness of the genetic background it occurs in [39, 129, 41]. Global epistasis often manifests in two particular forms:

- Diminishing returns epistasis: This pattern describes scenarios where the fitness benefit (f(g') f(g) > 0) conferred by a beneficial mutation decreases as the fitness of the genetic background, f(g), increases. In other words, the positive impact of a beneficial mutation diminishes in already fit genotypes [38]. To quantify this, we identify all beneficial single-step mutations (where the selection coefficient f(g') f(g) is positive) across the landscape. Diminishing returns is then measured by calculating the Pearson correlation coefficient between the fitness of the background genotype, f(g), and the corresponding positive selection coefficient, s(g → g'), across all such beneficial mutations. A negative correlation value indicates the presence of diminishing returns epistasis.
- Increasing costs epistasis: This describes a pattern where the fitness cost (negative effect) of a deleterious mutation (f(g')-f(g)<0) becomes larger (more negative) as the fitness of the genetic background, f(g), increases. This implies that fitter genotypes are less tolerant to deleterious mutations [75]. To quantify this, we identify all deleterious single-step mutations (where the selection coefficient $s(g \to g')$ is negative). Increasing costs epistasis is measured by calculating the Pearson correlation coefficient between the fitness of the background genotype, f(g), and the magnitude (absolute value) of the corresponding negative selection coefficient, $|s(g \to g')|$, across all such deleterious mutations. A positive correlation value indicates the presence of increasing costs epistasis, meaning the fitness cost tends to be larger in higher-fitness backgrounds.

These global epistatic trends suggest a general "coupling" of mutations through overall fitness, potentially leading to predictable macro-evolutionary dynamics like decelerating rates of adapta-

tion [41, 129]. This contrasts with idiosyncratic epistasis (see the next section), where interactions depend more specifically on the identities and combination of the mutations involved [39].

C.3.3 Idiosyncratic Epistasis

Idiosyncratic epistasis describes genetic interactions where the fitness effect of a mutation depends strongly and often unpredictably on the specific genetic background [131, 39, 132]. The term "idiosyncratic" highlights that these interactions are specific to the identities of the involved loci and alleles, resulting in context-dependent effects that can vary significantly even across similar genetic backgrounds. This contrasts with global epistasis models in the previous section (e.g., diminishing returns, increasing costs), where a mutation's effect is predicted to vary systematically based mainly on the background genotype's fitness.

To quantify the extent of idiosyncratic epistasis in a landscape, we measure the variability of individual mutation effects across different genetic backgrounds. Following Lyons et al., an idiosyncrasy index can be calculated for each specific mutational transition.

Consider a specific mutation at locus i changing allele $a_i \in \mathcal{A}_i$ to allele $b_i \in \mathcal{A}_i$ ($a_i \neq b_i$). Let $\mathcal{G}_{i,a_i} = \{g \in \mathcal{G} \mid \text{allele at locus } i \text{ in } g \text{ is } a_i\}$ denote the set of all genotypes (backgrounds) carrying allele a_i at locus i. The selection coefficient for this specific mutation $a_i \to b_i$ occurring in a background $g \in \mathcal{G}_{i,a_i}$ is defined according to Definition C.7:

$$s_{i,a_i \to b_i}(g) = f(g_{[i \leftarrow b_i]}) - f(g), \tag{A25}$$

where $g_{[i \leftarrow b_i]}$ is the genotype identical to g but with allele b_i at locus i.

The variability of this specific mutation's effect across all possible backgrounds is captured by its variance:

$$V_{i,a_{i}\to b_{i}} = \operatorname{Var}_{g\in\mathcal{G}_{i,a_{i}}}\left[s_{i,a_{i}\to b_{i}}(g)\right] = \frac{1}{|\mathcal{G}_{i,a_{i}}|} \sum_{g\in\mathcal{G}_{i,a_{i}}} \left(s_{i,a_{i}\to b_{i}}(g) - \bar{s}_{i,a_{i}\to b_{i}}\right)^{2}, \tag{A26}$$

where $\bar{s}_{i,a_i \to b_i}$ is the mean selection coefficient of the mutation $a_i \to b_i$ averaged over all backgrounds $g \in \mathcal{G}_{i,a_i}$.

To normalize this measure, the variability is compared to the overall variability of selection coefficients across the entire landscape. Let \mathcal{S} represent the set of all possible single-mutation selection coefficients:

$$S = \{ s_{k,C_k \to D_k}(h) \mid k \in \{1, \dots, n\}, C_k, D_k \in \mathcal{A}_k, C_k \neq D_k, h \in \mathcal{G}_{k,C_k} \}.$$
 (A27)

The total variance of selection coefficients across the landscape is:

$$V_s = \operatorname{Var}[s \in \mathcal{S}] = \frac{1}{|\mathcal{S}|} \sum_{s \in \mathcal{S}} (s - \bar{s})^2, \tag{A28}$$

where \bar{s} is the global mean selection coefficient averaged over all single mutations in all backgrounds.

The idiosyncrasy index for the specific mutation $a_i \to b_i$ is the ratio of the standard deviation of its effect across backgrounds to the standard deviation of all selection coefficients in the landscape:

$$I_{\rm id}(i, a_i \to b_i) = \frac{\sqrt{V_{i, a_i \to b_i}}}{\sqrt{V_c}}.$$
 (A29)

An index value $I_{\rm id}(i,a_i \to b_i) \approx 1$ signifies high idiosyncrasy, implying that the effect of this mutation is highly context-dependent, varying across backgrounds almost as much as selection coefficients vary globally. Conversely, $I_{\rm id}(i,a_i \to b_i) \approx 0$ indicates low idiosyncrasy, suggesting the mutation has a relatively consistent effect regardless of the genetic background.

To derive a single measure representing the overall level of idiosyncrasy for the entire landscape, we average the index across all possible single mutations. Let \mathcal{M} be the set of all possible directed single mutations, $\mathcal{M} = \{(i, a_i \to b_i) \mid i \in \{1, \dots, n\}, a_i, b_i \in \mathcal{A}_i, a_i \neq b_i\}$. The total number of such mutations is $|\mathcal{M}| = \sum_{k=1}^n m_k(m_k - 1)$. The average idiosyncrasy index for the landscape is:

$$I_{\mathrm{id}} = \frac{1}{|\mathcal{M}|} \sum_{(i, a_i \to b_i) \in \mathcal{M}} I_{\mathrm{id}}(i, a_i \to b_i). \tag{A30}$$

A high average idiosyncrasy I_{id} suggests that, overall, predicting a mutation's fitness effect requires detailed knowledge of the specific genetic background, and highlights the prevalence of complex, context-specific interactions within the landscape.

C.3.4 Pairwise and Higher-order Epistasis

Epistatic interactions can occur between pairs of mutations (pairwise epistasis) or among multiple ones (high-order epistasis). Ideally, to exactly determine the fraction of each pair of epistasis would require decompising the landscape into products of the single-locus variables according to the following expansion [133, 134]:

$$f(g) = a^{(0)} + \sum_{i} a_i^{(1)} a_i + \sum_{ij} a_{ij}^{(2)} a_i a_j + \sum_{ijk} a_{ijk}^{(3)} a_i a_j a_k + \dots + a_{12\dots n}^{(n)} a_1 a_2 \cdots a_n$$
 (A31)

There are $\binom{n}{k}$ coefficients of type $a^{(k)}$ in this expansion, one for each subset of k of n loci. According to the binomial theorem, the total number of coefficients equals 2^n , which makes it evident that the mapping between fitness values and expansion coefficients is one-to-one. The first-order coefficient $a^{(1)}$ describes the linear, non-epistatic effects, the second-order coefficient $a^{(2)}$ denotes pairwise epistatic interactions and so on.

However, such expansion is often computationally prohibitive because of the exponential growth in epistasis terms. As an alternative, researchers often specifically distinguish between pairwise and higher-order epistasis because the latter describes complex dependencies that are not reducible to combinations of pairwise interactions and can have profound consequences for the fitness land-scape [134]. For example, higher-order epistasis can cause the effects of mutations, and even the nature of pairwise interactions, to change depending on the broader genetic background, sometimes leading to mutations switching between being beneficial and detrimental—outcomes that cannot be predicted by considering only pairwise effects [42].

To measure the prevalence of higher-order epistasis in the landscape, GraphFLA provides a measure, $\epsilon_{(2)}$, which assesses how much variance in fitness distributions can be explained by pairwise epistasis alone. This is performed by fitting a polynomial linear regression model with interaction terms up to the second order. $\epsilon_{(2)}$ is then derived as the R^2 score of this model in fitting the data.

C.4 Neutrality

C.4.1 Neutrality

Mutational robustness [43, 44, 77] measures the extent to which a genotype's fitness remains unchanged by mutations, reflecting its ability to buffer genetic perturbations. Related is the concept of *neutral mutations*, which cause little to no change in fitness. Neutral mutations allow populations to explore the genotype space without incurring significant fitness costs. Sets of genotypes connected by neutral mutations and sharing approximately the same fitness level form *neutral networks* [17, 16, 43, 13].

Definition C.14 (Neutral Mutation and Neighbors). A mutation converting genotype g into a neighbor $g' \in \mathcal{N}(g)$ is considered σ -neutral if the absolute fitness change is below a predefined tolerance $\sigma \geq 0$: $|f(g') - f(g)| < \sigma$. The set of σ -neutral neighbors of g is:

$$\mathcal{N}_{\sigma}(g) = \{ g' \in \mathcal{N}(g) \mid |f(g') - f(g)| < \sigma \}.$$

Empirically, σ is often set based on the variance in the measured fitness across replications and act as a noise threshold. With the above definition, we can now define the mutational robustness for a specific genotype:

Definition C.15 (Mutational Robustness). The mutational robustness R(g) of a genotype g is the fraction of its neighbors that are σ -neutral [77, 127]:

$$R(g) = \frac{|\mathcal{N}_{\sigma}(g)|}{|\mathcal{N}(g)|}.$$

To characterize the neutrality of the entire fitness landscape, we average the mutational robustness across all genotypes:

$$\eta = \frac{1}{|\mathcal{G}|} \sum_{g \in \mathcal{G}} R(g). \tag{A32}$$

This quantity, referred to as *landscape neutrality*, measures the overall prevalence of neutrality. A high landscape neutrality ($\langle R \rangle_{\mathcal{G}}$) indicates the presence of extensive neutral networks [17, 16, 43, 13]. These networks can facilitate exploration of the genotype space via neutral drift without much fitness costs, which could potentially enhance *evolvability* [127], as discussed in the following section (C.2.4).

D Landscape Models

In the following, we briefly introduce the various fitness landscape models implemented in GraphFLA. For an excellent general overview, we refer the reader to a review by Szendro et al..

The additive model. In the additive model, the fitness of each genotype is given by the sum/product over the individual per locus fitness effects. Thus, the fitness effect of a specific allele, drawn from a Normal distribution with mean μ_a and variance σ_a^2 [72] (see also [135]), is independent of its genetic background (i.e., it is constant across all genetic backgrounds), such that all mutations are non-interacting (i.e., there is no epistasis) and the resulting unimodal fitness landscape is (maximally) smooth. In particular, the roughness-to-slope ratio is 0 and $\mathbb{E}[\gamma_d] = 1$ for the entire range of mutational distances d. Note that when fitnesses are given by the product over the individual fitness effects, this model is also referred to as the multiplicative model.

The House-of-cards model. On the other extreme, in the House-of-cards (HoC) model [136] the fitness of each genotype is an i.i.d. normally distributed random variable with zero mean and variance σ_{HoC}^2 resulting in an uncorrelated, maximally rugged fitness landscape that is characterized by multiple local optima [56, 80]. In particular, the fitness effect of an allele entirely depends on its genetic background such that there is complete interaction between all loci (i.e., full epistasis) which is also reflected in the roughness-to-slope ratio and $\mathbb{E}[\gamma_d]$ that become infinity and zero (for d>0), respectively.

The Rough Mount Fuji model. Introduced by [137], the Rough-Mount-Fuji (RMF) model, named after the eponymous mountain in Japan, which was initially formulated in the context of protein evolution [see also [135], for a simplified version], interpolates between the former two extremes. The fitness of a genotype is composed by an additive component (parametrized by μ_a and σ_a^2 ; see above) and a HoC component (parametrized by $\sigma_{\rm HoC}^2$) such that the extent of epistatic interactions ranges between none (additive model) to complete (HoC model) depending on the relative sizes of these three parameters. In particular, when $\sigma_{\rm HoC}^2 \ll \mu_a^2 + \sigma_a^2$ the RMF model becomes an additive model whereas for $\sigma_{\rm HoC}^2 \gg \mu_a^2, \sigma_a^2$ it essentially behaves like a HoC model [72]. Accordingly, $0 \leq \mathbb{E}[\gamma_d] = {\rm const} \leq 1$ for d>0 and the roughness-to-slope ratio ranges from zero to infinity.

The Kauffman NK model. Another frequently used fitness landscape model that, as the RMF model, also interpolates between the additive and the HoC model [56, 80] is the Kauffman NK model, where N di-allelic loci interact with $K \in \{0,1,\ldots,L-1\}$ randomly assigned other loci. In particular, for K=0 the NK model collapses to an additive model whereas for K=L-1 it approaches the HoC model. Although there are different ways how groups of interacting loci can be chosen [138], properties such as the mean number and height of local optima tend only to be weakly dependent on

the exact choice being made. For the NK model, $\mathbb{E}[\gamma_d]$ is a non-negative monotonically decreasing function in d, and the roughness-to-slope ratio can again range from zero to infinity.

The eggbox model. Introduced by [72], the eggbox model is a maximally epistatic, anticorrelated fitness landscape model (i.e., all loci interact with each other up to interactions of order L), in which the fitness effect of an allele switches from the highest to lowest value (or vice versa) between genetic backgrounds one step apart. Accordingly, depending on whether two genotypes are separated by an odd or even Hamming distance, their absolute fitness difference is either twice the mean allelic fitness effect or zero. Thus, this model generates an extreme case of reciprocal sign epistasis in which each mutation is either deleterious or compensatory, multiple local optima exist, and γ_d accordingly oscillates between -1 and 1.

E Analysis for Phenotype Landscapes

E.1 Phenotype Landscape Models

To demonstrate the applicability of GraphFLA to analyzing phenotype landscapes, we consider several well-known systems, including \blacktriangleright the RNA secondary structure phenotype landscape for lengths n=12 and n=15 (RNA12, RNA15) representing the RNA sequence's minimum free energy folded secondary structure [139, 97, 140], \blacktriangleright the Polyomino lattice self-assembly maps ($S_{2,8}$ and $S_{3,8}$) modelling the topology of protein quaternary structure assembled from interacting constituent tiles [141, 100, 142], and \blacktriangleright several hydrophobic-polar (HP) lattice protein models for folding of a sequence into a tertiary structure (two compact models, HP_{5x5} and HP_{3x3x3}, and two non-compact ones, HP₂₀ and HP₂₅) [98, 143, 144]. These phenotype landscapes have been thoroughly studied and compared in [141, 13]

RNA secondary structure: The search space \mathcal{G} is made of RNA sequences g where each position can take 4 RNA nucleotide bases ($\mathcal{A}_i = \{A, C, G, U\}$). Phenotypes \mathcal{P} are the secondary structure bonding pattern of the minimum free energy fold of the genotype, represented with the dot-bracket notation [97]. We use the Vienna package [97] with default parameters to convert RNA sequences $g \in \mathcal{G}$ to dot-bracket secondary structures $p \in \mathcal{P}$. Phenotype landscapes is the mapping from the sequence space \mathcal{G} to their phenotypes \mathcal{P} , and are represented as RNA-n with sequences of length n. As illustration, we consider n = 12, 15, resulting in the RNA12 and RNA15 phenotype landscapes.

HP lattice model: In this model, genotypes \mathcal{G} comprise sequences of hydrophobic (H) or polar (P) amino acids (alphabet $\mathcal{A}_i = \{H, P\}$) [98, 99]. Phenotypes \mathcal{P} correspond to the unique minimum energy conformation of a genotype when folded onto a 2D (square) or 3D (cubic) lattice. Folds are represented as strings of directional moves (2D: "Up", "Down", "Left", "Right"; 3D additionally "Forward", "Back"). Following [143, 144], only non-adjacent H-H pairs contribute to energy ($E_{HH} = -1$), while $E_{HP} = E_{PP} = 0$. Sequences lacking a unique minimum energy structure are considered undefined. We investigate both non-compact (HP_L) and compact phenotype landscapes. In HP_L, the phenotype is the minimum energy fold among all possible folds of a specific length. In compact maps (e.g., 2D HP_{lxw} like HP_{5x5}; 3D HP_{lxwxh} like HP_{3x3x3}), folds are confined to a prescribed grid. These compact models aim to better emulate the globular nature of native proteins [145], significantly reducing the conformational space while enhancing fidelity to observed protein topologies. We analyzed compact (HP_{3x3x3} and HP_{5x5}) and non-compact (HP₂₀ and HP₂₅) landscapes for illustration.

Polyomino model: This model represents protein quaternary structure on a 2D square lattice using an assembly kit of tiles. Genotypes $g \in \mathcal{G}$ define this kit of n_t tiles, where each tile edge has one of n_c colors (interface types) denoted by integers. We follow [141, 100], focusing on phenotype landscapes S_{n_t,n_c} , specifically $S_{2,8}$. We use $n_c = 8$ colors; tile edges are assigned bases from the alphabet $A_i = \{0,1,2,3,4,6,7\}$. Interactions are restricted to $1 \leftrightarrow 2$, $3 \leftrightarrow 4$, and $5 \leftrightarrow 6$, while colors 0 and 7 are neutral. The genotype sequence, consisting of bases from A, is encoded clockwise onto the four edges of each tile in the kit. Phenotype construction begins by "seeding" the lattice with the first tile. Subsequent tiles from the kit are stochastically placed at complementary interaction sites on the lattice. Assembly halts if no further placements are possible or if the structure grows unboundedly. This assembly process is repeated k = 200 times. The phenotype is the unique, rotationally invariant, bounded polyomino shape observed across the ensemble of assemblies.

E.2 Phenotype Landscape Features

Following [141], we consider the following 3 landscape features that are dedicated to characterizing phenotype landscape topography. The analysis results for the previously described landscapes are summarized in Table A1 below.

Table A1: Features of different phenotype landscapes analyzed

			1	7 1	1		
Phenotype landscape	$ \mathcal{A} $	n	$ \mathcal{G} $	$ \mathcal{P} $	$\phi_{ m del}$	$\log_{10} R$	η_p
RNA12	4	12	4^{12}	58	0.854	4.6	0.465
RNA15	4	15	4^{15}	432	0.650	5.9	0.482
$S_{2,8}$	8	8	8^{8}	14	0.537	5.8	0.487
HP5x5	2	25	2^{25}	550	0.816	4.1	0.285
HP3x3x3	2	27	2^{27}	49,808	0.939	2.2	0.115
HP20	2	20	2^{20}	5,311	0.976	0.7	0.102
HP25	2	25	2^{25}	107,337	0.977	0.9	0.099

Redundancy. Denoted by R, it is defined as the average number of distinct genotypes $g \in \mathcal{G}$ that map to each non-deleterious phenotype $p \in \mathcal{P}$. Redundancy is intrinsically linked to the average size of phenotypically neutral networks, which consist of sets of genotypes that share the same phenotype and are often connected by single mutations.

Deleterious frequency. Denoted as ϕ_{del} , this metric represents the fraction of the entire genotype space \mathcal{G} that is occupied by genotypes failing to map to a well-defined, functional phenotype. The nature of a deleterious phenotype is model-specific:

- In RNA secondary structure landscapes, such as RNA12 and RNA15, a deleterious phenotype corresponds to an unfolded RNA sequence that lacks any defined secondary structure.
- For Hydrophobic-Polar (HP) lattice protein models, like HP_{5x5} (a compact 2D model) or HP₂₀ (a non-compact model), a deleterious outcome signifies an amino acid sequence that does not fold into a unique minimum energy conformation.
- In the context of Polyomino lattice self-assembly models, for example $S_{2,8}$ or $S_{3,8}$ which model protein quaternary structure, a deleterious genotype is one that results in an unbounded or non-deterministic assembly process.

Phenotypic neutrality. Denoted as η_p , it is the average proportion of mutational neighbors of a genotype g (i.e., genotypes $g' \in \mathcal{N}(g)$) that exhibit the same phenotype as g. This average is computed over all genotypes in G that correspond to non-deleterious phenotypes. The value of η_p provides a measure of local neutral connectivity within the phenotypic landscape, indicating the extent to which mutations can occur without altering the observable phenotype. This concept of phenotypic neutrality is distinct from fitness-based neutrality (η) defined in C.15, as it specifically pertains to the preservation of phenotype rather than fitness.

F Directed Evolution

This section provides details regarding how each directed evolution (DE) approach in Section 4.5 is implemented. Specifically, we considered 5 DE variants. For each approach, the results are evaluated by the highest fitness variant they identified. To enable comparison across tasks, this is reported as percentiles from 0 to 1, where 1 represents the fitness of the global optimum. Each approach is run with random initialization for 100 repeatations, and we report the average in Section 4.5.

Basic DE. In this simpliest form, DE is implemented via a greedy adaptive walk algorithm starting from a random variant $g \in \mathcal{G}$. For each step, it exhaustively searches within its neighborhood for the single-point mutation $g \to g', (g' \in \mathcal{N}(g))$ that yields the highest fitness increase (i.e, Δf), until a local optimum is reached.

MLDE. In this paradigm, a supervised ML model (TabPFN [27])² is trained on a set of N randomly sampled protein variants from \mathcal{G} along with their fitness. Following [147, 148, 95], we set N = 384

²We also experimented with other common models including XGBoost [146] and a convolutionary neural network (CNN) [116]. We report results for TabPFN in Section 4.5 as it yielded the highest performance.

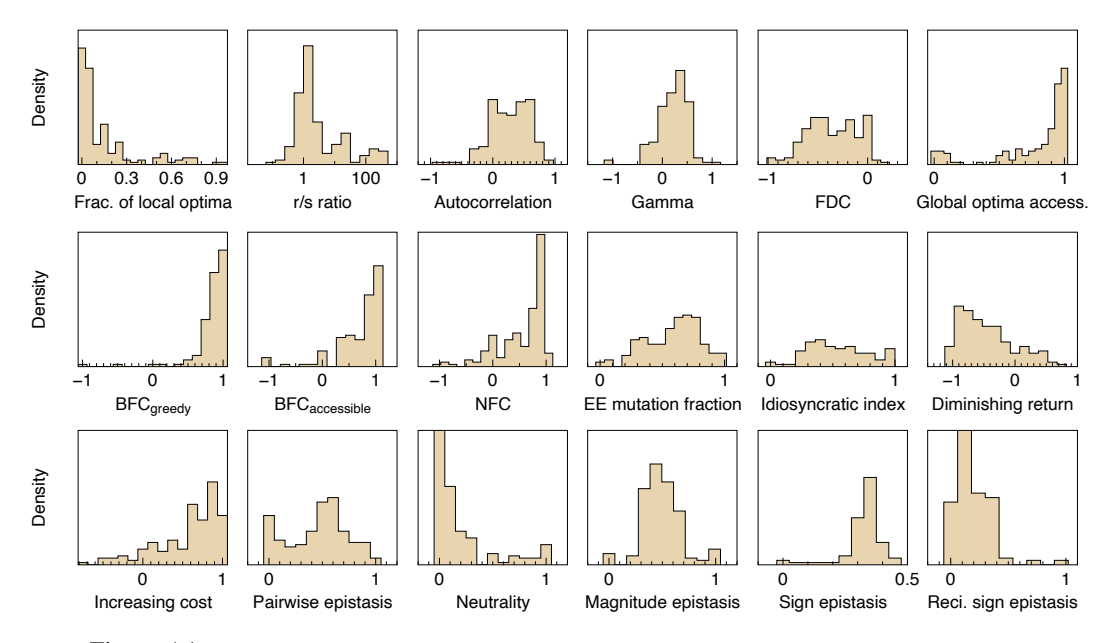


Figure A1: Distribution of landscape features across our combinatorially complete datasets.

as performance typically plateaus at this value. Increasing the sample size beyond this point yields only marginal gains while incurring higher costs. During training, protein sequences were represented using one-hot encoding flattened over the mutated sites. The trained model was then employed to predict fitness values for the entire library, with the top 96 predicted variants selected for evaluation.

MLDE with zero-shot warm start. Instead of randomly selecting the training set from the entire search space \mathcal{G} , this approach first uses a zero-shot predictor (ESM [149] here) to identify prominent regions composed of the top ranked 10% variants. The initial training samples are then sampled from these regions to bias the learning towards them. The subsequent steps are the same as in MLDE.

ALDE. This active learning-assisted DE implements an iterative learning strategy with 3 or 5 rounds. In each round, the ML model (TabPFN) is trained on all data acquired up to that point. The initial round involves the same random sampling as in MLDE with N=96. For subsequent rounds, the ML model serves as an acquisition function to rank all variants in the library, thus guiding the selection of the next batch of variants for fitness evaluation. After the final round, the trained model predicts fitness values, and the top 96 variants are selected for analysis for evaluation.

ALDE with zero-shot warm start. This approach is almost identical to ALDE, except that insteading of randomly sampling the initial 96 variants, it employs the same zero-shot ranking as in MLDE with zero-shot warm start.

G Additional Results

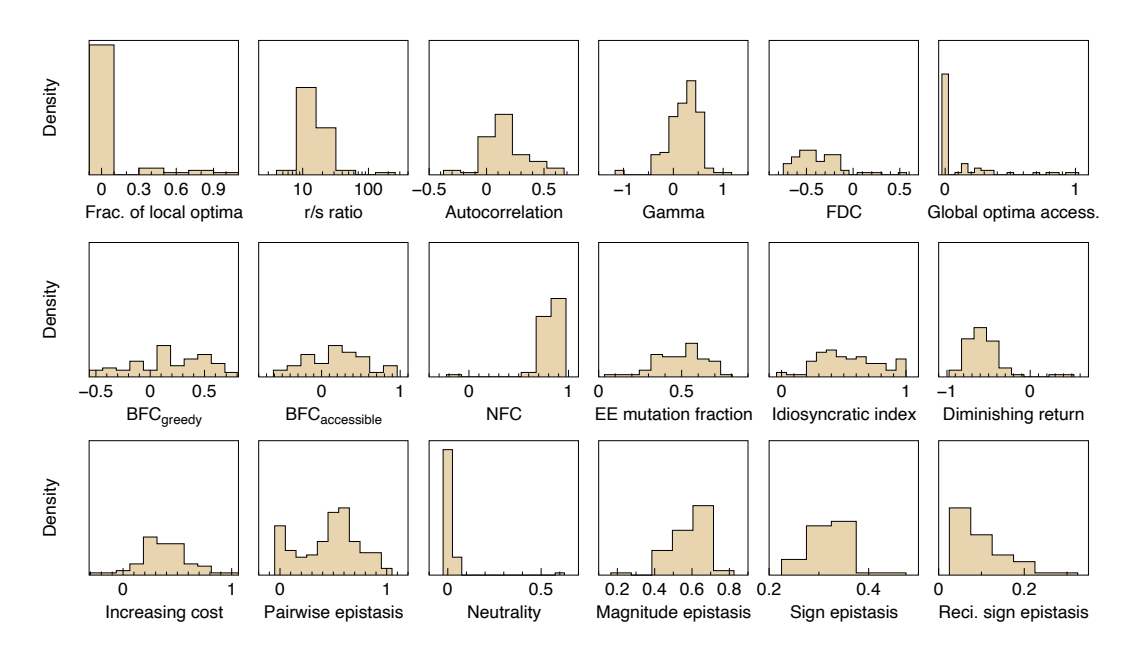


Figure A2: Distribution of landscape features across ProteinGym tasks.

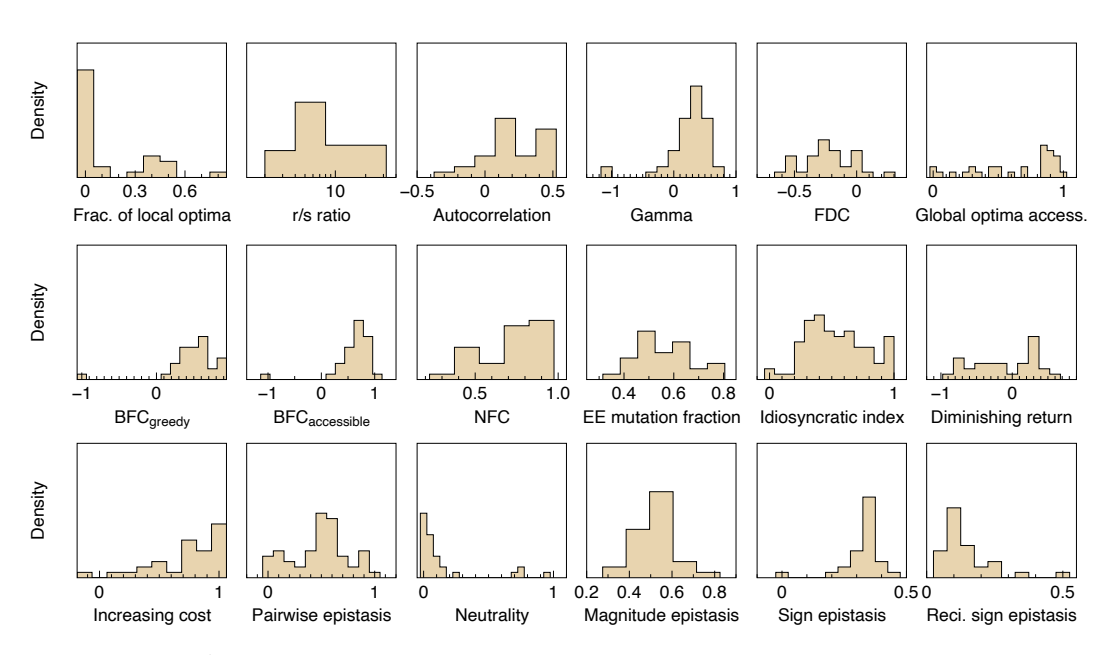


Figure A3: Distribution of landscape features across ProteinGym tasks.

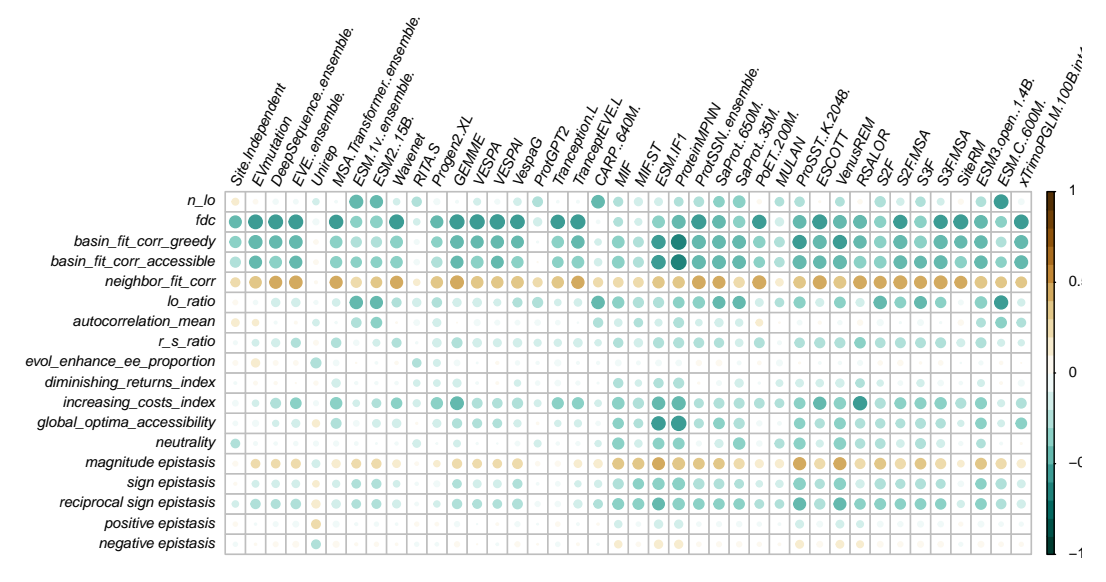


Figure A4: Spearman correlation between fitness landscape features and the performance of zero-shot protein fitness models on ProteinGym tasks. Due to the vast number of baslines on ProteinGym leaderboard, we only display representative ones here for each model series. Model performances are reported as Spearman's ρ between predicted and true fitness.

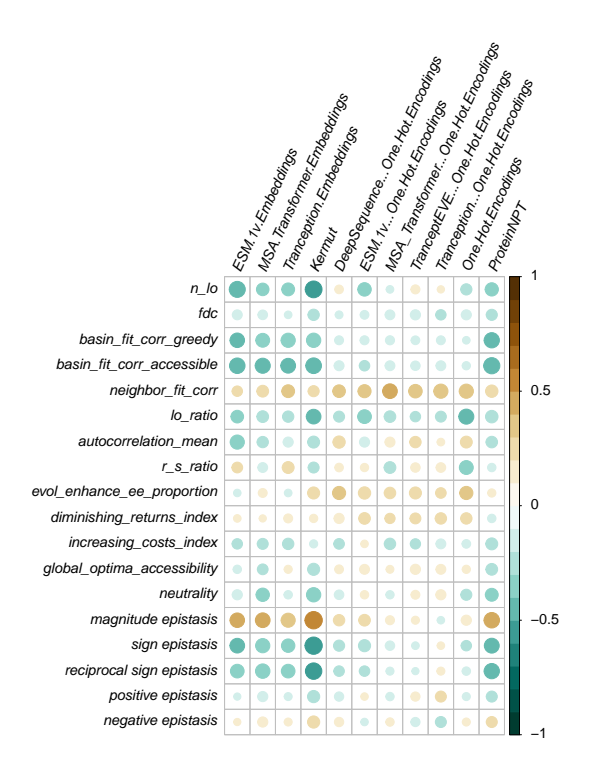


Figure A5: Spearman correlation between fitness landscape features and the performance of supervised protein fitness models on ProteinGym tasks. Model performances are reported as Spearman's ρ between predicted and true fitness.

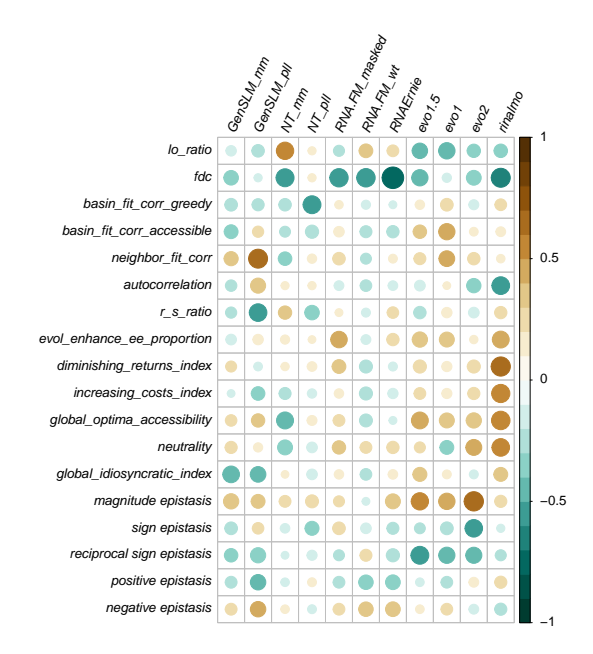


Figure A6: Spearman correlation between fitness landscape features and the performance of supervised RNA fitness models on RNAGym tasks. Model performances are reported as Spearman's ρ between predicted and true fitness.

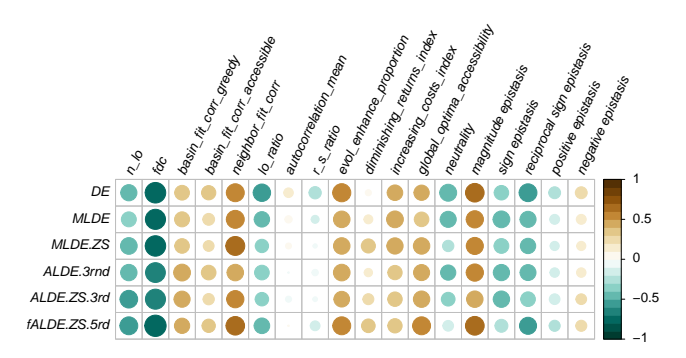


Figure A7: Spearman correlation between fitness landscape features and the performance of 5 directed evolution (DE) approaches on 20 combinatorially complete protein fitness landscapes. Model performances are reported as the maximum fitness (normalized to [0,1] by taking percentiles) reached, averaged across 100 randomly initialized repeatations.

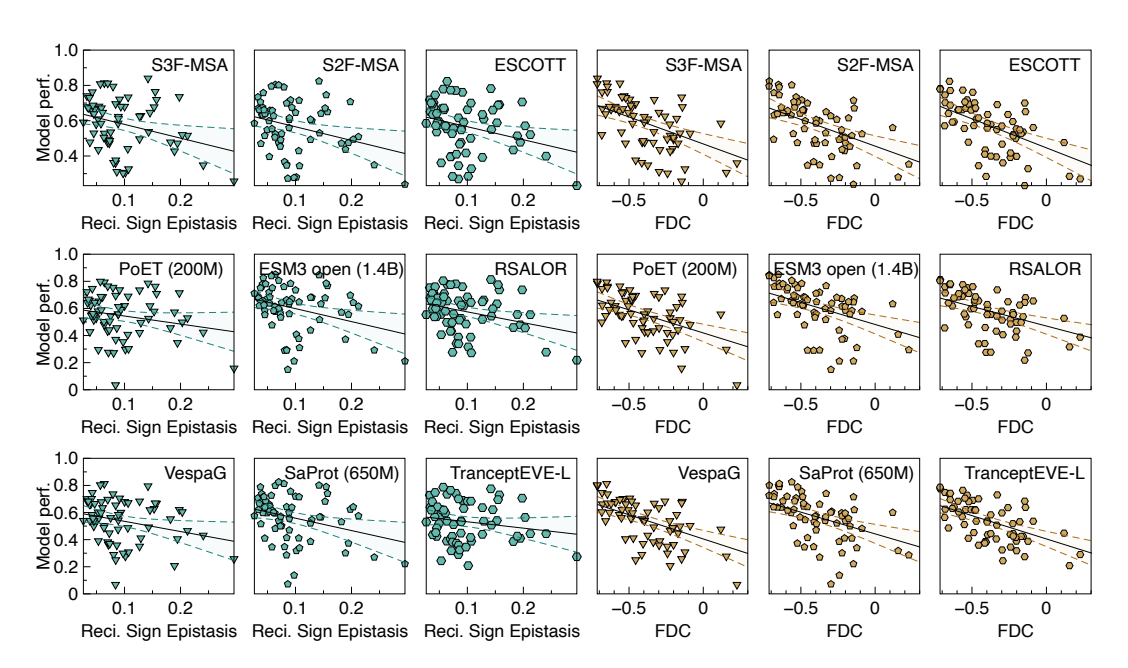


Figure A8: Influence of landscape features on protein fitness model performance on ProteinGym. We plot the distribution of model (name specified in each plot) performance (y-axis; measured as Spearman's ρ) against landscape features (x-axis). Straight lines show a fit of the linear regression model, and shaded regions depict the 95% confidence intervals. References: S3F-MSA [150], ESCOTT [151], PoET [152], ESM3 [153], RSALOR [154], VespaG [155], SaProt [156], and TranceptEVE-L [157].

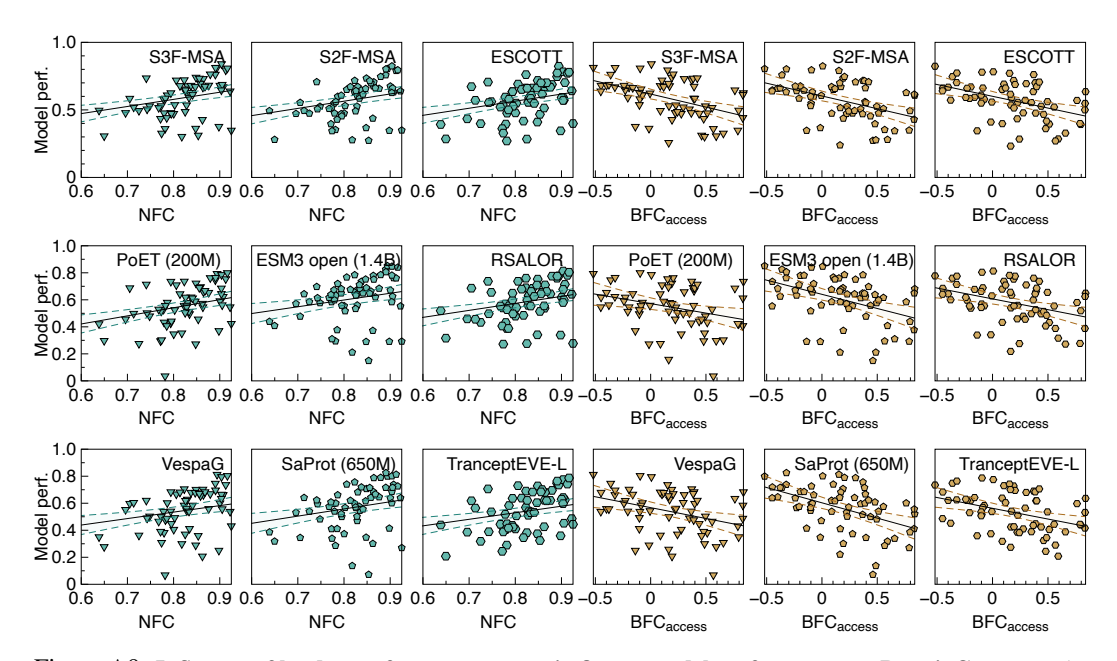


Figure A9: Influence of landscape features on protein fitness model performance on ProteinGym. We plot the distribution of model (name specified in each plot) performance (y-axis; measured as Spearman's ρ) against landscape features (x-axis). Straight lines show a fit of the linear regression model, and shaded regions depict the 95% confidence intervals.

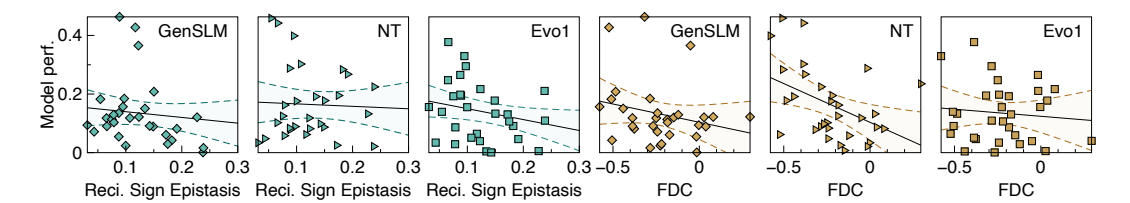


Figure A10: Influence of landscape features on RNA fitness model performance on RNAGym. We plot the distribution of model (name specified in each plot) performance (y-axis; measured as Spearman's ρ) against landscape features (x-axis). Straight lines show a fit of the linear regression model, and shaded regions depict the 95% confidence intervals. References: GenSLM [158], NT [159], and Evol [63].

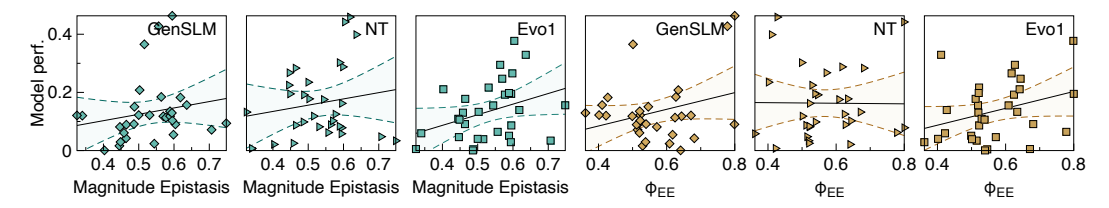


Figure A11: Influence of landscape features on RNA fitness model performance on RNAGym. We plot the distribution of model (name specified in each plot) performance (y-axis; measured as Spearman's ρ) against landscape features (x-axis). Straight lines show a fit of the linear regression model, and shaded regions depict the 95% confidence intervals.

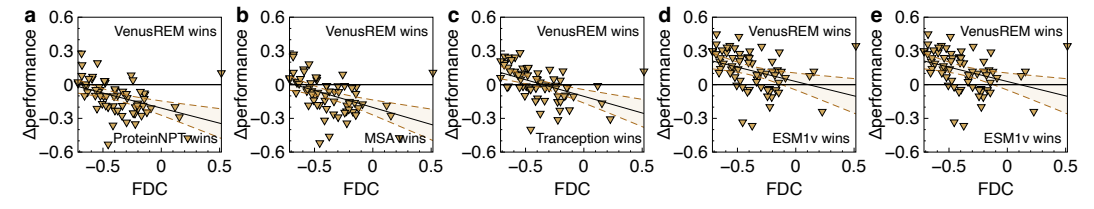


Figure A12: Difference in performance (y-axis) between 5 supervised baselines and VenusREM in ProteinGym is plotted against landscape features on the x-axis. Straight lines show a fit of the linear regression model, and shaded regions depict the 95% confidence intervals. References: VenusREM [24], ProteinNP [87], MSA [160], and Tranception [161].

Table A2: Summary of landscape features for different microbial community-function landscapes.

Feature	[162]	[52]	[54]	[53]	[50]	[119]
\overline{n}	63	54	279	614	21198	1561
$\phi_{ m lo}$	0.032	0.074	0.075	0.040	0.158	0.584
r/s	0.944	0.863	1.417	1.778	3.087	2.294
$ ho_a$	0.528	0.491	0.556	0.490	0.559	0.196
γ	0.384	0.345	0.449	0.330	0.146	0.161
FDC	-0.559	-0.780	-0.587	-0.161	-0.378	-0.487
$lpha_{ m go}$	0.984	0.944	0.888	0.853	0.003	0.003
BFC_{greedy}	1.000	0.800	0.861	0.724	0.502	0.156
BFC_{acc}	1.000	1.000	0.861	0.950	0.409	0.025
NFC	0.919	0.902	0.873	0.820	0.790	0.635
$\phi_{ ext{EE}}$	0.683	0.709	0.644	0.625	0.535	0.402
$I_{ m id}$	0.398	0.395	0.539	0.639	0.552	0.605
$\epsilon_{ m DR}$	-0.741	-0.314	-0.603	-0.194	0.043	-0.319
$\epsilon_{ m IC}$	0.648	0.871	0.574	0.728	0.816	0.583
$\epsilon_{(2)}$	0.861	0.869	0.633	0.361	0.547	0.675
η	0.038	0.000	0.527	0.183	0.000	0.000
$\epsilon_{ m mag}$	0.489	0.543	0.496	0.447	0.404	0.457
$\epsilon_{ m sign}$	0.431	0.413	0.396	0.375	0.395	0.354
$\epsilon_{ m reci}$	0.080	0.043	0.108	0.178	0.201	0.189
$\epsilon_{ m pos}$	0.764	0.768	0.742	0.840	0.841	0.774
$\epsilon_{ m neg}$	0.236	0.232	0.258	0.160	0.159	0.226

Table A3: Selected landscape features for combinatorially complete fitness landscapes

Author	Ref.	SubID	Space	Size	$\phi_{\mathrm{lo}}(\%)$	ρ_a (%)	NFC	γ	$\epsilon_{ m reci}$	$\epsilon_{ m DR}$	FDC	$\phi_{ ext{EE}}$	η
Kuo2020	[163]	-	Nucleotide	$4^9 = 262,144$	0.012	0.573	0.917	0.454	0.206	0.391	-0.235	0.669	0.074
Papkou2023	[4]	DHFR	Nucleotide	$4^9 = 262,144$	0.004	0.641	0.954	0.399	0.255	0.065	-0.140	0.553	0.076
PodgornaiaL15	[47]	PhoQ	Protein	$20^4 = 160,000$	0.013	0.241	0.540	NaN	0.234	0.469	-0.196	0.609	0.282
Wu2016	[59]	GB1	Protein	$20^4 = 160,000$	0.001	0.406	0.872	0.440	0.221	0.499	-0.123	0.621	0.717
Jalal2020	[78]	ParB	Protein	$20^4 = 160,000$	0.005	0.450	0.594	0.120	0.284	-0.107	-0.310	0.519	0.002
Jalal2020	[78]	Noc	Protein	$20^4 = 160,000$	0.004	0.346	0.388	0.131	0.331	-0.164	-0.313	0.426	0.003
Tu2022	[79]	TEV	Protein	$20^4 = 160,000$	0.007	0.053	0.242	0.031	0.309	-0.655	0.008	0.510	0.141
Tu2022	[79]	T7	Protein	$20^3 = 8,000$	0.018	-0.025	-0.172	NaN	0.341	-0.855	0.036	0.380	0.018
Johnston2024	[7]	TrpB4	Protein	$20^4 = 160,000$	0.005	0.399	0.831	0.195	0.294	0.393	-0.112	0.562	0.343
Johnston2024	[7]	TrpB3A	Protein	$20^3 = 8,000$	0.008	0.161	0.485	0.036	0.256	-0.239	-0.178	0.621	0.167
Johnston2024	[7]	TrpB3B	Protein	$20^3 = 8,000$	0.009	0.074	0.306	0.025	0.295	-0.326	-0.021	0.555	0.205
Johnston2024	[7]	TrpB3C	Protein	$20^3 = 8,000$	0.008	0.115	0.395	0.020	0.284	-0.585	-0.065	0.572	0.089
Johnston2024	[7]	TrpB3D	Protein	$20^3 = 8,000$	0.006	0.251	0.676	0.145	0.264	0.325	-0.125	0.611	0.175
Johnston2024	[7]	TrpB3E	Protein	$20^3 = 8,000$	0.012	0.113	0.498	0.030	0.316	0.153	-0.036	0.500	0.339
Johnston2024	[7]	TrpB3F	Protein	$20^3 = 8,000$	0.011	0.105	0.390	0.026	0.309	-0.236	-0.197	0.500	0.179
Johnston2024	[7]	TrpB3G	Protein	$20^3 = 8,000$	0.010	0.162	0.543	0.043	0.305	0.184	-0.176	0.514	0.313
Johnston2024	[7]	TrpB3H	Protein	$20^3 = 8,000$	0.015	0.046	0.253	0.011	0.322	0.110	-0.012	0.475	0.346
Johnston2024	[7]	TrpB3I	Protein	$20^3 = 8,000$	0.002	0.433	0.856	0.275	0.171	0.373	-0.240	0.726	0.145
Domingo2018	[42]	-	Nucleotide	$2^6 \times 3^4 = 5,184$	0.021	0.517	0.777	0.114	0.182	-0.757	-0.506	0.681	0.076
Phillips2021	[117]	CR6261-h1	Mutation	$2^{11} = 2,048$	0.011	0.561	0.820	0.538	0.044	-0.956	-0.379	0.794	0.075
Phillips2021	[117]	CR6261-h9	Mutation	$2^{11} = 2,048$	0.019	0.547	0.794	0.420	0.026	-0.901	-0.575	0.794	0.037
Phillips2021	[117]	CR9114-h1	Mutation	$2^{16} = 65,536$	0.013	0.765	0.956	0.391	0.118	-0.945	-0.219	0.673	0.093
Phillips2021	[117]	CR9114-h3	Mutation	$2^{16} = 65,536$	0.563	0.411	0.198	NaN	0.071	-0.400	-0.354	0.586	0.019
Phillips2021	[117]	CR9114-flueB	Mutation	$2^{16} = 65,536$	0.972	-0.062	-0.162	NaN	0.118	-0.304	-0.089	0.278	0.018
Phillips2023	[164]	CH65-SI06	Mutation	$2^{16} = 65,536$	0.481	0.655	0.741	0.442	0.082	-0.474	-0.498	0.672	0.026
Phillips2023	[164]	CH65-MA90	Mutation	$2^{16} = 65,536$	0.000	0.831	0.991	0.481	0.078	-0.320	-0.534	0.798	0.070
Phillips2023	[164]	CH65-G189E	Mutation	$2^{16} = 65,536$	0.144	0.664	0.860	0.408	0.072	0.569	-0.554	0.763	0.034
Westmann24	[34]	-	Nucleotide	$4^8 = 65,536$	0.118	0.202	0.362	0.072	0.305	-0.170	-0.111	0.457	0.053
Soo2021	[118]	30C	Nucleotide	$4^8 = 65,536$	0.015	0.445	0.773	0.219	0.231	-0.743	-0.260	0.648	0.007
Soo2021	[118]	37C	Nucleotide	$4^8 = 65,536$	0.021	0.419	0.748	0.196	0.240	-0.785	-0.004	0.639	0.008
Wong2018	[165]	BRCA2	Nucleotide	32,768	0.022	0.535	0.897	0.444	0.290	0.247	0.019	0.529	0.143

Table A3 – continued from previous page

			'	Table A3 – continued	from pre	evious pag	ge						
Author	Ref.	SubID	Space	Size	$\phi_{ m lo}$	ρ_a	NFC	γ	$\epsilon_{ m reci}$	$\epsilon_{ m DR}$	FDC	$\phi_{ ext{EE}}$	η
Wong2018	[165]	SMN1	Nucleotide	32,768	0.009	0.502	0.861	0.421	0.183	0.290	0.011	0.668	0.096
Wong2018	[165]	IKBKAP	Nucleotide	32,768	0.036	0.392	0.808	0.380	0.375	0.216	0.004	0.372	0.102
Moulana2022	[166]	ACE	Mutation	$2^{15} = 32,768$	0.001	0.833	0.993	0.536	0.058	-0.875	-0.485	0.848	0.050
Moulana2023	[167]	CB6	Mutation	$2^{15} = 32,768$	0.006	0.811	0.965	0.368	0.107	-0.593	-0.394	0.774	0.040
Moulana2023	[167]	CoV555	Mutation	$2^{15} = 32,768$	0.020	0.770	0.957	0.180	0.201	-0.707	-0.150	0.598	0.040
Moulana2023	[167]	REGN10987	Mutation	$2^{15} = 32,768$	0.007	0.716	0.924	0.222	0.160	-0.817	-0.449	0.680	0.055
Moulana2023	[167]	S309	Mutation	$2^{15} = 32,768$	0.006	0.775	0.962	0.348	0.115	-0.535	-0.339	0.696	0.071
Bendixsen2019	[168]	HDV	Mutation	$2^{14} = 16,384$	0.071	0.239	0.240	0.218	0.410	0.192	0.140	0.271	0.232
Bendixsen2019	[168]	Ligase	Mutation	$2^{14} = 16,384$	0.004	0.347	0.803	0.510	0.137	0.418	-0.437	0.705	0.810
Poelwijk2019	[169]	eqFP611	Mutation	$2^{13} = 8,192$	0.009	0.675	0.979	0.452	0.187	-0.281	0.077	0.623	0.146
Lite2020	[170]	ParD2	Protein	$20^3 = 8,000$	0.001	0.577	0.960	0.319	0.113	-0.348	-0.302	0.796	0.058
Lite2020	[170]	ParD3	Protein	$20^3 = 8,000$	0.001	0.579	0.957	0.287	0.068	-0.560	-0.245	0.851	0.052
Centurion2019	[171]	-	Mutation	$2^{10} \times 3 = 3,072$	0.032	0.657	0.919	0.366	0.155	-0.850	-0.050	0.751	0.053
Schulz2025	[172]	-	Mutation	$2^{10} = 1,024$	0.036	0.653	0.911	0.215	0.153	-0.820	-0.223	0.689	0.016
Bakerlee2022	[39]	hap-4NQ0	Mutation	$2^{10} = 1,024$	0.479	0.029	0.025	0.175	0.273	-0.536	-0.037	0.351	0.953
Bakerlee2022	[39]	hap-37C	Mutation	$2^{10} = 1,024$	0.630	0.013	0.039	0.081	0.422	0.044	0.043	0.278	0.977
Bakerlee2022	[39]	hap-gu	Mutation	$2^{10} = 1,024$	0.681	-0.009	-0.004	-0.039	0.377	-0.377	0.034	0.205	0.964
Bakerlee2022	[39]	hap-salt	Mutation	$2^{10} = 1,024$	0.774	-0.101	0.045	0.299	0.282	0.408	0.015	0.245	0.959
Bakerlee2022	[39]	hap-suloc	Mutation	$2^{10} = 1,024$	0.510	-0.024	-0.013	-0.036	0.434	0.114	-0.046	0.224	0.992
Bakerlee2022	[39]	hap-YPDA	Mutation	$2^{10} = 1,024$	0.633	0.007	0.012	0.083	0.378	-0.943	0.039	0.271	0.972
Bakerlee2022	[39]	hom-4NQO	Mutation	$2^{10} = 1,024$	0.570	0.065	0.048	0.185	0.305	-0.417	-0.033	0.326	0.936
Bakerlee2022	[39]	hom-37C	Mutation	$2^{10} = 1,024$	0.535	0.022	0.024	0.052	0.412	-0.163	-0.015	0.235	0.992
Bakerlee2022	[39]	hom-gu	Mutation	$2^{10} = 1,024$	0.740	-0.043	0.012	0.086	0.357	-0.452	0.000	0.209	0.925
Bakerlee2022	[39]	hom-salt	Mutation	$2^{10} = 1,024$	0.770	-0.129	0.027	0.190	0.250	-0.005	-0.032	0.277	0.881
Bakerlee2022	[39]	hom-suloc	Mutation	$2^{10} = 1,024$	0.549	0.005	-0.004	0.001	0.320	-1.000	0.026	0.325	0.982
Bakerlee2022	[39]	hom-YPDA	Mutation	$2^{10} = 1,024$	0.569	0.031	0.020	0.103	0.355	-0.707	-0.051	0.268	0.958
Bank2016	[115]	-	Mutation	640	0.027	0.476	0.807	0.210	0.117	0.190	-0.411	0.780	0.000
Bank2016	[115]	-	Mutation	$2^6 = 64$	0.062	0.403	0.886	0.606	0.125	-0.965	-0.126	0.719	0.250
Wu2020	[173]	Bei89	Mutation	576	0.005	0.651	0.980	0.475	0.024	-0.556	-0.428	0.916	0.008
Wu2020	[173]	Bk79	Mutation	576	0.002	0.627	0.967	0.475	0.055	-0.354	-0.519	0.856	0.006
Wu2020	[173]	Bris07L194	Mutation	576	0.007	0.680	0.951	0.466	0.141	-0.087	-0.463	0.726	0.009
Wu2020	[173]	Bris07P194	Mutation	576	0.052	0.359	0.719	0.191	0.272	0.288	-0.405	0.540	0.006
Wu2020	[173]	HK68	Mutation	576	0.016	0.595	0.946	0.522	0.070	-0.711	-0.260	0.846	0.007

Table A3 – continued from previous page

				Table A3 – continu	ed from pre	vious pag	e						
Author	Ref.	SubID	Space	Size	$\phi_{ ext{lo}}$	$ ho_a$	NFC	γ	$\epsilon_{ m reci}$	$\epsilon_{ m DR}$	FDC	$\phi_{ ext{EE}}$	η
Wu2020	[173]	Mos99	Mutation	576	0.012	0.632	0.941	0.399	0.089	-0.621	-0.498	0.809	0.006
Wu2020	[173]	NDako16	Mutation	576	0.003	0.700	0.971	0.523	0.040	-0.251	-0.644	0.875	0.011
Lunzer2005	[6]	fitness	Protein	512	0.002	0.496	0.918	0.639	0.019	-0.978	-0.586	0.939	0.003
Lunzer2005	[6]	NAD	Protein	512	0.002	0.561	0.953	-0.024	0.000	-0.762	-0.503	1.000	0.036
Lunzer2005	[6]	NADP	Protein	512	0.002	0.685	0.972	-0.004	0.000	-0.671	-0.665	1.000	0.000
Doud2024	[174]	base	Mutation	$2^9 = 512$	0.016	0.568	0.921	0.549	0.105	-0.462	-0.346	0.740	0.005
Doud2024	[174]	LamB	Mutation	$2^9 = 512$	0.012	0.625	0.939	0.511	0.133	-0.057	-0.548	0.729	0.011
Doud2024	[174]	Lspec	Mutation	$2^9 = 512$	0.026	0.586	0.932	0.628	0.107	-0.594	-0.270	0.722	0.008
Doud2024	[174]	OmpF	Mutation	$2^9 = 512$	0.040	0.558	0.901	0.538	0.124	-0.460	-0.265	0.681	0.009
Doud2024	[174]	Ospec	Mutation	$2^9 = 512$	0.020	0.541	0.931	0.619	0.097	-0.859	-0.108	0.753	0.011
Colunga2024	[51]	colorants	Mutation	$2^8 = 256$	0.004	0.730	0.996	0.162	0.001	-0.507	-0.854	0.981	0.015
Colunga2024	[51]	pseudo	Mutation	$2^8 = 256$	0.035	0.396	0.782	0.290	0.198	-0.838	-0.306	0.615	0.055
Hall2020	[175]	NfsA-2039	Mutation	$2^7 = 128$	0.016	0.586	0.945	0.404	0.074	-0.461	-0.363	0.738	0.518
Hall2020	[175]	NfsA-3637	Mutation	$2^7 = 128$	0.031	0.601	0.946	0.392	0.071	-0.496	-0.509	0.770	0.107
Frohlich2021	[176]	CAZtraj1	Mutation	$2^4 = 16$	0.062	0.228	0.867	0.322	0.083	-0.333	-0.714	0.719	0.156
Frohlich2021	[176]	CAZtraj2	Mutation	$2^6 = 64$	0.031	0.523	0.942	0.600	0.026	-0.149	-0.446	0.880	0.047
Frohlich2021	[176]	CAZtraj3	Mutation	$2^6 = 64$	0.016	0.513	0.962	0.320	0.100	-0.367	-0.433	0.647	0.258
Frohlich2021	[176]	PIPtraj1	Mutation	$2^4 = 16$	0.125	0.182	0.745	0.044	0.125	-0.621	0.000	0.625	0.688
Frohlich2021	[176]	PIPtraj2	Mutation	$2^6 = 64$	0.016	0.418	0.862	0.423	0.106	-0.171	-0.373	0.649	0.455
Frohlich2021	[176]	PIPtraj3	Mutation	$2^6 = 64$	0.062	0.581	0.958	0.030	0.151	-0.719	-0.441	0.587	0.032
Hall2010	[177]	Haploid	Mutation	$2^6 = 64$	0.141	0.239	0.483	-0.150	0.292	-0.814	-0.263	0.469	0.245
Hall2010	[177]	Diploid	Mutation	$2^6 = 64$	0.125	0.214	0.451	-0.235	0.342	-0.746	-0.316	0.443	0.130
Tamer2019	[178]	kcat-trajr	Mutation	$2^5 = 32$	0.125	0.222	0.706	0.253	0.163	-0.941	-0.214	0.575	0.163
Tamer2019	[178]	kcat-trajg	Mutation	$2^5 = 32$	0.125	0.256	0.800	0.480	0.150	-0.961	-0.357	0.662	0.075
Tamer2019	[178]	ki-trajr	Mutation	$2^5 = 32$	0.031	0.471	0.966	0.192	0.000	-0.066	-0.952	1.000	0.000
Tamer2019	[178]	ki-trajg	Mutation	$2^5 = 32$	0.031	0.472	0.971	0.510	0.000	0.333	-0.959	1.000	0.000
Lozovsky2021	[179]	ic50-c57	Mutation	$2^4 = 16$	0.125	0.006	0.320	-0.059	0.133	-0.271	-0.594	0.414	0.000
Lozovsky2021	[179]	ic50-c58	Mutation	$2^4 = 16$	0.188	0.034	0.342	-0.330	0.125	-0.233	-0.539	0.483	0.000
Lozovsky2021	[179]	ic50-c59	Mutation	$2^4 = 16$	0.125	-0.039	0.132	-0.169	0.167	0.594	-0.606	0.407	0.000
Lozovsky2021	[179]	ic50-c60	Mutation	$2^4 = 16$	0.250	-0.167	-0.064	-0.232	0.222	-0.477	-0.184	0.400	0.240
Lozovsky2021	[179]	ic50-c61	Mutation	$2^4 = 16$	0.312	-0.139	-0.010	0.015	0.167	-0.394	-0.536	0.273	0.000
Hall2019	[180]	Acetate	Mutation	$2^5 = 32$	0.094	0.171	0.494	-0.060	0.200	-0.757	-0.250	0.500	0.100
Hall2019	[180]	Beef	Mutation	$2^5 = 32$	0.062	0.365	0.878	0.558	0.125	-0.477	-0.561	0.738	0.075

Table A3 – continued from previous page

				Table A3 – co	ntinued from pro	evious pag	ge						
Author	Ref.	SubID	Space	Size	$\phi_{ ext{lo}}$	$ ho_a$	NFC	γ	ϵ_{reci}	$\epsilon_{ m DR}$	FDC	$\phi_{ ext{EE}}$	η
Hall2019	[180]	Casamino	Mutation	$2^5 = 32$	0.062	0.303	0.774	0.309	0.125	-0.735	-0.493	0.625	0.050
Hall2019	[180]	Glucose	Mutation	$2^5 = 32$	0.031	0.421	0.904	0.162	0.050	-0.775	-0.843	0.850	0.050
Hall2019	[180]	Milk	Mutation	$2^5 = 32$	0.062	0.392	0.876	0.276	0.050	0.089	-0.625	0.775	0.062
Hall2019	[180]	NAG	Mutation	$2^5 = 32$	0.062	0.411	0.911	0.420	0.075	-0.742	-0.601	0.713	0.100
Hall2019	[180]	Rhamnose	Mutation	$2^5 = 32$	0.062	0.329	0.858	0.461	0.087	-0.303	-0.779	0.800	0.037
Hall2019	[180]	Trypsin	Mutation	$2^5 = 32$	0.094	0.261	0.753	0.432	0.163	-0.785	-0.640	0.650	0.113
Whitlock2000	[181]	-	Mutation	$2^5 = 32$	0.094	0.267	0.734	0.391	0.138	-0.897	-0.739	0.750	0.000
deVisser2009	[182]	-	Mutation	$2^5 = 32$	0.156	0.156	0.416	-0.401	0.300	-0.617	-0.568	0.388	0.200
daSilva2010	[183]	CCR5	Mutation	$2^5 = 32$	0.094	0.240	0.680	0.336	0.200	-0.615	-0.569	0.636	0.013
daSilva2010	[183]	CXCR5	Mutation	$2^5 = 32$	0.094	0.137	0.469	0.215	0.197	-0.476	0.112	0.544	0.000
Sunden2015	[184]	AP	Mutation	$2^5 = 32$	0.031	0.456	0.960	0.529	0.037	-0.242	-0.714	0.863	0.000
Anderson2021	[185]	MPH-CaPTM	Mutation	$2^5 = 32$	0.036	0.269	0.844	0.710	0.038	-0.511	-0.507	0.810	0.016
Anderson2021	[185]	MPH-CdPTM	Mutation	$2^5 = 32$	0.031	0.407	0.905	0.538	0.075	-0.464	-0.470	0.738	0.025
Anderson2021	[185]	MPH-CoPTM	Mutation	$2^5 = 32$	0.031	0.373	0.887	0.494	0.025	-0.273	-0.445	0.887	0.000
Anderson2021	[185]	MPH-CuPTM	Mutation	$2^5 = 32$	0.031	0.326	0.834	0.441	0.087	-0.204	-0.476	0.750	0.013
Anderson2021	[185]	MPH-MgPTM	Mutation	$2^5 = 32$	0.062	0.362	0.893	0.770	0.050	-0.376	-0.465	0.863	0.000
Anderson2021	[185]	MPH-MnPTM	Mutation	$2^5 = 32$	0.062	0.411	0.931	0.831	0.037	-0.548	-0.440	0.863	0.025
Mira2015	[186]	TEM-AMP	Mutation	$2^4 = 16$	0.688	-0.672	-0.723	-0.222	1.000	-1.000	-0.368	0.067	0.200
Mira2015	[186]	TEM-AM	Mutation	$2^4 = 16$	0.125	-0.008	0.382	0.351	0.083	-0.989	-0.169	0.594	0.719
Mira2015	[186]	TEM-CEC	Mutation	$2^4 = 16$	0.188	0.065	0.407	0.259	0.333	-0.848	0.038	0.406	0.000
Mira2015	[186]	TEM-CTX	Mutation	$2^4 = 16$	0.250	0.002	0.271	-0.260	0.375	-0.544	-0.184	0.312	0.000
Mira2015	[186]	TEM-ZOX	Mutation	$2^4 = 16$	0.125	0.015	0.313	-0.401	0.333	-0.715	-0.614	0.344	0.344
Mira2015	[186]	TEM-CXM	Mutation	$2^4 = 16$	0.125	0.090	0.537	0.304	0.167	-0.721	-0.683	0.594	0.000
Mira2015	[186]	TEM-CRO	Mutation	$2^4 = 16$	0.250	-0.015	0.192	-0.306	0.250	-0.599	-0.161	0.406	0.031
Mira2015	[186]	TEM-AMC	Mutation	$2^4 = 16$	0.875	-0.938	-1.000	NaN	0.000	NaN	-0.214	0.000	0.000
Mira2015	[186]	TEM-CAZ	Mutation	$2^4 = 16$	0.688	-0.743	-0.953	NaN	1.000	0.408	-0.160	0.000	0.143
Mira2015	[186]	TEM-CTT	Mutation	$2^4 = 16$	0.312	-0.142	-0.212	0.228	0.375	-0.949	-0.107	0.250	0.000
Mira2015	[186]	TEM-SAM	Mutation	$2^4 = 16$	0.062	0.101	0.701	0.292	0.048	-0.953	-0.430	0.677	0.645
Mira2015	[186]	TEM-CPR	Mutation	$2^4 = 16$	0.188	0.018	0.259	-0.242	0.292	-0.875	-0.268	0.375	0.000
Mira2015	[186]	TEM-CPD	Mutation	$2^4 = 16$	0.125	0.116	0.515	-0.245	0.125	-0.617	-0.445	0.562	0.000
Mira2015	[186]	TEM-TZP	Mutation	$2^4 = 16$	0.125	0.180	0.745	0.468	0.125	-0.903	-0.545	0.719	0.688
Mira2015	[186]	TEM-FSP	Mutation	$2^4 = 16$	0.250	-0.202	-0.437	-0.241	0.458	-0.963	-0.499	0.219	0.000
Meini2015	[187]	-	Mutation	$2^4 = 16$	0.062	0.209	0.798	0.501	0.000	-0.682	-0.627	0.741	0.000

Table A3 – continued from previous page

Author	Ref.	SubID	Space	Size	$\phi_{ ext{lo}}$	ρ_a	NFC	γ	$\epsilon_{ m reci}$	$\epsilon_{ m DR}$	FDC	$\phi_{ ext{EE}}$	η
Lozovsky2009	[188]	P. falciparum	Mutation	$2^4 = 16$	0.125	-0.009	0.111	-0.103	0.167	-0.875	-0.736	0.562	0.031
Jiang2013	[189]	P. vivax	Mutation	$2^4 = 16$	0.062	0.212	0.762	0.013	0.125	-0.927	-0.652	0.625	0.000
Ogbunugafor2022	[190]	Pyrimethamine	Mutation	$(2^4) \times 12$	0.200	-0.027	0.235	0.251	0.333	-0.884	-0.187	0.321	0.071
Ogbunugafor2022	[190]	Cycloguanil	Mutation	$(2^4) \times 12$	0.200	-0.022	0.235	0.250	0.333	-0.884	-0.187	0.321	0.071
Weinreich20016	[5]	Cefotaxime	Mutation	$2^5 = 32$	0.031	0.363	0.821	0.149	0.049	-0.484	-0.728	0.682	0.000
Khan2011	[41]	DM25	Mutation	$2^5 = 32$	0.062	0.253	0.652	-0.057	0.087	-0.614	-0.724	0.700	0.287
Flynn2013	[191]	DM25-EGTA	Mutation	$2^5 = 32$	0.094	0.214	0.597	0.202	0.087	-0.156	-0.608	0.662	0.175
Flynn2013	[191]	DM25-guanazole	Mutation	$2^5 = 32$	0.094	0.212	0.597	0.202	0.087	-0.156	-0.608	0.662	0.175
Chou2011	[38]	-	Mutation	$2^4 = 16$	0.062	0.310	0.993	0.570	0.000	-0.742	-0.836	1.000	0.000
Malcolm1990	[192]	Diploid	Mutation	$2^3 = 8$	0.125	0.013	0.961	0.333	0.000	0.085	-0.951	0.917	0.000
Guerrero2019	[193]	C-muri-GroEL	Mutation	$2^3 = 8$	0.250	-0.062	0.571	0.333	0.167	-0.992	-0.676	0.583	0.750
Guerrero2019	[193]	C-muri-LON	Mutation	$2^3 = 8$	0.250	-0.227	-0.150	-0.333	0.333	-0.976	-0.025	0.333	0.500
Guerrero2019	[193]	C-muri-WT	Mutation	$2^3 = 8$	0.250	-0.373	-0.864	-0.333	0.333	-0.733	-0.150	0.250	0.083
Guerrero2019	[193]	E.coli-GroEL	Mutation	$2^3 = 8$	0.250	-0.266	-0.218	-0.333	0.333	-0.964	-0.401	0.333	0.250
Guerrero2019	[193]	E.coli-LON	Mutation	$2^3 = 8$	0.125	-0.180	-0.286	-0.333	0.000	-0.943	-0.476	0.417	0.333
Guerrero2019	[193]	E.coli-WT	Mutation	$2^3 = 8$	0.375	-0.358	-0.403	-1.000	0.667	-0.744	-0.175	0.083	0.250
Guerrero2019	[193]	L-grayi-GroEL	Mutation	$2^3 = 8$	0.250	-0.337	-0.505	-0.333	0.333	-0.978	-0.601	0.333	0.500
Guerrero2019	[193]	L-grayi-LON	Mutation	$2^3 = 8$	0.250	-0.263	-0.110	1.000	0.333	-0.999	-0.200	0.333	0.167
Guerrero2019	[193]	L-grayi-WT	Mutation	$2^3 = 8$	0.375	-0.281	-0.173	-1.000	0.667	-0.981	-0.300	0.083	0.833

Table A4: Selected landscape features for ProteinGym tasks with mean mutation depth > 1.

Dataset	Size	Avg. Mutation	$\phi_{ m lo}$	ρ_a	NFC	I_d	ϵ _reci	FDC	$\phi_{ ext{EE}}$	η
PIN1_HUMAN_Tsuboyama_2023_1I6C	802	1.145	0.050	-0.047	0.806	0.157	-0.664	-0.330	0.116	0.022
RAD_ANTMA_Tsuboyama_2023_2CJJ	912	1.151	0.064	-0.054	0.800	0.195	-0.595	-0.524	0.064	0.017
RCD1_ARATH_Tsuboyama_2023_5OAO	1261	1.216	0.048	-0.026	0.696	0.182	-0.777	-0.411	0.204	0.016
RD23A_HUMAN_Tsuboyama_2023_1IFY	1019	1.217	0.044	0.026	0.748	0.064	-0.806	-0.089	0.261	0.015
SRBS1_HUMAN_Tsuboyama_2023_2O2W	1556	1.222	0.042	0.038	0.849	0.033	-0.731	-0.532	0.357	0.016
PSAE_PICP2_Tsuboyama_2023_1PSE	1579	1.228	0.042	0.028	0.830	0.153	-0.514	0.515	0.303	0.022
RPC1_BP434_Tsuboyama_2023_1R69	1459	1.230	0.045	0.010	0.823	0.091	-0.697	-0.495	0.316	0.011
RL20_AQUAE_Tsuboyama_2023_1GYZ	1461	1.233	0.041	0.036	0.907	0.040	-0.871	-0.680	0.347	0.022
TNKS2_HUMAN_Tsuboyama_2023_5JRT	1479	1.244	0.041	0.050	0.778	0.049	-0.783	-0.226	0.371	0.015
UBR5_HUMAN_Tsuboyama_2023_1I2T	1453	1.247	0.039	0.051	0.786	0.053	-0.789	-0.374	0.367	0.018
NUSG_MYCTU_Tsuboyama_2023_2MI6	1380	1.262	0.040	0.063	0.773	0.045	-0.768	-0.157	0.409	0.015
RBP1_HUMAN_Tsuboyama_2023_2KWH	1332	1.268	0.041	0.052	0.725	0.071	-0.697	-0.200	0.395	0.015
RFAH_ECOLI_Tsuboyama_2023_2LCL	1326	1.269	0.041	0.045	0.650	0.102	-0.351	0.155	0.380	0.017
SPG2_STRSG_Tsuboyama_2023_5UBS	1451	1.291	0.040	0.049	0.823	0.042	-0.589	-0.566	0.404	0.013
CATR_CHLRE_Tsuboyama_2023_2AMI	1903	1.296	0.040	0.019	0.814	0.034	-0.765	-0.141	0.324	0.012
SAV1_MOUSE_Tsuboyama_2023_2YSB	965	1.296	0.048	-0.016	0.768	0.212	-0.659	-0.223	0.326	0.023
CBPA2_HUMAN_Tsuboyama_2023_106X	2068	1.344	0.036	0.090	0.890	0.043	-0.660	-0.681	0.455	0.015
FECA_ECOLI_Tsuboyama_2023_2D1U	1886	1.354	0.038	0.092	0.743	0.063	-0.476	-0.202	0.478	0.012
NUSA_ECOLI_Tsuboyama_2023_1WCL	2028	1.356	0.035	0.104	0.863	0.041	-0.474	-0.541	0.497	0.018
EPHB2_HUMAN_Tsuboyama_2023_1F0M	1960	1.368	0.035	0.086	0.894	0.064	-0.600	-0.651	0.485	0.012
CUE1_YEAST_Tsuboyama_2023_2MYX	1580	1.396	0.035	0.088	0.782	0.089	-0.641	0.118	0.478	0.013
ODP2_GEOSE_Tsuboyama_2023_1W4G	1134	1.410	0.043	0.096	0.782	0.084	-0.808	0.227	0.461	0.022
TCRG1_MOUSE_Tsuboyama_2023_1E0L	1058	1.413	0.036	0.069	0.879	0.155	-0.487	-0.646	0.441	0.021
PR40A_HUMAN_Tsuboyama_2023_1UZC	2033	1.428	0.032	0.132	0.904	0.142	-0.527	-0.713	0.443	0.021
BCHB_CHLTE_Tsuboyama_2023_2KRU	1572	1.434	0.033	0.120	0.794	0.038	-0.821	-0.395	0.586	0.012
SR43C_ARATH_Tsuboyama_2023_2N88	1583	1.438	0.031	0.127	0.865	0.037	-0.600	-0.522	0.572	0.011
MBD11_ARATH_Tsuboyama_2023_6ACV	2116	1.454	0.031	0.121	0.913	0.079	-0.517	-0.646	0.518	0.017
DNJA1_HUMAN_Tsuboyama_2023_2LO1	2264	1.463	0.029	0.149	0.916	0.057	-0.508	-0.714	0.571	0.015
MAFG_MOUSE_Tsuboyama_2023_1K1V	1429	1.467	0.030	0.102	0.838	0.100	-0.558	-0.593	0.536	0.019
RCRO_LAMBD_Tsuboyama_2023_1ORC	2278	1.475	0.028	0.150	0.876	0.054	-0.608	-0.481	0.586	0.019
BBC1_YEAST_Tsuboyama_2023_1TG0	2069	1.476	0.031	0.127	0.779	0.070	-0.510	-0.336	0.563	0.010

Table A4 – continued from previous page

	Table A	4 – continued froi	n previo	us page						
Dataset	Size	Avg. Mutation	$\phi_{ m lo}$	$ ho_a$	NFC	I_d	ϵ _reci	FDC	$\phi_{ ext{EE}}$	η
PITX2_HUMAN_Tsuboyama_2023_2L7M	1824	1.486	0.033	0.121	0.829	0.089	-0.654	-0.397	0.529	0.013
THO1_YEAST_Tsuboyama_2023_2WQG	1279	1.487	0.033	0.109	0.828	0.075	-0.513	-0.551	0.583	0.012
SPA_STAAU_Tsuboyama_2023_1LP1	2105	1.508	0.025	0.149	0.834	0.129	-0.343	-0.471	0.546	0.024
YAIA_ECOLI_Tsuboyama_2023_2KVT	1890	1.509	0.026	0.143	0.847	0.059	-0.739	-0.589	0.569	0.010
ISDH_STAAW_Tsuboyama_2023_2LHR	1944	1.516	0.030	0.153	0.772	0.053	-0.791	-0.292	0.614	0.014
VILI_CHICK_Tsuboyama_2023_1YU5	2568	1.532	0.028	0.222	0.904	0.047	-0.639	-0.621	0.616	0.017
NKX31_HUMAN_Tsuboyama_2023_2L9R	2482	1.537	0.029	0.153	0.826	0.145	-0.566	-0.506	0.541	0.025
DOCK1_MOUSE_Tsuboyama_2023_2M0Y	2915	1.584	0.027	0.149	0.802	0.143	-0.397	-0.333	0.549	0.017
CSN4_MOUSE_Tsuboyama_2023_1UFM	3295	1.589	0.022	0.234	0.833	0.027	-0.644	-0.398	0.673	0.014
CBX4_HUMAN_Tsuboyama_2023_2K28	2282	1.598	0.021	0.164	0.858	0.084	-0.633	-0.456	0.592	0.012
OBSCN_HUMAN_Tsuboyama_2023_1V1C	3197	1.621	0.023	0.194	0.891	0.070	-0.511	-0.561	0.654	0.013
SPTN1_CHICK_Tsuboyama_2023_1TUD	3201	1.672	0.018	0.286	0.868	0.035	-0.583	-0.482	0.698	0.011
YNZC_BACSU_Tsuboyama_2023_2JVD	2300	1.690	0.017	0.180	0.900	0.093	-0.442	-0.632	0.670	0.017
UBE4B_HUMAN_Tsuboyama_2023_3L1X	3622	1.691	0.022	0.177	0.795	0.073	-0.578	-0.170	0.646	0.012
SDA_BACSU_Tsuboyama_2023_1PV0	2770	1.699	0.016	0.266	0.922	0.045	-0.496	-0.658	0.717	0.015
MYO3_YEAST_Tsuboyama_2023_2BTT	3297	1.713	0.019	0.212	0.825	0.074	-0.374	-0.405	0.709	0.011
AMFR_HUMAN_Tsuboyama_2023_4G3O	2972	1.724	0.021	0.264	0.848	0.081	-0.665	-0.414	0.682	0.010
HECD1_HUMAN_Tsuboyama_2023_3DKM	5586	1.777	0.015	0.288	0.898	0.084	-0.427	-0.455	0.680	0.018
POLG_PESV_Tsuboyama_2023_2MXD	5130	1.806	0.011	0.352	0.905	0.044	-0.491	-0.488	0.775	0.016
DLG4_HUMAN_Faure_2021	6976	1.817	0.040	0.441	0.794	0.127	-0.637	-0.258	0.431	0.027
RASK_HUMAN_Weng_2022_binding-DARPin_K55	24873	1.876	0.023	0.646	0.903	0.061	-0.633	-0.299	0.460	0.054
RASK_HUMAN_Weng_2022_abundance	26012	1.882	0.027	0.487	0.774	0.107	-0.558	-0.123	0.441	0.028
A4_HUMAN_Seuma_2022	14811	1.946	0.032	0.365	0.785	0.106	-0.710	-0.206	0.562	0.005
YAP1_HUMAN_Araya_2012	10075	1.964	0.094	0.264	0.639	0.127	0.245	-0.242	0.598	0.017
PABP_YEAST_Melamed_2013	37708	1.969	0.038	0.446	0.856	0.106	-0.441	-0.145	0.631	0.059
GRB2_HUMAN_Faure_2021	63366	1.984	0.021	0.450	0.841	0.089	-0.354	-0.179	0.660	0.029
Q6WV12_9MAXI_Somermeyer_2022	31401	2.685	0.459	0.579	0.853	0.086	-0.727	-0.298	0.444	0.000
D7PM05_CLYGR_Somermeyer_2022	24515	3.038	0.547	0.437	0.705	0.058	-0.778	-0.476	0.350	0.002
Q8WTC7_9CNID_Somermeyer_2022	33510	3.055	0.499	0.540	0.818	0.098	-0.745	-0.241	0.458	0.000
F7YBW8_MESOW_Aakre_2015	9192	3.575	0.008	-0.214	0.925	0.241	0.376	-0.374	0.609	0.581
GFP_AEQVI_Sarkisyan_2016	51714	3.878	0.724	0.456	0.741	0.198	-0.879	-0.547	0.407	0.058
CAPSD_AAV2S_Sinai_2021	42328	4.728	0.439	0.269	0.862	0.189	-0.422	-0.223	0.539	0.005
F7YBW8_MESOW_Ding_2023	7922	5.426	0.783	-0.353	0.714	0.203	-0.204	-0.683	0.320	0.051

Table A4 – continued from previous page

Dataset	Size	Avg. Mutation	$\phi_{ m lo}$	$ ho_a$	NFC	I_d	ϵ _reci	FDC	$\phi_{ ext{EE}}$	η
GCN4_YEAST_Staller_2018	2638	17.068	0.966	-0.292	-0.083	0.295	-0.839	-0.146	0.304	0.031

Table A5: Selected landscape features for RNAGym tasks with mean mutation depth > 1.

Dataset	RNA Type	Size	φ _{lo} (%)	ρ_a (%)	NFC	I_d	$\epsilon_{ m reci}$	FDC	$\phi_{ ext{EE}}$	η
Andreasson2020	ribozyme	7343	0.078	0.080	0.404	2.748	0.043	-0.243	0.515	0.766
Beck2022	ribozyme	21321	0.022	0.498	0.917	0.335	0.123	0.081	0.522	0.092
Domingo2018	tRNA	4175	0.021	0.127	0.777	0.628	0.182	-0.506	0.681	0.076
Guy2014	tRNA	25491	0.393	0.106	0.484	2.434	0.191	-0.377	0.571	0.677
Janzen2022	ribozyme	1953	0.031	0.129	0.742	0.770	0.097	-0.285	0.627	0.004
Janzen2022	ribozyme	1953	0.048	0.182	0.823	0.666	0.065	-0.250	0.644	0.003
Janzen2022	ribozyme	1953	0.041	0.176	0.516	1.434	0.087	-0.017	0.617	0.001
Janzen2022	ribozyme	1953	0.032	0.177	0.529	1.107	0.075	-0.186	0.625	0.001
Janzen2022	ribozyme	1953	0.049	0.170	0.695	0.915	0.100	-0.226	0.609	0.002
Ke2017	mRNA	5533	0.078	0.292	0.906	0.394	0.150	-0.485	0.634	0.129
Kobori2015	ribozyme	255	0.008	-0.174	0.881	0.550	0.089	-0.317	0.800	0.135
Kobori2015	ribozyme	255	0.020	-0.194	0.805	0.582	0.117	-0.523	0.778	0.249
Kobori2015	ribozyme	1023	0.041	-0.239	0.407	0.895	0.339	-0.148	0.422	0.957
Kobori2016	ribozyme	10296	0.009	0.284	0.842	0.505	0.031	-0.003	0.519	0.053
Kobori2018	ribozyme	16383	0.016	-0.025	0.722	0.767	0.227	0.027	0.671	0.080
Li2016	tRNA	65536	0.356	0.051	0.357	0.707	0.095	-0.578	0.411	0.033
McRae2024	ribozyme	74942	0.758	0.195	0.754	0.512	0.055	-0.510	0.427	0.006
McRae2024	ribozyme	47503	0.439	0.363	0.750	0.304	0.107	-0.387	0.499	0.006
Peri2022	ribozyme	16383	0.001	0.113	0.955	0.472	0.066	-0.387	0.799	0.763
Roberts2023	ribozyme	33930	0.042	0.521	0.884	0.414	0.149	0.038	0.512	0.041
Roberts2023	ribozyme	21321	0.022	0.495	0.919	0.332	0.087	-0.242	0.521	0.077
Roberts2023	ribozyme	9045	0.035	0.391	0.852	0.455	0.122	-0.051	0.501	0.054
Roberts2023	ribozyme	22578	0.033	0.483	0.906	0.440	0.172	-0.172	0.520	0.065
Roberts2023	ribozyme	10296	0.016	0.344	0.876	0.436	0.079	-0.184	0.522	0.072
Soo2021	ribozyme	63430	0.021	0.039	0.752	0.725	0.238	-0.015	0.641	0.008
Tome2014	aptamer	417	0.317	0.011	0.421	0.060	0.500	0.294	0.402	0.005
Tome2014	aptamer	2652	0.049	0.392	0.831	0.236	0.078	-0.122	0.362	0.018
Zhang2020	ribozyme	111417	0.464	0.408	0.707	0.567	0.134	-0.441	0.546	0.009
Zhang2024	ribozyme	61393	0.492	0.461	0.656	0.612	0.239	-0.284	0.530	0.026
Zhang2024	ribozyme	69583	0.452	0.488	0.654	0.605	0.175	-0.219	0.538	0.012
Zhang2024	ribozyme	149710	0.450	0.222	0.387	0.885	0.143	-0.268	0.539	0.066